2017

Enhancement of Bandwidth and Laser Deflection Angle of Acousto-optic Deflectors by Dynamic Two-dimensional Refractive Index Modulation

Tiansi Wang
University of Central Florida

ENHANCEMENT OF BANDWIDTH AND LASER DEFLECTION ANGLE OF ACOUSTO-OPTIC DEFLECTORS BY DYNAMIC TWO-DIMENSIONAL REFRACTIVE INDEX MODULATION

by

TIANSI WANG
M.S. University of British Columbia, Canada (2006)
M.S. University of Central Florida, US (2012)

A dissertation submitted in partial fulfillment of the requirements
for the degree of Doctor of Philosophy
in the College of Optics and Photonics: CREOL & FPCE
at the University of Central Florida
Orlando, Florida

Spring Term
2017

Major Professors: Aravinda Kar

ABSTRACT

Acousto-Optic Deflectors (AODs) are inertialess optical solid state devices that have advantages over conventional mechanically controlled mirror-based deflectors in numerous scientific and industrial applications. These applications include fluorescence microscopy, sensing, variable-focus lens, photolithography and laser materials processing. AODs are currently operated with a single piezoelectric transducer that modulates the refractive index only in one direction. This operating principle limits the performance of AODs to a narrow acoustic bandwidth of the transducer and a small angle of laser deflection governed by the Bragg diffraction.

To overcome these two limitations, the operation of AODs with phased array ultrasonic transducers is analyzed in this study. Only the amplitude and frequency of the acoustic waves are modulated in conventional AODs. The phased array mechanism enables modulating the acoustic phase in addition to the amplitude and frequency modulations. The latter two phenomena affect the refractive index variation and its periodicity in the AOD medium, respectively, and the phase modulation produces tilted wavefronts due to diffraction and interference of the ultrasonic waves. Consequently, a tilted phase grating is formed inside the AOD device and the tilt angle automatically modifies the laser incident angle on the grating compared to the original angle of incidence on the AOD device. The acoustic frequency and amplitude are, therefore, modulated to achieve the Bragg diffraction under the new angle of incidence and maximize the diffraction efficiency, respectively.

The phase grating can be tilted at any arbitrary angle by steering the ultrasonic beam in different directions. The beam steering can be achieved by operating the transducers with various time delays to generate ultrasonic waves of different phases. Due to the diffraction pattern of the

ultrasonic intensity distribution, the refractive index varies both longitudinally and transversely to the beam steering direction, and two-dimensional refractive index modulation occurs when the transducers are very long in the third dimension. The acoustic waves affect the refractive index through the photoelastic effect by inducing mechanical strain waves in the AOD medium. The ultrasonic beam steering and the mechanical strain are determined using a modified Rayleigh-Sommerfeld diffraction integral. This integral represents the mechanical displacement vector field produced by ultrasonic waves in solid media. An analytic expression is obtained for the displacement field and the resulting strain distribution is calculated using this expression.

Based on the strain and the photoelastic constants, the two-dimensional variation in the refractive index is determined for single-crystal paratellurite TeO2 which is an excellent AOD material. Conventional two-dimensional coupled mode theory of AOD, which is based on only one-dimensional refractive index modulation, is extended in this study to analyze the effect of two-dimensional index variation on the performance of AODs. The diffraction efficiency and the laser beam deflection angle are determined for both plane waves and Gaussian laser beams by obtaining analytic solutions for the coupled mode equations. The diffraction efficiency is found to be nearly unity over a broad range of the acoustic frequency, and the deflection angle can also be increased by steering the ultrasonic beam at large angles.

This dissertation is dedicated to my parents, my friends, and my collegues extremely patient and supportive with me during all these years

ACKNOWLEDGMENTS

I joined the Laser-Advanced Manufacturing, Materials and Micro-Processing (LAMMMP) Laboratory at creol of UCF, supervisored by Dr. Aravinda Kar, on Octomber 30, 2012. Before that I have obtained Master of Science in optics and had studied in the field of fibers laser for nearly two years. I was planning to leave CREOL and began looking for a job but Dr. Shengyang Chen, who was close to graduate at that time, brought into my attention a piece of information. It was about there being a recent opening position for recruiting a new PhD student in LAMMMP group, in order to continue the so-called acousto-optic deflectors (AODs) project funded by Intel Corporation, for next generation laser microvia drilling or UV lithography in the applicaiaton for high density internects (HDIs) fabrication and processing. Encouraged by such unexpected news, I right away prepared my CV and credits records of all classes ever attented at CREOL for Dr. Kar's examination and Intel Corporation's review. Finally and luckily, based on the previous weekly reports and additional literature reviews, I passed my Candidacy Exam on Oct. 30, 2012 and then jumped the first step along my academic journey to PhD degree. That is why and how I decided to stay and pursue a PhD degree at CREOL. There is no doubt, Dr. Shengyang Chen is the first person I would like to say "Thank you!".

It has been passed four years since the lauching of the AOD project so far. As a routine agenda, there was about 100 or so weekly presentation which had to be given every Friday during one hour teleconference meeting, except the holidays and my absence due to illness. Dr. Chong, one of previous graduates, represented Intel for weekly presentation examiner and the project communicator between Intel Corp. and CREOL; while on the side of CEROL, Dr. Kar supervisored this project as a principla investigator (PI) and gave very specific guidance to make

sure my weekly research activies at the right track to meet the Intel's expectation and requirements. I appreciated weekly discussions and suggestions with Dr. Chong to help me improve the studies and investigations and gradually learned how to satisfy the project's traget in terms of Intel's thinking-ways and befefits. I am also about to thank Dr. Kar for introducing me into such exciting and impressive research field on the interaction between acoustic waves and laser beams, no one ever took initative try before in LAMMMP group. I have to admit that the core concept of the AOD project proposed in this dissertation just came out of Dr. Kar's genius construction and partial analytical formulations can not be derived without Dr. Kar's handwriting demonstration and lectureing on whiteboard. It is no exaggeration that Dr. Kar opened a door and show me how to apply all the knowledge I have learned wherever in China, Canada or US to the real world. In summary, it is what we commonly referred to as "putting into practice what one has learnt".

I would also like to extend my thanks to the members of the committee, Dr. Patrick L. LiKamWa，Dr. M. G. "Jim" Moharam and Dr. Raj Vaidyanathana. I am grateful for Dr. Raj Vaidyanathana's wise advice and help, particularly in my final exam defense. In spite of the busy schedule Dr. M. G. "Jim" Moharam had always time for me whenever consulting theoretical explanation during his office. Discussion with him was very enriching which helped me in strengthening my concepts and skills on the laser beam diffraction process due to index modulaiton in phase graing.

Last, but not least, I would like to thank my parents for their love and financial support in difficult and disturbing situations, especially in my last two semester (Summer term and Fall term in 2016). Without their generous funding, I cannot make payment to tuition fees and medical insuranes and cannot complet registeration for my student status.

TABLE OF CONTENTS

LIST OF FIGURES

LIST OF TABLES

LIST OF ACRONYMS/ABBREVIATIONS

AODs	Acousto-Optic Deflectors
AOMs	Acousto-Optic Modulators
Bragg cell	A device using a bulk acousto-optic interaction
0^{th}-order,	The beam directly transmitted through the cell
-1^{st}-orfer	The beam generated when the laser beam interacts with laser
Bragg angle	The partilular angle of incidence gives diffraction into a single order
Separation angle	The angle between the 0^{th}-order and -1^{st}-order
RF bandwidth	The particular frequency rangle matching Bragg condition
Defleciton angle	The angle range of -1^{st}-order scanning across RF bandwidth
Diffraction efficiency	The fraction of 0^{th}-orderm being diffracted into -1^{st}-order
Resolution	The number of resolvable spots across deflection angle scanning
$K = \frac{2\pi}{\Lambda}$	Acoustic wave number in AO medium
$k_0 = \frac{2\pi}{\lambda_0}$	Optical wave number in vaccumm
$Q = \frac{2\pi(\lambda_0/n_0)L}{\Lambda^2}$	Klein and Cook parameter
$v = k_0 \Delta n L$	Raman-Nath parameter
$\Delta n = -0.5{n_0}^3 p S_0$	Sound-induced peak refractive index change
n_0	Refractive index of AO medium
p	Appropriate elasto-optic coefficient
$S_0 = \sqrt{\frac{2I_S}{\rho_0 V^3}}$	Amplitude of condensation $\Delta\rho/\rho$ or strain

I_s	Sound intensity
ρ_0	Density of medium
V	Sound velocity
$M_2 = \frac{{n_0}^6 p^2}{\rho_0 V^3}$	Figure of merit
P	Acoustic power radiated by transducer
$sin\theta_B = \frac{\lambda_0}{2\Lambda}$	Bragg condition in vaccumm, θ_B is the Bragg angle

CHAPTER 1: INTRODUCTION TO LASER BEAM SCANNING AND GENERAL APPLICATIONS

Since the invention of the laser in 1960, the demand for various methods to scan, deflect, switch or modulate laser beam scanning has been developed for a wide range of scientific and industrial applications, such as fluorescence microscopy, optical storage, laser printers, display, sensing and laser material processing [1,2]. Among these applications, these laser beam scanners are used to scan or deflect the laser beam, in order to position the laser spot, in 1D, 2D, or even 3D dimensions, on the surface of the substrate under consideration. To achieve fast response time, large deflection scan angle, large band width and high diffraction efficiency is of interest not only for microscopy applications, such as random-access scanning fluorescence microscopy [3] and swept-source optical coherence tomography [4], but also for high-power, high-repetition-rate laser material processing [5,6,7].

1.1. What is it meant by laser beam scanning?

In modern optical engineering, the term laser beam scanning is used to mainly describe the controlled deflection of laser beams, visible or invisible [8]. The scanned laser beams can be used in stereo-lithography, in laser material processing, in laser engraving machines, in confocal microscopy, in laser printers, in laser shows, in Laser TV, in LIDAR and in barcode scanners. Laser beam scanning or deflection devices are capable of: pointing a laser beam randomly within a wide field-of-view; stepping the beam in small increments from one angular position to the next; dwelling in each position for the required time on target.

In contrast, laser beam scanning devices move the beam axis continuously and laser beam switching devices are only able to address predefined directions [9].

1.2. Types of light beam deflectors

Various laser beam deflectors may be loosely grouped into two categories: lowe-speed and high-speed deflectors, see Fig. 1-1. The low-speed mechanical deflectors, such as Galvanometric scanners, Piezo scanners and static MEMS scanners, are fundamentally limited by the inertia associated with the mass of the rotating mirror and other moving parts ($\dot{\theta} < 10^3$ rad/s) and hence difficult to exploit the high repetition-rate ($f_{rep} = 100MHz$) of ultrashort pulsed laser sources; while other high-speed mechanical deflectors, including rotating polygon wheel scanners, resonant Piezo scanners and resonant MEMS scanners, can achieve high-speed deflection angle velocity $\dot{\theta}$ and large maximum deflection scan angles $\Delta\theta$ by operating the mechanism at its eigen-frequency.

In essence, polygon and resonant scanners are operating in raster scanning mode, in which the laser beam scans over the substrate line by line in a raster pattern. In this approach, the laser power is to be modulated and synchronized to the laser pulse frequency f_{rep}, in order to deliver the desired energy dose at the desired location on the substrate.

In contrast to raster scanning, random-access scanning scans the laser beam along a trajectory where the laser energy actually needs to be delivered to the substrate, rather than scanning the entire area. Random-access scanning can provide a higher spatial resolution, as well as a reduced processing time, when compared to raster scanning.

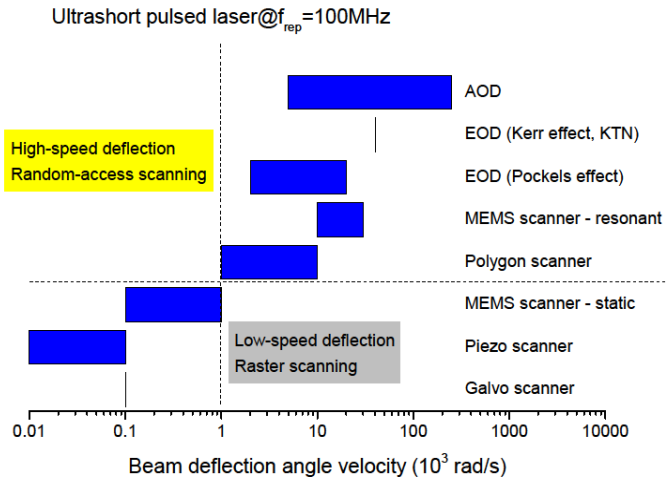

Figure 1-1 Laser beam scanning technologies of high-speed deflection vs. low-speed deflection.

1.2.1. Galvanometers (mirror-based deflectors)

All modern high-performance oscillating galvanometer scanners are built with a moving magnet torque motor, position transducers, bearing suspension, and mirrors, see Fig. 1-2.

- The torque motor is selected for its ability to integrate with the other elements of the scanner, the mirror, the position transducer, and the electronic driver/controller
- The torque motor is built with large air gaps, where the drive coil is housed, and consequently radial forces are negligible.
- The torque motor pushes against the torsion bar and positions the mirror.
- Galvanometric scanners are built with either ball bearing suspension or flexure bearing suspension.

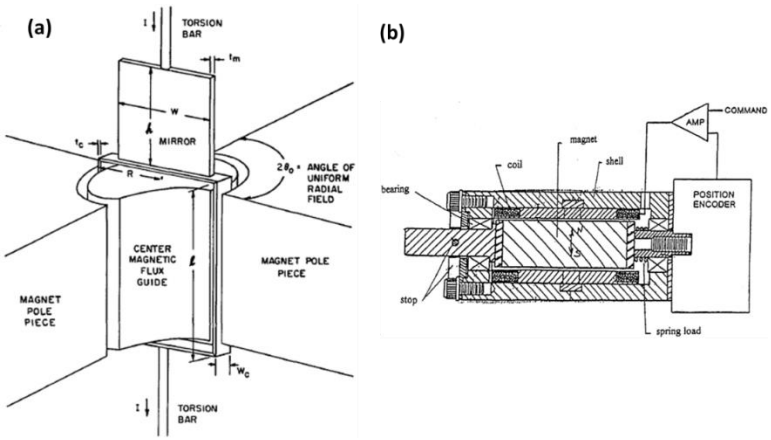

Figure 1-2 (a) Schematic view of oscillating galvanometer and (b) illustration of all inside construction elements [8].

1.2.2. Electro-optic deflectors (EODs)

An Electro-Optic Deflector (EOD), see Fig. 1-3, means the change of the refractive index, Δn, of a material as a result of an electric field E applied to an optically transparent crystsl. The latter is achieved by applying an electric voltage over the EO medium. The change of the refractive index, Δn, is caused by electro-magnetic forces that perturb the position, orientation or shape of atom or molecule structure in the EO material. EODs refract a laser beam by introducing a phase delay across the cross section of the laser beam.

Two types of EO effects are distinguished: if the refractive index varies linearly with the electric field, it is referred to as *the Pockels effect* (LEO effect); if quadratically with the electric field, it is referred to as *the Kerr effect* or quadratic electro-optic effect (QEO effect).

These index-changes are small and usually of the order of $\Delta n \approx 10^{-4}$. Usually the Pockels effect is stronger than the Kerr effect, but for special EO crystal KTN, which shows larger index change ($\Delta n \approx 10^{-2}$) and in turn the larger deflection angle $\Delta\theta$.

The scan angle of deflection is defined as (for Pockels effect), see in Fig. 1-3(a)

$$\Delta\theta_p = \frac{\Delta n}{n}\frac{l}{w} \tag{1}$$

where n denotes the refractive index of the optical prism, Δn denotes the difference between the refractive index of the optical prism and the surrounding material.

The scan angle of deflection is defined as (for Kerr effect, taking the example of KTN), see Fig. 1-3(b)

$$\Delta\theta_e = -0.153 n^3 {\varepsilon_0}^2 {\varepsilon_r}^2 \frac{V^2}{d^3} L \tag{2}$$

where ε_0 and ε_r are the permittivity of vacuum and relative permittivity, n is the refractive index of the EO crystal at $V = 0$, L denotes the propagation length of the laser beam in the EO crystal and d denotes the thickness of the EO crystal.

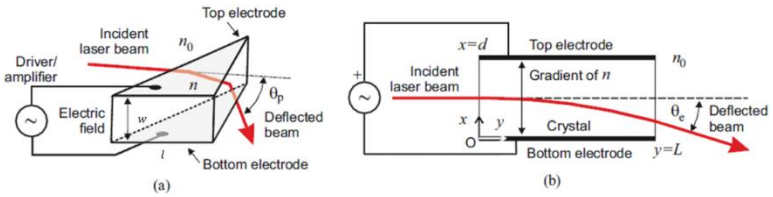

Figure 1-3 Two typical configurations of an EOD: (a) EOD based on the Pockels effect and (b) EOD based on the Kerr effect [2].

1.2.3. Acousto-optic deflectors (AODs)

The acousto-optic deflectors are based on the acousto-optic interaction between travelling acoustic waves (bulk or surface type) with perpendicularly propagating laser beams (free or guided) due to the photoelastic effect. The acoustic waves produce a periodic refractive index modulation, Δn,

from which the optical waves are diffracted or scattered. Several physical mechanisms can contribute to the formation of the periodic refractive index modulation [1,2]:

- the bulky acoustic strain modulates the refractive index of the AO medium through the acousto-optic (AO) effect;
- the surface acoustic strain generates the index changes in an optical waveguide by periodically changing its thickness;
- in piezoelectric mediem the traveling acoustic wave may be accompanied by periodic electric fields which induce a refractive index change through the electro-optic (EO) effect.

These effects create a moving phase grating from which the light wave diffract. Two diffraction modes, $\pm 1^{st}$-order mode ($\vec{E}_{\pm 1}$) and 0^{th}-order mode ($\vec{E}_0$) are most important for the practical applications under the incident angle satisfying the Bragg diffraction ($\theta_{in} = \theta_B$), see Fig. 1-4(a). Most of the acousto-optic beam deflectors are based on the 1^{st}-order mode, which is characterized by diffraction of the incident optical wave into almost entirely one order. This case is realized for a sufficiently long interaction length L, so that the thick phase grating may be considered. The general nature of the laser diffraction process can be described by one parameter introduced below:

The Raman-Nath parameter in the medium is given by the Klein-Cook parameter as below

$$Q = \frac{2\pi(\lambda_0/n)L}{\Lambda^2} \tag{3}$$

where λ_0 is the optical wavelength in the vacuum, n is the refracted index withoug strain field and Λ the acoustic wavelength in the medium [10].

- when $Q \ll 1$, Raman-Nath region: laser diffracts into multiple diffraction orders;
- when $Q \gg 1$, Bragg region: laser appears in only one or two diffraction order;

- when $Q \approx 1$, Transition region: in the middle between pure phase modulatioin and Bragg deflection, no simple analytic solutions exist for solving problems of this type and only numerical methods will be resoted to.

Three important parameters are often used to evaluate the AO devices performance , kind of as a performance criterion, bandwidth (ΔB), diffraction efficiency (η), and the deflection scan angle ($\Delta\theta$). In Fig. 1-4(a), in which case the acoustic grating appears to be a thin phase grating and a multiplicity of diffracted orders results.

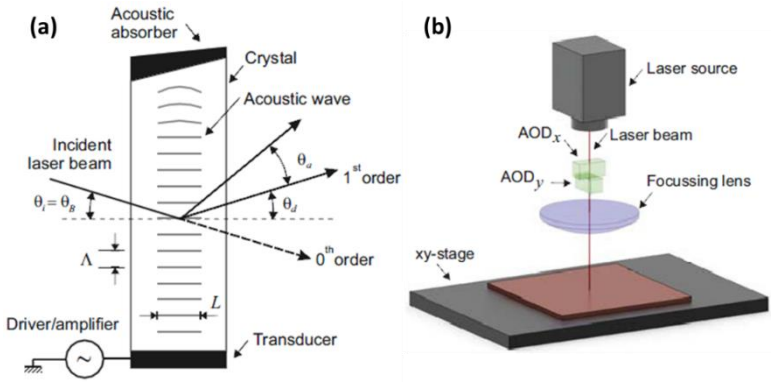

Figure 1-4 Typical configuration of an AOD (a) and a two-dimensional light deflectors by arranging two OADs orthogonally in series [2].

The Bragg angle in the air outside of the crystal, see Fig. 1-4(a), is defined as

$$\theta_B = sin^{-1}\left(\frac{\lambda_0}{2\Lambda}\right) \tag{4}$$

The maximum deflection angle or the maximum deflection scan angle in the air outside of the crystal, see Fig. 1-4(a), is defined as

$$\Delta\theta = \frac{\lambda_0}{V}\Delta f \tag{5}$$

1.3. Performance criterion of mechanical deflectors vs. optical deflectors

Resolution (N_R), bandwidth (ΔB), and speed or access time (τ_0) are the important characteristics shared by all types of light beam scanning or deflection system. The resolution is defined as the maximum deflection angle divided by the diffraction limited angle:

$$N_R = \Phi_m W / e\lambda_0 \tag{6}$$

where W is the aperture of the mirror, λ_0 is the wavelength of light in vacuum, and e is a number of order unity that depends on the uniformity of illumination of the input optical window and the criterion used for resolution. The random access time is defined as

$$\tau_0 = \frac{1}{2f_0} \text{ (for galvanometer)} \tag{7}$$

where f_0 is the specified resonant frequency of the galvanometer. Advantages for a mechanical beam deflector as follows:

A mechanical deflector has only a single surface (one mirror for one dimension); while in the non-mechanical deflectors, the light interacts with a volume of active material that must be of high optical quality as well as having good optical surfaces and low acoustic or dielectric losses.

A mirror deflector is simple to align and use because of its large angular aperture compared to Limitations of a mechanical deflector as follows:

- First limitation is their low speed. The scanning frequency typically not exceeding 200/s, which is generally insufficient for many current industrial applications.
- Second limitation consists in the complexity of the mechanically driven systems. Their performance is strongly affected by environmental factors such as vibrations and depends on the physical robustness of their components at industrial conditions.

- Third limitation, they don't allow random access, have short operational life time, and are susceptible to mechanical damage.

Comparing with mechanical deflectors, the acousto-optic deflectors and electro-optic deflectors have high angular accuracy (μrad) and small access time, τ (μs) but less resolution, N, that is. the number of the resolvable spots, see Fig. 1-5 and Fig. 1-6 below.

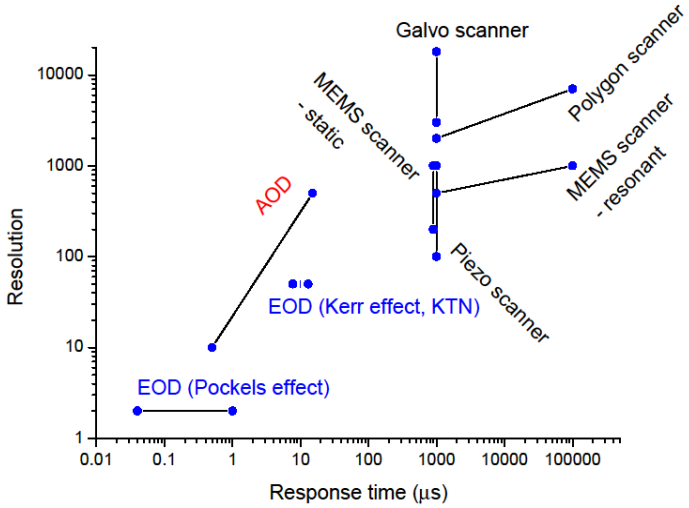

Figure 1-5 Resolution vs. response time of various light beam scanning technologies at infra-red wavelength (1.0 μm) [2].

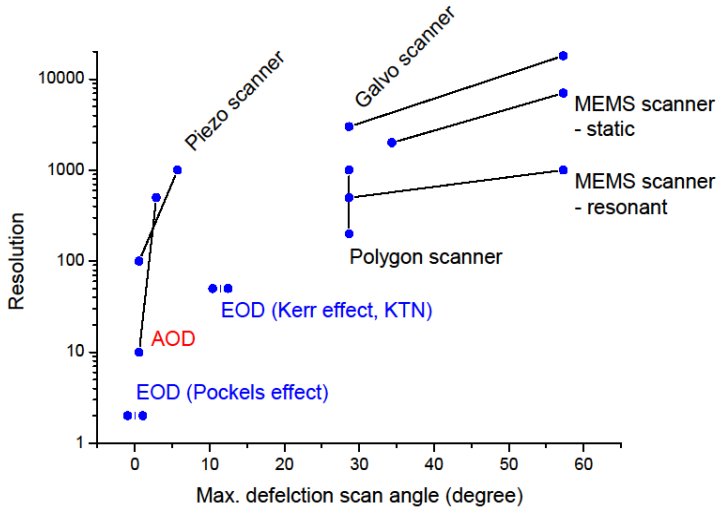

Figure 1-6 Resolution vs. maximum deflection scan angle of various light beam scanning technologies at infra-red wavelength (1.0 μm) [2].

1.4. Potential applications of Acousto-optic deflectors for laser direct machining

The term laser direct machining is used here to describe materials processing with the focused spot of a laser beam (Fig. 1-7).This technique is used in a wide range of micromachining applications where high precision and small feature sizes are essential, including laser microvia drilling, fuel injector drilling, gas sensor drilling, solar cell scribing and MEMS prototyping. The movement of the beam relative to the workpiece using a glavo-scanner and motorised stages is synchronized with the firing of the laser to create the desired features. Processing speeds of up to 10 ms can be attained with a Galvanometric scanner [2,11].

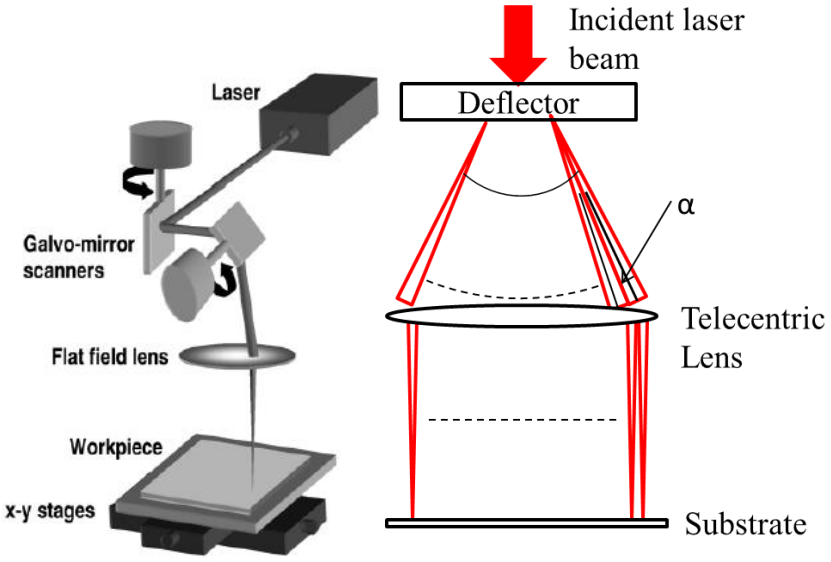

Figure 1-7 Schematic of the direct machining using a galavo-scanner and motorised x–y translation stages (left) and using a acousto-optic deflector and a Telecentric lens (right).

1.4.1. AODs potential application in the CW laser material processing

In Fig. 1-8, the examples of demonstration of what the CW laser material processing can be done with high power continuous wave (CW) laser sources [12]: (a) metal cutting of 5-mm-thick stainless steel with a CO_2 slab laser of 2kW; (b) a laser trepanned hole as used in diesel fuel injectors (the typical diameter is 40–150 μ m through 1-mm steel); (c) a spinneret hole showing the versatility of trepanned laser holes, which can be of almost any required shape; (d) micrograph of the transverse section through a laser-welding showing the fusion and heat affected zones.

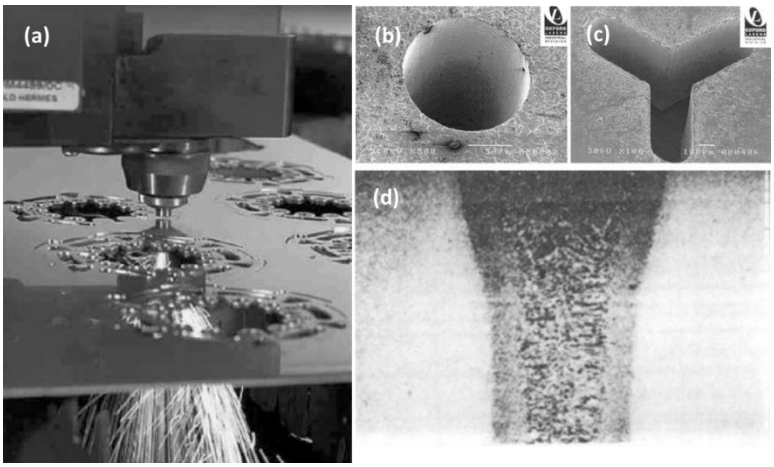

Figure 1-8 Examples of showing high power CW-laser used in the material processing: (a) laser-cutting, (b) laser-drilling; (c) laser-piercing and (d) laser-welding [12].

1.4.2. AODs potential application in the CW laser microvia drilling

In the electronics industry, a "via" is a hole through a material which, when filled with a conductive material such as copper or silver-conductive ink, creates an electrical connection between at least two conductive layers. The typical configuration has sandwich-type, involving two conductive layers separated by an insulating substrate. Vias can be divided into two types:

- Through vias are drilled through all layers of the laminate structure.
- Blind vias are initiated at one surface and stop at a layer interface within the laminate.

Vias are routinely drilled by pure mechanical methods with diameters 500 μm down to 100 μm. However, as the diameter decreases, the vias become more difficult and costly to produce using traditional mechanical methods. An advantage offered by laser microvia drilling is that high power CW lasers can readily drill small diameter vias from 200 μm down to 25 μm [7,13].

Figure 1-9(a) shows the microvia produced with a pitchfork beam of pulse energy = 0.3 mJ. Top diameter = 55 μm, bottom diameter = 48 μm and tapering angle = 5°. Fig. 1-9(b) shows the drilling front profile produced with a pitchfork laser beam (pulse energy = 0.3 mJ, averaged beam radius = 21 μm, pulse width = 430 ns, repetition rate = 83.3 kHz).

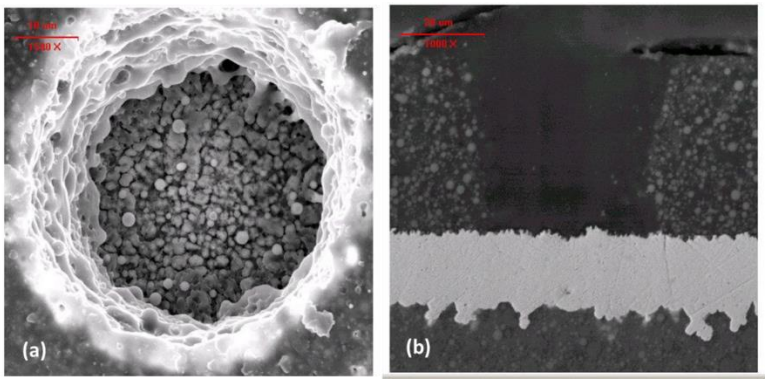

Figure 1-9 Examples of laser microvia drilling (Courtesy of Dr. Chong Zhang at CREOL).

1.5. References

[1] M. Gottlieb, et al., Electro-optic and acousto-optic scanning and deflection (Marcel Dekker, Inc. 1983).

[2] G. Römer and P. Bechtold, "Electro-optic and acousto-optic laser beam scanners," Physics procedia **56**, 29-39 (2014).

[3] A. Bullen and P. Saggau, "High-Speed, Random-Access Fluorescence Microscopy: II. Fast Quantitative Measurements With Voltage-Sensitive Dyes," Biophysical Journal **76**(4), 2272-2287 (1999).

[4] Y. Okabe, et al., "200 kHz swept light source equipped with KTN deflector for optical coherence tomography," Electronics Letters **48**(4), 201-202 (2012).

[5] S. Bruening, et al., "Ultrafast scan techniques for 3D-µm structuring of metal surfaces with high repetitive ps-laser pulses," Physics procedia **12**, 105-115 (2011).

[6] J. Schille, et al., "Micro structuring with highly repetitive ultra short laser pulses," Proceedings of LPM2008-the 9th International Symposium on Laser Precision Microfabrication (2008).

[7] C. Zhang, *Thermal Modeling and Laser Beam Shaping for Microvias Drilling in High Density Packaging*, PhD thesis, University of Central Florida Orlando, Florida (2008).

[8] G. F. Marshall and G. E. Stutz, *Handbook of optical and laser scanning* (CRC Press 2011).

[9] H. D. Tholl, "Novel laser beam steering techniques," Proc. of SPIE **6397**, 639708-1:14 (2006).

[10] W. R. Klein and B. D. Cook, "Unified Approach to Ultrasonic Light Diffraction," Sonics and Ultrasonics, IEEE Transactions on **14**(3): 123-134 (1967).

[11] B. K. A. Ngoi, et al., "Angular dispersion compensation for acousto-optic devices used for ultrashort-pulsed laser micromachining," Opt. Express **9**(4), 200-206 (2001).

[12] K. G. Watkins, et al., *Laser Material Processing* (Springer 2010).

[13] Wikipedia, "Microvia," https://en.wikipedia.org/w/index.php?title=Microvia&printable=yes.

CHAPTER 2: TECHNICAL BARRIER IN CURRENT AOD TECHNOLOGY AND TECHNICAL APPROACH

2.1. Performance criteria for future HDI requirements in semiconductor industry

With the advent of smartphones and hand-held electronic devices, microvias have evolved from single-level to stacked microvias that cross over multiple high density interconnect (HDI) layers (e.g. finer lines and spaces, and smaller vias). The reliability of HDI structure is one of the major challenges for its successful widespread implementation in the current semiconductor industry. The reliability of microvas depends on many factors such as microvia geometry parameters, dielectric material properties, and processing parameters. Among them, good geometrical reliability of microvias is an essential part of HDI reliability [1,2,3,4,5].

HDI standards in semocondutor indutry define microvias as blind or buried vias with a diameter equal to or less than 150 μm. Microvia geometry parameters, such as microvia diameter, wall angle and plating thickness, must be carefully optimized to fabricate reliable microvias, especially for stacked microvias, without resulting in incomplete filling, dimples, or voids in the copper plating process, as seen in Fig. 2-1 [6].

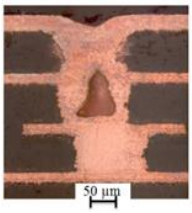

Figure 2-1 A cross-section view of a microvia with a void.

Since the traditional mirror-based mechanical deflectors, i.e. galvanometers, can not meet the future confronting requirements of HDIs fabrication and processing in the semiconductor industry, the nonmechanical optical deflectors for laser microvia drilling, as a potential alternative candidate, come into attention with the required performance criteria highlighted in Table 1.

Table 1 Performance criteria of optical deflectors for future semiconductor industrial requirements

Process parameters		**Performance criteria**
Scanning resolution (δr)		0.25 - 1 μm
Position accuracy (δr_{PA})		1 - 3 μm
Scanning field (2r > 30mm)		$> 30 \times 30\ mm^2$
Deflection angle range ($\pm \frac{\Delta\theta}{2}$)		$\pm 3^o - \pm 10^o$
Stepping speed ($\frac{1}{\tau}$)	CO_2	20 - 100 kHz
	UV	20 kHz - 2 MHz
Target feature ($D_{microvia}$)	CO_2	40 μm
	UV	8 μm
Power handling	CO_2	50 W ($3\ W / cm^2$)
	UV	5.0 W ($1.5\ W / cm^2$)
Diffraction efficiency (η)		> 50%

2.2. Technical barriers facing the current AOD devices

As we mentioned before, the three main parameters of any current acousto-optic deflectors (AODs) are diffraction efficiency η, transit time τ and bandwidth ΔB. The resolution is defined as the number of resolvable spots and equals the product of the transit time and bandwidth; while the diffraction efficiency is the fraction of the -1st-order diffracted power ot the laser inputr power and the bandwidth corresponds the maximum deflection scan angle. Future HDIs fabricagtion and processing requires a high performance of optical deflection both in high diffraction efficiency and large deflection scan angle for fast scanning laser beam over a large angular range.

The current acousto-optic deflectors is limited by the bandwidth, as imposed by the Bragg condition, as seen in Fig. 2-2. The traditional method of enlarging the interaction bandwidth is normally to increase the acoustic beam diffraction spread by shrinking transducer plate. Unfortunaltely, that is not ideal approach to solve the limitation. There are two disadvantages going with this approach:

- first, only partial of the acoustic momentum components can satisfy phase matching to the incident or the diffracted light momentum components and the rest of acoustic momentum or power are wasteful.
- second, this increased acoustic power density due to the transducer size shrinking may produce heating at the transducer, and in turn lead to thermal distortion in the acousto-optic medium due to the gradients in the acoustic velocity and refractive index.

As Bragg condition in the case of isotropic acousto-optic interaction is pictured in Fig. 2-2, the momentum vectors do not form a closed triangle, which means certain amount of momentum is

lost. Phase mismatch of $\Delta k_i = 2\pi\Delta\left(\frac{1}{\lambda_i}\right)$ leads to momentum loss of $\left|\Delta\vec{p}\right| = \hbar\Delta k_i$, and then finally the energy loss is $\hbar c\Delta k_i$. The energy loss brought up by the tuning of acoustic frequency has bad effect on laser vias-drilling: the energy in central lobe decreases and the energy in side lobes start to increase which affects the quality of vias-drilling; the dissipated energy will heat workpiece [7].

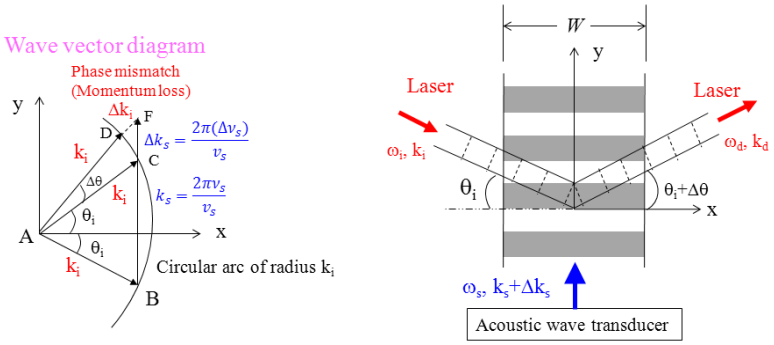

Figure 2-2 Bragg condtion for effective acousto-optic interation in Bragg diffraction region.

2.3. An ideal solution to this issue

An ideal solution to this t=difficulty would be the approach in which the acoustic beam changes in direction as the RF frequency is varied, so that for every RF frequency the Bragg condition is perfectly matched. This promising approach was fistly proposed by LMAAA group at CREOL, UCF, as far as we kmow. The so-called “actoustic beam steering” can be achieved by utilizing multiple phase array transducer based on PZT plate and electronically tuned by RF signal to control the applied frequency components and RF power and time delay between neighboring elements of tranducer array. By using multi transducer array attached to the acousto-optic medium, the atomic planes in the AO medium can be tilted to satisfy strictly Bragg Reflection Condition all the time

whatever the tuning of acoustic frequency is. Fig. 2-3 illustrates such idea with two typical cases of atomic planes tilting: (left figure) by appropriating combination of RF frequencies and RF power, the atomic plane inside AO medium is tilted on purpose to deflect the input laser beam to the right-up corner; (right figure) similarly, by utilizing another suitable combination of RF signal both in frequencies and power distribution among individual elements, the input laser beam can be deflected to the right-down corner.

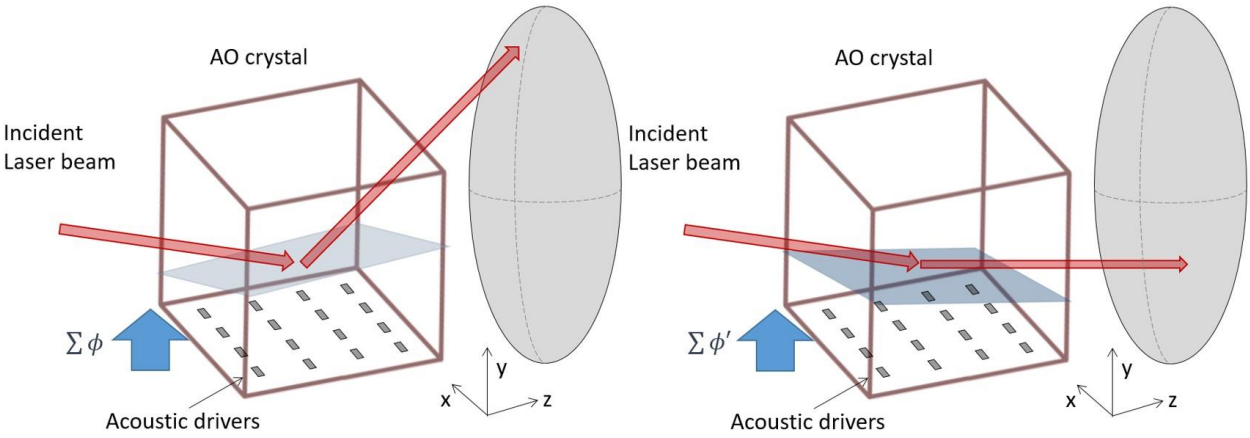

Figure 2-3 Deflection of laser beam to the top of focusing lens (left); to the bottom of the focusing lens (right).

2.4. References

[1] IPC/JPCA-2315, “Design Guide for High Density Interconnects (HDI) and Microvias,” June 2000.

[2] IPC-2226, “Sectional Design Standard for High Density Interconnect (HDI) Printed Boards,” April 2003.

[3] H. Holden, *The HDI Handbook (1st Edition)*, available from: http://www.hdihandbook.com/.

[4] B. Birch, “Reliability testing for microvias in printed wire boards,” Circuit World **35**(4), 3 – 17 (2009).

[5] IPC-6016, “Qualification and Performance Specification for High-density Interconnect (HDI) Structures,” May 1999.

[6] Wikipedia, "Microvia," https://en.wikipedia.org/w/index.php?title=Microvia&printable=yes.

[7] A. Yariv and P. Yeh, *Optical waves in crystals* (Wiley, New York, 1984).

CHAPTER 3: TWO-DIMENSIONAL ANALYTIC MODELING OF ACOUSTIC DIFFRACTION FOR ULTRASONIC BEAM STEERING BY PHASED ARRAY TRANSDUCCERS

3.1. Introduction

Ultrasonic phased arrays consist of a number of individual elements of width comparable to or smaller than the ultrasonic half-wavelength and spacing of 56 μm between two consecutive elements. This type of geometry offers a dynamic means of focusing and scanning the ultrasonic beam by modulating the time delay between the RF electronic excitation of the individual element. The phased array technology dominates in several important areas, such as radar, underwater acoustics, medical diagnostics, and therapeutic treatment. Much of the early work implemented one-dimensional arrays in medical devices for imaging applications [1-3]. Later two-dimensional arrays were implemented for volumetric imaging [4-6]. This initial success of the technology quickly spread into numerous sub-disciplines, such as pulse-echo imaging, Doppler techniques, sono-elastic imaging, computed tomography, and three-dimensional imaging [7-8]. Improvements were made in the therapeutic field by introducing intracavity phased arrays capable of increasing tissue temperature as a potential tool for prostate cancer treatment [9-11] and transskull therapy [12].

Non-destructive testing or evaluation (NDT or NDE) of materials, mainly in the field of nuclear inspection, utilizes the phased array transducer technology [13]. This technology enables acoustic imaging for NDE and locating the position of flaws quickly and accurately. Other notable endeavors include the time-reversal processing [14], and self-focusing techniques [15]. These efforts have provided a variety of NDE tools for industrial applications to image flaws or detect defects by swiftly scanning an ultrasonic beam over the material of interest [16]. The sensitivity

and efficiency of the ultrasonic diagnostic and inspection are greatly enhanced by the phased array technique due to the constructive or destructive interference as well as the diffraction of the ultrasonic waves.

The tremendous success of the ultrasonic diagnostic technology in the medical and NDE fields sparked considerable interest for possible applications in optics and photonics since 1960s [17] after the invention of lasers. Acousto-optic scanning and deflection (AOSD) devices have been produced for a variety of laser applications such as detection, modulation, or filtering of coherent light. The operating principle of these devices include modulation of the refractive index of an acousto-optic medium using acoustic waves to generate a transparent dynamic volume phase grating that deflects an incident laser beam. This type of acousto-optic deflectors (AODs) has been used in many applications such as laser marking, micromachining, patterning and direct writing. Galvo scanners are traditionally used to direct laser beams to different locations on a workpiece using two mirrors. The mechanical motion of x-y mirrors in the scanner affects the accuracy of beam positioning and repeatability in high-volume manufacturing. Ultrasonic beam steering without any moving optical component is necessary to overcome the limitations of conventional scanning technology. The ability to steer ultrasonic beam in different directions within the acousto-optic crystal using phased array transducers provides a unique device for flexible and high speed deflection of laser beams with high precision and accuracy.

The fundamental aspect of this new device is the capability to steer ultrasonic waves inside the crystal using phased array transducers. The diffraction of the waves is studied to analyze the formation of the zeroth order diffraction lobe as the steered ultrasonic beam. The ultrasonic displacement vector field generated by an immersion piston transducer can be calculated using the Rayleigh-Sommerfeld integral (RSI) model for liquid [18]. In solid media, on the other hand,

Vezzetti's model [19] is applied to determine the ultrasonic displacement vector field generated by a contact piston transducer, because this model accounts for the Christoffel equation of motion. This solid media model yields an integral equation for the displacement vector field by the method of angular spectrum. Schmerr [20] simplified Vezeetti's model to obtain an explicit expression that resembles the Rayleigh-Sommerfeld diffraction integral for the displacement field and, therefore, Schmerr's model is called the modified Rayleigh-Sommerfeld integral (mRSI) model.

Since TeO_2 is a good AOD material for lasers of wavelength 0.35 - 5.0 μm, an analytic expression is derived in this paper for the displacement field in TeO_2 by applying the mRSI model to an ultrasonic linear phased array transducers. This paper begins by presenting a theoretical background in Section 2 as a foundation for the two models, Fourier and Filon models, developed in this study. These two new models are validated in Section 3 by comparing their results to that of the non-paraxial multi-Gaussian beam (NMGB) model [21] and then the profile of the displacement field is analysed using the Fourier model for various ultrasonic beam steering angles. Finally, the results are summarized and discussed in Section 4.

3.2. Theoretical Background

Conventional AODs are operated with a single transducer, or an array of transducers assembled in the planar or stepped configuration [22]. The performance of single-transducer AODs is limited by the applied radiofrequency (RF) power, narrow bandwidth, small deflection angle and narrow scan angle of the laser beam, and low diffraction efficiency. Phased array transducers are used to improve the performance of AODs. Each transducer is operated with relative time delay in the applied RF power to generate phase-shifted ultrasonic waves. These waves form a tilted wavefront

in the AOD medium due to the diffraction of the waves. The interaction of a laser beam with the tilted wavefront improves the deflection angle and diffraction efficiency [23]. Conventional phased array AODs are, however, operated with fixed time delays, and therefore, the ultrasonic wavefronts cannot be steered at any arbitrary angle for a given AOD. To achieve flexibility in the ultrasonic beam steering, the time delays of the transducers can be varied during the operation of the AOD. This type of beam steering or focusing technique produces a tilted ultrasonic diffraction pattern with the zeroth order diffraction lobe pointing in the principal direction z_s at the steering angle θ_s as shown in Fig. 1a [23, 24] .

In this paper, the mathematical formulation to analyze the beam steering is based on Nakahata and Kono's [25] three-dimensional model for ultrasonic wave patterns in solids due to phased array transducers. Their single-transducer model is applied to multiple phased array transducers in this study for two-dimensional wave patterns. The geometry of the AOD medium is presented in Fig. 1a with transducers that are infinitely long along the y axis. So the displacement of the atoms at any point P(x,z) in the AOD medium for unit length in the y direction is given by the following expression for longitudinal ultrasonic waves in the medium.

$$\vec{\mathrm{U}}(x,z) = \frac{1}{2\pi\rho}\sum_{m=1}^{M}\frac{P_m}{c_{lm}^2}\int_{-\infty}^{\infty} D(\theta(x_m))\vec{d}_p(x_m)\frac{\exp[(i\kappa_m-\alpha_m)r_m]}{r_m} Rect\left(\frac{x_m-x_{cm}}{2a_m}\right) exp(i\Delta\phi_m)dx_m \qquad (1)$$

Here ρ is the density of the AOD medium and c_{lm} represents the speed in this medium for the longitudinal ultrasonic waves emitted by the m-th transducer. Since the speed depends on the ultrasonic frequency, the effect of operating the transducers at different frequencies can be analyzed by selecting the value of c_{lm} corresponding to each frequency. p_m is the pressure exerted on the AOD medium by the m-th transducer. κ_m (=ω_m/c_{lm}) and α_m are the wave number and attenuation coefficient of the ultrasonic wave in the medium, respectively, where ω_m is the angular

frequency of the waves, due to m-th transducer. M is the total number of transducers. The distance between the point P(x,z) and an arbitrary point B(x_m,0) on the m-th transducer is denoted by

$$r_m = BP = \sqrt{(x - x_m)^2 + z^2} \tag{2}$$

and the rectangular function is defined as

$$Rect\left(\frac{x_m - x_{cm}}{2a_m}\right) = \begin{cases} 1, \text{for } x_{cm} - a_m \le x_m \le x_{cm} + a_m \\ 0, \text{otherwise} \end{cases} \tag{3}$$

where a_m is the half-width of the m-th transducer, which allows to study the effect of the transducer size variation on the ultrasonic wave pattern in the medium, and x_{cm} is the x-coordinate of the mid-point on the m-th transducer. The directivity function for the m-th transducer, $D(\theta_m)$, is given by

$$D(\theta(x_m)) = \frac{c_m^2\left(\frac{1}{2}c_m^2 - sin^2\theta(x_m)\right)cos\theta(x_m)}{2\left(sin^2\theta(x_m) - c_m^2/2\right)^2 + \frac{1}{2}sin^2(2\theta(x_m))\sqrt{c_m^2 - sin^2\theta(x_m)}} \tag{4}$$

where $\theta(x_m)$ is the angle between the line BP and the normal to the surface of the m-th transducer at an arbitrary point x_m, and $c_m = c_{lm}/c_{sm}$ where c_{sm} is the speed of ultrasonic shear waves in the AOD medium due to the m-th transducer. The polarization vector for the m-th transducer, $\vec{d}_p(x_m)$, is given by

$$\vec{d}_p(x_m) = \frac{x - x_m}{r_m}\hat{x} + \frac{z}{r_m}\hat{z} \tag{5}$$

where $\hat{x}$ and $\hat{z}$ are the unit vectors in the x and z directions respectively. The phase shift $\Delta\phi_m$ represents the ultrasonic phase difference between the center of each transducer element, such as

C(x_{cm},0) and the center of the entire transducer array, such as O(0,0), in Fig. 1a. This phase shift is related to the time delays for ultrasonic waves arriving at point Q(x′,z′) from points C(x_{cm},0) and O(0,0), i.e., $\Delta\tau_m = (F' - R'_m)/c_{lm}$, where Q is the point of focus at a distance F' from the point O, and R'_m is the distance CQ [25, 26]. Applying the cosine law of triangle to the triangle QOC, the relationship between the phase shift and time delay can be expressed as

$$\Delta\phi_m = 2\pi F_m \Delta\tau_m = \frac{2\pi}{\Lambda_m} F'\left[1 - \{F'^2 + x_{cm}^2 - 2F' x_{cm} sin\theta_s\}^{1/2}\right] \quad (6)$$

where F_m and $_m$ are the frequency and wavelength of the ultrasonic waves in the AOD medium, respectively, for the m-th transducer. In this study, all of the transducers are considered to emit ultrasonic waves of the same frequency and wavelength. x_{cm} represents the coordinate value of the center of m-th transducer, i.e., x_{cm} is negative for the transducers lying on the –x axis. The steering angle θ_s is considered positive when measured from the z axis in the clockwise direction.

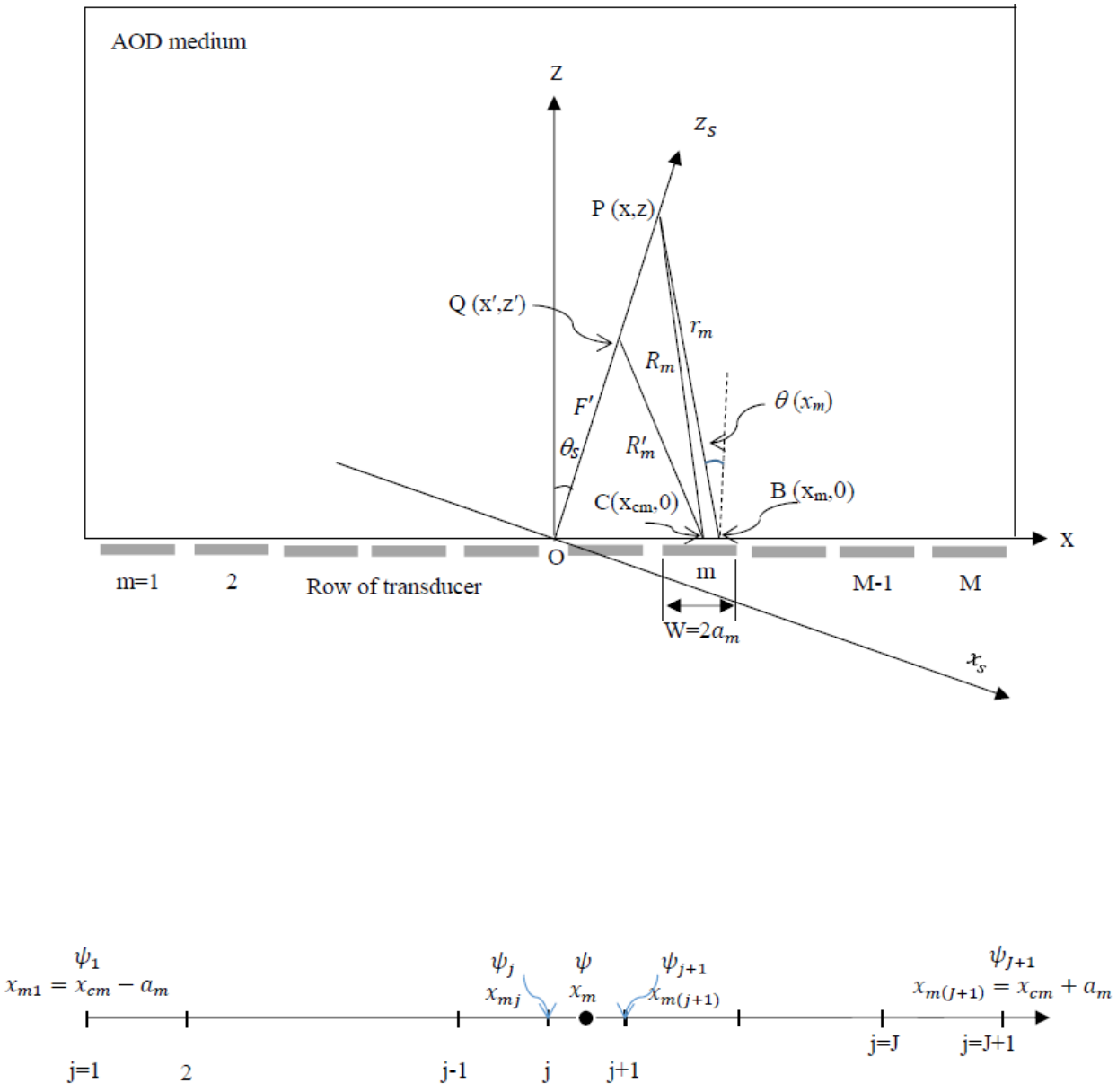

Figure 3-1 Geometry of the AOD medium and piezoelectric transducers for ultrasonic beam steering.

3.2.1. Fourier Model for a Linear Phased Array Transducer

This model is developed by carrying out the integration in Eq. (1) analytically, and the model is named after Fourier because the analytic result involves the sine and cosine functions. When the width of a transducer, $W_m = 2a_m$, is very small, the variation of the directivity function and the polarization vector, $\vec{d}_p(x_m)$, at various points within a given transducer would be very small. Therefore, evaluating these two variables at x_{cm}, i.e., taking $D(\theta(x_m)) \approx D(\theta(x_{cm}))$ and $\vec{d}_p(x_m) \approx \vec{d}_p(x_{cm})$, Eq. (1) can be simplified as

$$\vec{\mathrm{U}}(x,z) = \sum_{m=1}^{M} A_m \int_{x_{cm}-a_m}^{x_{cm}+a_m} \frac{\exp(iK_m r_m)}{r_m} dx_m \tag{7}$$

where $\mathrm{A}_m = \frac{1}{2\pi\rho}\frac{P_m}{c_{lm}^2} D(\theta(x_{cm}))\vec{d}_p(x_{cm}) exp(i2\pi F_m \Delta\tau_m)$ and $K_m = \kappa_m + i\alpha_m$. Using Eq. (2) to change the variable of integration from x_m to r_m, Eq. (7) can be written as

$$\vec{\mathrm{U}}(x,z) = -\sum_{m=1}^{M} A_m \int_{b_l}^{b_u} \frac{\exp(iK_m r_m)}{x-x_m} dr_m \tag{8}$$

where $b_l = \sqrt{z^2 + [x-(x_{cm}-a_m)]^2}$ and $b_u = \sqrt{z^2 + [x-(x_{cm}+a_m)]^2}$. Noting that the oscillating exponential factor $\exp(ik_m r_m)$ in the integrand of Eq. (8) varies rapidly compared to the denominator x-x_m, and x-$x_m \approx x$-x_{cm} for small widths of the transducers, Eq. (8) yields

$$\vec{\mathrm{U}}(x,z) = -\sum_{m=1}^{M} \frac{A_m}{iK_m} \frac{\exp(iK_m b_u) - \exp(iK_m b_l)}{x-x_{cm}} \quad \text{for } x \neq x_{cm} \tag{9}$$

For the case of, $x = x_{cm}$, L'Hospital's rule is applied to Eq. (8) by taking the limit as $x \rightarrow x_{cm}$ to obtain the following expression for the displacement vector field.

$$\vec{\mathrm{U}}(x,z) = 2\sum_{m=1}^{M} A_m \frac{a_m}{\sqrt{z^2+a_m^2}} \exp\left(iK_m\sqrt{z^2+a_m^2}\right) \quad \text{for } x = x_{cm} \tag{10}$$

Eqs. (9) and (10) will be used to analyze the ultrasonic beam steering in the AOD medium due to phase modulation of the piezoelectric transducers.

3.2.2. Filon Model for a Linear Phased Array Transducer

This model is named after Filon because the integration in Eq. (1) is carried out following Filon's quadrature method for trigonometric integrals [27] of the form:

$$\int_{X_l}^{X_u} \psi'(x)\sin(kx)dx \tag{11}$$

In this method, the integral is represented by a sum of integrals over small intervals within the range of integration [X_u,X_l], and the function $\psi'(x)$ is approximated as a polynomial, such as a quadratic function [27] or a linear function [28], to evaluate the integral analytically in each interval.

To apply Filon's method, Eq. (2) is substituted into Eq. (7) to obtain the following expression:

$$\vec{\mathrm{U}}(x,z) = \sum_{m=1}^{M} \frac{A_m}{z} \int_{x_{cm}-a_m}^{x_{cm}+a_m} \frac{\exp\left(iK_m z\psi(x_m)\right)}{\psi(x_m)} dx_m \tag{12}$$

where

$$\psi_m = \sqrt{1 + \left(\frac{x-x_m}{z}\right)^2} \tag{13}$$

The interval of integration, [x_{cm}-a_m, x_{cm}-a_m], is divided into J number of equal intervals with j = 1 for the first point at the lower limit of the integration, i.e., $x_{m1} = x_{cm}$-a_m and $j = J$+1 for the last point at the upper limit of the integration, i.e., $x_{m(J+1)} = x_{cm}$-a_m as shown in Fig. 1b, and the width of each interval is $\Delta x_m = x_{m(j+1)} - x_{mj} = \frac{2a_m}{J}$. The integral in Eq. (12) can be written as a sum of J number of integrals as follows:

$$\vec{\mathrm{U}}(x,z) = \sum_{m=1}^{M} \frac{A_m}{z} \sum_{j=1}^{J} \int_{x_{mj}}^{x_{m(j+1)}} \frac{\exp\left(iK_m z\psi(x_m)\right)}{\psi(x_m)} dx_m \tag{14}$$

To evaluate the integrals in Eq. (14), $\psi(x_m)$ is fitted as a straight line in each interval of integration, $x_{mj} \le x_m \le x_{m(j+1)}$. It should be noted that the coefficient of the sinusoidal function, i.e., $\psi'(x)$ in Eq. (11), is approximated as a polynomial or a linear function in each interval of integration in the original Filon method. This original approach is modified in this study by approximating the denominator, $\psi(x_m)$, as a straight line in each interval of integration, i.e.,

$$\psi(x_m) = \psi_{mj} + \Delta\psi_{mj}\xi_m \tag{15}$$

where $\psi_{mj} = \psi(x_{mj})$, $\Delta\psi_{mj} = \psi_{m(j+1)} - \psi_{mj}$ and $\xi_m = \frac{x_m - x_{mj}}{\Delta x_m}$. Substituting Eq. (15) into Eq. (14), the total displacement vector can be written as

$$\vec{\mathrm{U}}(x,z) = \sum_{m=1}^{M} \frac{A_m}{z} \sum_{j=1}^{J} \Delta x_m \int_0^1 \frac{\exp\left(iK_m z(\psi_{mj} + \Delta\psi_{mj}\xi_m)\right)}{\psi_{mj} + \Delta\psi_{mj}\xi_m} d\xi_m \tag{16}$$

and Eq. (16) is evaluated for the following two cases.

(i) When$\Delta\psi_{mj} = 0$, the integrand in Eq. (16) is independent of ξ_m and the following expression is obtained for the displacement vector.

$$\vec{\mathrm{U}}(x,z) = \sum_{m=1}^{M} \frac{2A_m a_m}{zJ} \sum_{j=1}^{J} \frac{\exp(iK_m z\psi_{mj})}{\psi_{mj}} \tag{17}$$

(ii) When $\Delta\psi_{mj} \neq 0$, the change of variable, $\beta_m = \psi_{mj} + \Delta\psi_{mj}\xi_m$, is applied to Eq. (16) to obtain the following expression:

$$\vec{\mathrm{U}}(x,z) = \sum_{m=1}^{M} \frac{2A_m a_m}{zJ} \sum_{j=1}^{J} \frac{1}{\Delta\psi_{mj}} \int_{\psi_{mj}}^{\psi_{m(j+1)}} \frac{\exp(iK_m z\beta_m)}{\beta_m} d\beta_m \tag{18}$$

which yields the following result in terms of the cosine and sine integrals [29], e.g., Ci(Z) and Si(Z) of an arbitrary argument Z, respectively.

$$\vec{\mathrm{U}}(x,z) = \sum_{m=1}^{M} \frac{2A_m a_m}{zJ} \sum_{j=1}^{J} \frac{1}{\Delta\psi_{mj}} \left[\left\{ Ci\left(K_m z \psi_{m(j+1)}\right) - Ci\left(K_m z \psi_{mj}\right) \right\} + i\left\{ Si\left(K_m z \psi_{m(j+1)}\right) - Si\left(K_m z \psi_{mj}\right) \right\} \right] \quad (19)$$

Eqs. (17) and (19) are used to calculate the displacement vector and the accuracy is verified by comparing with the results of the Fourier and NMGB models.

3.3. Numerical Results and Discussion

TeO_2 is the acousto-optic medium for numerical simulation in this study with a row of M = 22 piezoelectric transducers. Each transducer is operated at the ultrasonic frequency of F=75 MHz each, and at this frequency, the speeds of S and L waves are c_{sm}= 616 ± 10 m/s c_{lm} = 4202 ± 10 m/s, respectively [30]. For the L waves, the ultrasonic wavelength and wavenumber are Λ = 56 μm and κ_m = 1.12×10^5 m^{-1}, respectively. The width and height of each transducer element is W=$20.8\,\mu m$ and H=$2.76\,mm$, which yields the half-width a_m = 10.4 μm. The row of the transducers and the height of the AOD medium are aligned with the x and z axes, respectively, with the origin of this coordinate system lying at the center of the transducer row of pitch S=Λ/2=56 μm as shown in Fig. 3-1a. For the computation in the Filon model, the total number of intervals J = 2, that yields the integration step Δx_m=10.4 μm, which is approximately Λ/5 and sufficiently small to resolve the ultrasonic wavefront for beam steering studies. The pressure exerted on the AOD medium by each transducer is taken as p_m = 1 N/mm^2 and the distance of the point of focus from the origin of the x-z coordinate system is considered to be very large at F' = 1 km. All the required parameters for simulation are listed in Table 2.

Table 2 Simulation parameters for TeO2 crystal at HeNe-laser.

Laser wavelength	632.8 nm at HeNe
AO material	TeO_2 crystal
Refractive index, n	2.26
Sound speed at P-wave	4200 m/s
Sound speed at S-wave	616 m/s
Density of AO medium, ρ	5.99 g/cm^3
Central acoustic frequency	75 MHz
Central acoustic avelength,	56 μm
Acoustic bandwidth	32 MHz
Figure of merit, M_2	793×10^{-15} s^3/kg
Attenuation constant, Γ	15 dB/cm-GHz^2
Attenuation coefficient, α	0.0194/cm

The accuracy of the ultrasonic wave model plays an important role in the design of acousto-optic deflector and the investigation of acousto-optic interactions. So the ultrasonic displacement fields obtained from the NMGB [27] are used to verify the accuracy of the Fourier analytical model and the Filon numerical model for two values of the beam steering angle at the ultrasonic central frequency of F=75 MHz. Fig. 3-2, 3-3 and 3-4 show the results of the NMGB, Fourier and Filon models, respectively, which represent the two-dimensional amplitudes of the ultrasonic displacement field $|U|$ for the beam steering angles of $\theta_s = 0^o$ and 30^o in each figure. These results indicate that the two models of this study are in good agreement with the NMGB model.

The models are also compared along the ultrasonic beam steering axis inside the TeO_2 crystal. Each model yields the displacement vector $\vec{U}$. The scalar magnitude of this vector is $U = \sqrt{\vec{U} \cdot \vec{U}}$, which is a complex variable in this study. The amplitude of U, which is given by the modulus $|U| = \sqrt{UU^*}$, where U* is the complex conjugate of U, is plotted in Fig. 3-5 for the steering angles $\theta_s = 0^o$ and 30^o, indicating that the three models are in good agreement. The curves clearly distinguish the ultrasonic wave propagation domain into two sections, representing the near field and far field regions of the diffraction pattern. The near field regions extend to approximately

56μm and 1.0 mm from the z_s = 0 surface (Fig. 3-1a) for θ_s = 0° and 30°, respectively, before the development of the far-field region. For phased array transducers emitting ultrasonic waves of a single frequency, the near field region is characterized by the amplitude of the field varying rapidly with maximum and minimum values. The reason for this type of variation in the amplitude is that the phase of the waves, which arrive from different regions of the transducer array, vary rapidly from point to point near the transducer plane (z = 0 in Fig. 3-1a) [28], resulting in maximum and minimum amplitudes due to constructive and destructive interferences respectively. The amplitude of the ultrasonic field is nearly constant over a certain range of the far field region, and this region is generally preferred for AOD applications because the uniform acoustic amplitude produces a phase grating of constant refractive index amplitude. Due to good agreements between the NMGB, Fourier and Filon models, and the simplicity of the Fourier model, the following results are obtained using the Fourier model.

Figure 3-6 is a three-dimensional view showing the amplitude $|U|$ along the x and z directions in the TeO_2 medium based on Fourier model for the beam steering angle θ_s= 0°. The ultrasonic wave propagation is calculated from one wavelength above the transducer plane, i.e., from z=56 μm. For θ_s=0°, the amplitude profile is symmetric about the x = 0 line as the wave propagates in the z direction. Fig. 3-6 shows the front and rear views of the amplitude profile. Near the transducer plane, i.e., close to the z = 0 plane, the front view of the amplitude profile exhibits a rectangular diffraction pattern consisting of peaks at the two edges of the rectangle and oscillations of very small amplitude between the edges. This pattern is similar to the profile produced by Gibbs' phenomenon when a rectangle function is synthesized using a Fourier series. The synthesized function overshoots at the edges of the rectangle function and oscillates between the edges. In this study, each transducer emits ultrasonic waves as a rectangle function, and the

resulting diffraction pattern near the transducer plane is denoted as Gibbs' profile. This profile spreads and the overall amplitude decreases as the waves propagate in the x and z directions. Gibbs' profile transforms into the Fresnel diffraction pattern as shown in the rear view at z = 2 mm.

The effect of phase shift or time delay on the amplitude profile is studied in Fig. 3-7. The time delays between two neighboring transducers are taken as $\Delta\tau$ = 0 ns, 0.58 ns, 3.33 ns and 4.71 ns, which correspond to the steering angles θ_s=0°, 5°, 30° and 45°, respectively. Due to different steering angles and, correspondingly, different time delays, the phase characteristics of the ultrasonic waves arriving at the same observation position P(x,z) [Fig. 3-1a] from the transducers would be different. Consequently, the peaks and valleys, which are formed in the resultant displacement field due to the interference of the waves, will be different for these cases as shown in Fig. 3-7. However, the length of the near field is approximately 1 mm for the three cases, and the amplitude is nearly constant in the far field region for the steering angles up to 30°.

The phase plots, i.e., $\tan^{-1}(U_i/U_r)$, where U_i and U_r are the imaginary and real parts of U respectively, are presented in Fig. 3-8 for the steering angles θ_s = 0° and 5° to show that the wavefronts also tilt by the same angle as θ_s. The wavefronts are formed due to the interference of the waves emitted by the phased array transducers. The main, i.e., the zeroth order, diffraction lobe coincides with the steering axis z_s corresponding to the steering angles θ_s= 0° and 5°, and the side lobes, i.e., the higher order diffraction pattern is formed in the transverse direction of the z_s axis. The tilted wavefront implies slanted displacement field that produces an oblique phase grating in the AOD medium. This type of oblique phase gratings can be utilized to increase the deflection angles of laser beams in AODs.

The characteristics of the main and side diffraction lobes are examined in Fig. 3-9, which shows the amplitude of the ultrasonic displacement field along x-axis, for the steering angles θ_s = 0° (left) and 5° (right) at different distances, z = 56 μm, 2 mm, 5 mm and 10 mm, from the transducer plane. The common diffraction features can be observed in both groups of the amplitude profile [31]. Near the source, i.e., close to the transducer plane, typical diffraction pattern of rectangular shape is observed and then the shape changes to the Fresnel diffraction profile in the near-field region. This pattern ultimately evolves into the Fraunhofer profile in the far-field region. In the case of θ_s=0°, the amplitude profiles are symmetric about the z axis since this axis coincides with the steering axis (z_s). On the other hand, the profiles are asymmetric about the z axis in the case of θ_s=5° because the z and z_s axes do not coincide. Gibbs' profile is observed at z = 56 μm, which is near the transducer plane, and the Fresnel diffraction pattern is observed at a distance of z = 10 mm, indicating the existence of near-field diffraction effect over a large distance in the AOD medium. However, the peak of the main lobe shifts to the right, which indicates that the peak lies on the steering axis z_s.

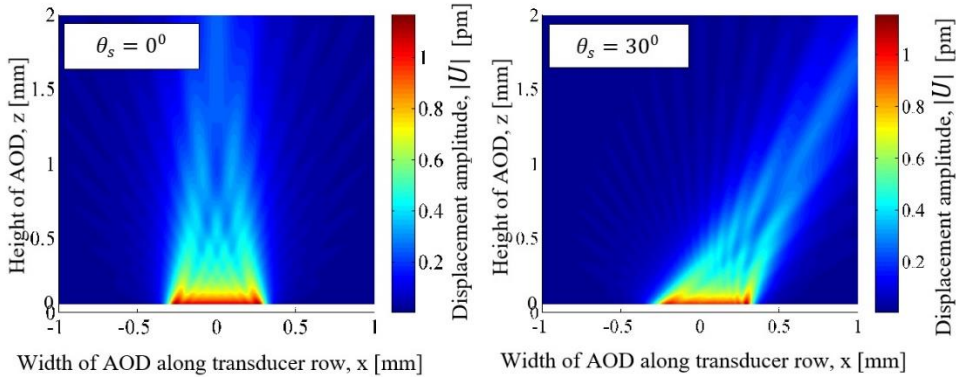

Figure 3-2 Two-dimensional amplitude of the ultrasonic displacement field $|\vec{U}|$ in the AOD medium based on NMGB model for two beam steering angles.

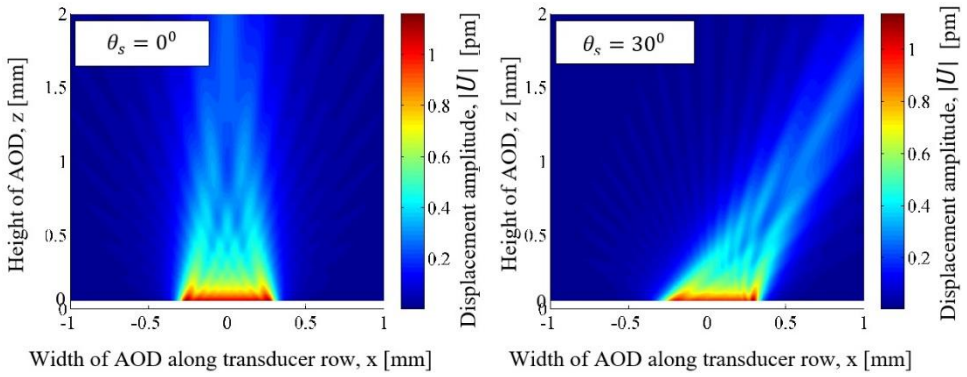

Figure 3-3 Two-dimensional amplitude of the ultrasonic displacement field $|\vec{U}|$ in the AOD medium based on Fourier model for two beam steering angles.

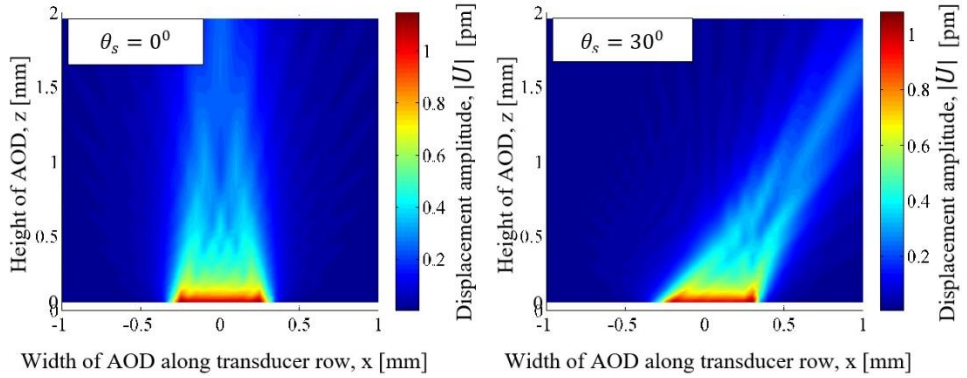

Figure 3-4 Two-dimensional amplitude of the ultrasonic displacement field $|\vec{U}|$ in the AOD medium based on Filon model for two beam steering angles.

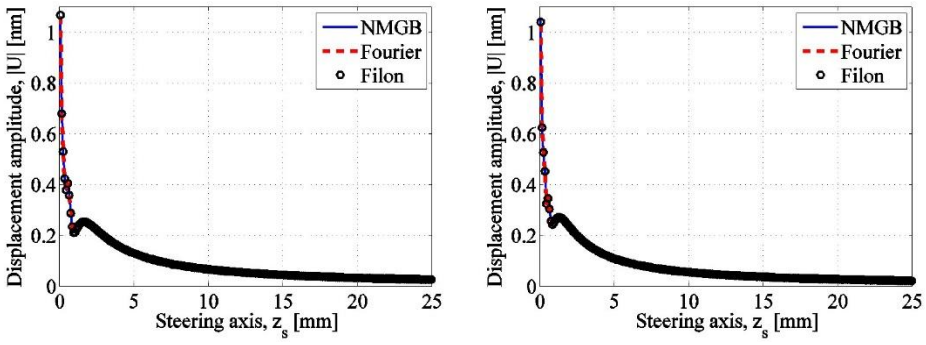

Figure 3-5 Comparison of one-dimensional amplitude of the ultrasonic displacement field $|\vec{U}|$ in the AOD medium based on NMGB, Fourier and Filon models for two steering agnles to verify the accuracy of the models.

We noticed that in Table 2, the attenuation coefficient was found to be 0.0194/cm when the atocustic wave propagating inside the AO meium of TeO_2. So the amplitude of the displacement acouxtic field has no obvious differences whether such attenuation factor is considered or not, givent the usual AO crsytral size in the range of ~5 cm.

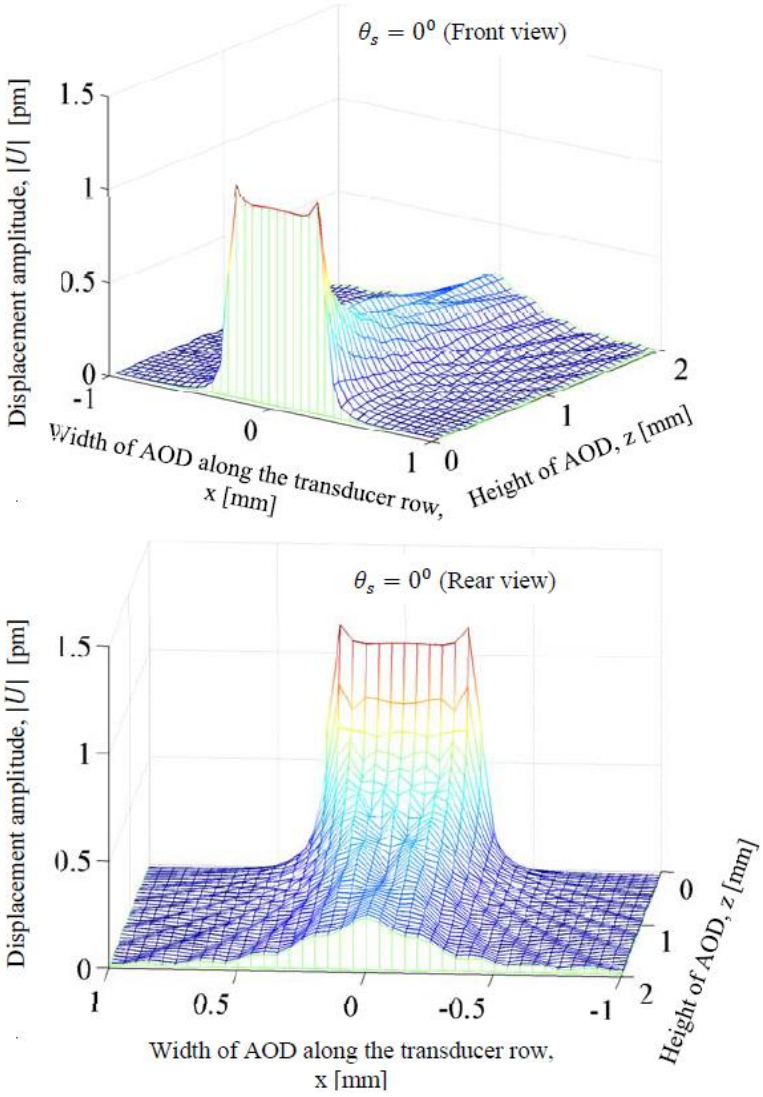

Figure 3-6 Front and rear views of three-dimensional amplitude of the ultrasonic displacement field $|\vec{U}|$ in the AOD medium based on Fourier model with beam steering angle of $\theta_s = 0^o$.

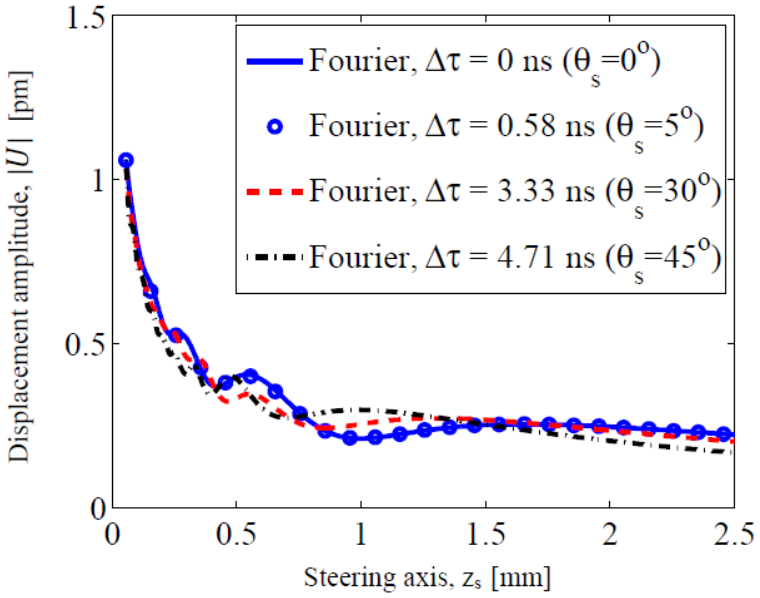

Figure 3-7 Comparison of one-dimensional amplitude of the displacement field $|\vec{U}|$ in the AOD meidum based on Fourier model to study the effect time delay on the amplitude profile.

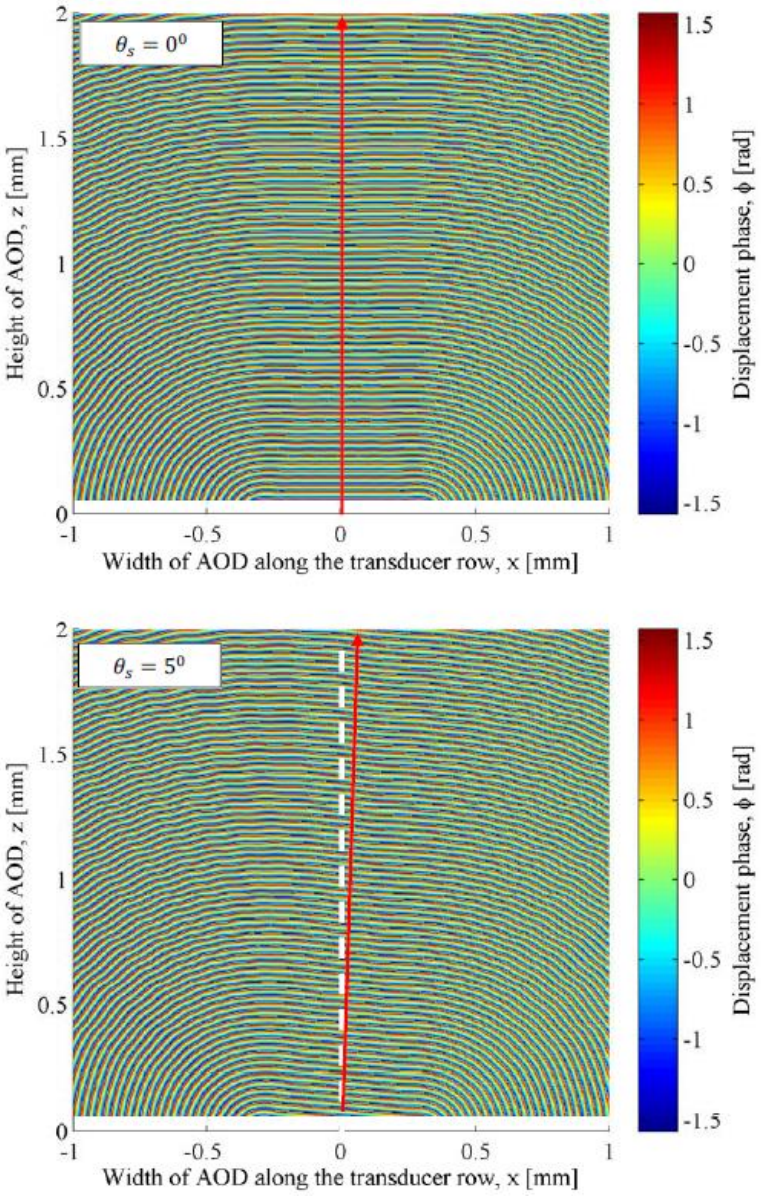

Figure 3-8 Phase plot of the ultrasonic displacement field $|\vec{U}|$ in the AOD medium based on Fourier model for two beam steering angles.

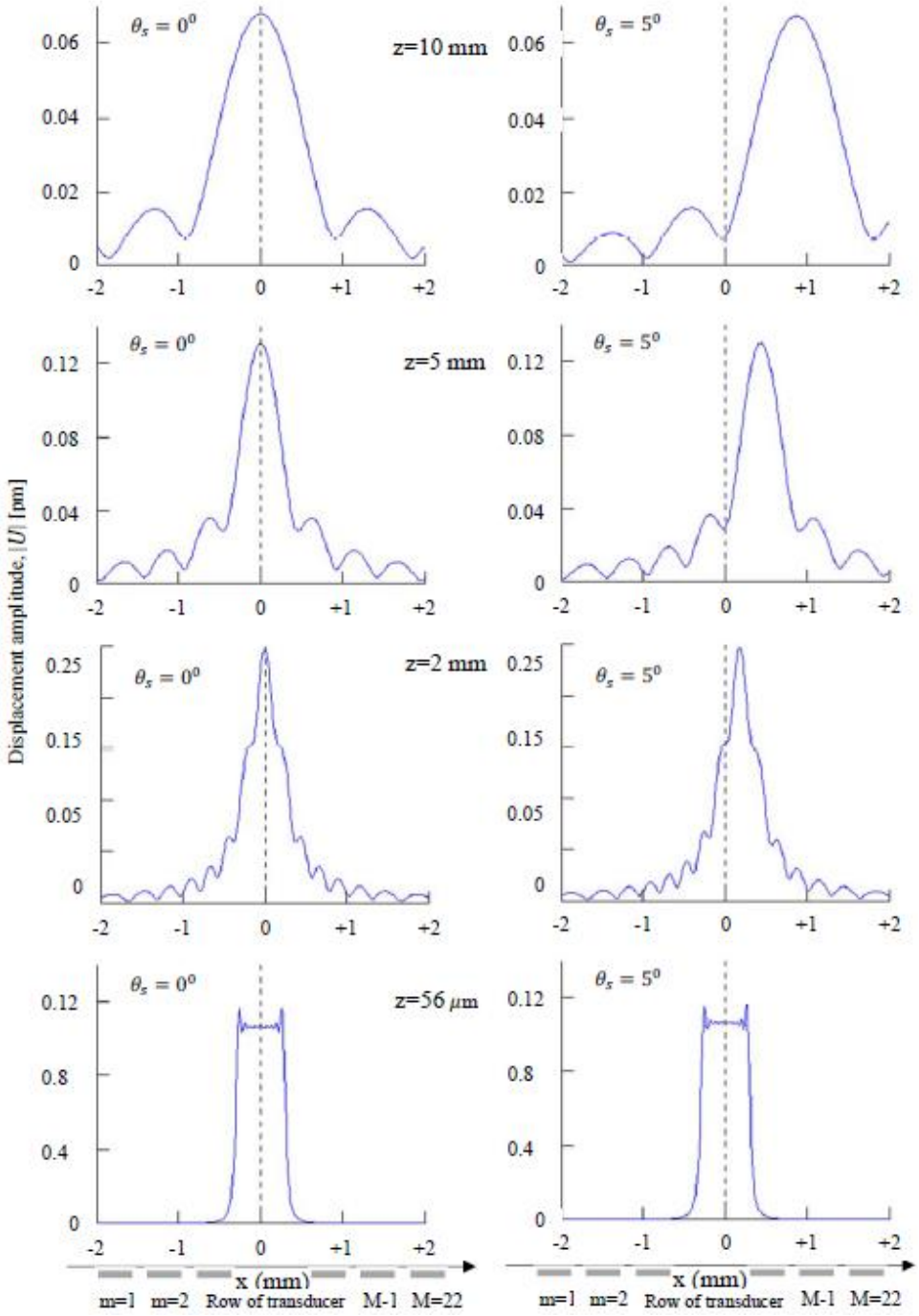

Figure 3-9 Effect of diffraction on the evolution of the amplitude of the ultrasonic displacement field $|\vec{U}|$ at different heights in the AOD medium based o Fourier model for two beam steering angles.

3.4. Summary and Conclusions

Two models called Fourier and Filon models have been developed to analyze the performance of phased array transducers for producing ultrasonic displacement field in AOD media. The Fourier model provides analytic solution for the displacement field, while the Filon model involves numerical integration of the diffraction integral to express the displacement field as a series. The accuracy of these two models is found to be excellent by comparing the results with the NMGB model. By varying the phases of the ultrasonic waves emitted by the transducers, i.e., by operating the transducers at different time delays, the waves can be caused to interfere to produce a diffracted wave pattern in a predetermined direction called the beam steering axis. This type of beam steering can be utilized to scan ultrasonic waves inside materials for non-destructive testing. The amplitude of the composite wave exhibits a rapidly varying wavy characteristic in the near field region and an almost constant value in the far field region. Therefore, nonperiodic and periodic phase gratings would be formed in the near and far field regions, respectively. So the beam steering effect and the far field region can be utilized in AODs to achieve large deflection angles for laser beams. Since the phase grating region extends over a certain volume inside the AOD medium and is primarily affected by the main lobe of the diffraction pattern, the locus of the main lobe is important in AOD applications. The peak of the main lobe is found to lie on the steering axis and the width of the lobe increases along this axis.

3.5. References

[1] C. S. De Silets, Transducer arrays suitable for acoustic imaging, Ph.D. Dissertation, Stanford University, Stanford, California, 1978.

[2] A. Macovski, Ultrasonic imaging using arrays, Proc. IEEE 67 (1979) 484-495.

[3] O. T. Von Ramm and S. T. Smith, Beam steering with linear arrays, IEEE Trans. Biomed. Enging. BME-30 (1983) 438-452.

[4] T. Smith, H. G. Pavy, Jr., and O. T. Von Ramm, High-speed ultrasound volumetric imaging system—Part I: Transducer design and beam steering, IEEE Trans. Ultrasonics, Ferroelectrics, and Frequency Control 38 (1991a) 100-108.

[5] S. T. Smith, H. G. Pavy, Jr., and O. T. Von Ramm, High-speed ultrasound volumetric imaging system-—Part II: Parallel processing and image display, IEEE Trans. Ultrasonics, Ferroelectrics, and Frequency Control 38 (1991b) 109-115.

[6] D. H. Turnbull and S. F. Foster, Beam steering with pulsed two-dimensional transducer arrays, IEEE Trans. Ultrasonics, Ferroelectrics, and Frequency Control 38 (1991) 320-333.

[7] P. N. T. Wells, The present status of ultrasonic imaging in medicine, Ultrasonics 31 (1993) 345-351.

[8] A. E. Weyman, Principles and Practice of Echocardiography, Lea and Febiger, Philadelphia, 1994.

[9] M. T. Buchanan and K. Hynynen, Design and experimental evaluation of an intracavity ultrasound phased array system for hyperthermia, IEEE Trans. Biomed. Enging. 41 (1994) 1178-1187.

[10] H. Wang, E. S. Ebbini, M. O'Donnell, and C. A. Cain, Phase aberration correction and motion compensation for ultrasonic hyperthermia phased arrays: Experimental results, IEEE Trans. Ultrasonics, Ferroelectrics, and Frequency Control 41 (19941) 34-43.

[11] Y. J. Yoon and P. J. Benkeser, Ultrasonic phased arrays with variable geometric focusing for hyperthermia applications, IEEE Trans. Ultrasonics, Ferroelectrics, and Frequency Control 39 (1992) 273-278.

[12] J. - L. Thomas and M. A. Fink, Ultrasonic beam focusing through tissue inhomogeneities with a time reversal mirror: Application to transskull therapy, IEEE Trans. Ultrasonics, Ferroelectrics, and Frequency Control 43 (1996) 1122-1129.

[13] Gerbhardt W. Improvement of ultrasonic testing by phased arrays. Nucl Engng Design 76 (1983) 275–283.

[14] ST. Smith, H.G. Pavy Jr., O.T. Von Ramm, High-speed ultrasound volumetric imaging system - Part II: parallel processing and image display, IEEE Trans. Ultrasonics, Ferroelectrics, and Frequency Control 38 (1991) 109-l15.

[15] D.H. Turnbull, S.F. Foster, Beam steering with pulsed two-dimensional transducer arrays, IEEE Trans. Ultrasonics, Ferroelectrics, and Frequency Control 38 (1991) 320-333.

[16] Von Ramm OT, Smith SW. Beam steering with linear arrays. IEEE Trans Biomed Engng; BME-30 (1983) 438–452.

[17] M. Gottlieb, C.L.M. Ireland and J.M. Ley, Electro-optic and acousto-optic scanning and deflection, New York, Marcel Dekker, Inc., (1983) p.101.

[18] R. Huang, L.W. Schmerr, A. Sedov, Modeling the radiation of ultrasonic phased-array transducers with Gaussian beams, IEEE Transactions on Ultrasonics, Ferroelectrics, and Frequency Control 55 (2008) 2692-2702.

[19] D.J. Vezzetti, Propagation of bounded ultrasonic beams in anisotropic media, Journal of Acoustical Society of America 78 (1985) 1103–1108.

[20] L.W. Schmerr, Fundamentals of Ultrasonic Nondestructive Evaluation, Plenum Press, New York, 1998, p. 543.

[21] X. Zhao and T. Gang, Nonparaxial multi-Gaussian beam models and measurement models for phased array transducers, Ultrasonics 49 (2009) 126-130.

[22] M. Gottlieb, C.L.M. Ireland and J.M. Ley, Electro-optic and acousto-optic scanning and deflection, New York, Marcel Dekker, Inc., 1983, pp. 150-156.

[23] T. Wang, C. Zhang, A. Aleksov, I. Salama and A. Kar, Effect of large deflection angle on the laser intensity profile produced by acousto-optic deflector scanners in high precision manufacturing, Journal of Laser Applications 28 (2016).

[24] T. Wang, C. Zhang, A. Aleksov, I. Salama and A. Kar, Dynamic two-dimensional refractive index modulation for high performance acousto-optic deflector, Optics Express 23 (2015) 33667-33680.

[25] K. Nakahata and N. Kono, 3-D Modelings of an Ultrasonic Phased Array Transducer and Its Radiation Properities in Solid, Ehime University, Hitachi, Ltd, Japan (2012) 60-80.

[26] M. G. Silk, Ultrasonic transducers for nondestructive testing, Adam Hilger Ltd, Bristol, 1984, pp. 76-84 and 90-93.

[27] L. N. G. Filon, Proc. Roy. Soc. Edinburgh, 49 (1928) 38-47.

[28] A. K. Rigler, Note on the Fast Fourier Transform, Journal of the Optical Society of America 58 (1968) 274-275.

[29] M. Abramowitz and I. A. Stegun, Handbook of mathematical functions: with formulas, graphs, and mathematical tables, Dover Publications, Inc., 1964, pp. 231-233.

[30] N. Uchida and Y. Ohmachi, Elastic and photoelastic properties of TeO_2 single crystal, J. Appl. Phys. 40 (1969) 4692-4695

[31] J. W. Goodman, Introduction to Fourier optics, Roberts and Company Publishers, 2005, pp. 84-88.

CHAPTER 4: TWO DIMENSIONAL REFRACTIVE INDEX MODULATION BY PHASED ARRAY TRANSDUCERS IN ACOUSTO-OPTIC DEFLECTORS

4.1. Introduction

The scanning or deflection of light with high performance and broad frequency bandwidth is applied in a number of applications, including light modulators, optical beam deflectors, optical signal processors, optical tunable filters [1,2], RF spectrum analyzers [3], WDM optical communication [4-6], optical tweezers for molecule trapping [7-9], optical image scanners [10-12], optical fringe pattern projectors [13-15], and optical frequency shifters [16,17]. Acousto-optic deflectors (AODs) involve interactions between lasers and acoustic waves, and the deflectors generally operate in three different modes: random access, continuous mode and multi-frequency modes [18]. The performance of the AODs is characterized by the angular resolution for deflecting the laser beam, acoustic frequency bandwidth for modulating the phase grating in the AOD medium, diffraction efficiency to maximize the laser power in the first order diffracted laser beam, and access time to minimize the time for the deflector to steer the beam from one position to another one. The access time, which is the ratio of the laser beam diameter to the acoustic velocity, represents the necessary time for the acoustic wave to propagate through the laser beam.

Therefore, the operation of AODs using the ultrasonic longitudinal or shear waves impacts the performance of the deflector. The longitudinal waves (L-waves) successively compress and stretch the distance between the atomic planes of the AOD material in the direction of the ultrasonic wave propagation, which is similar to the compression and rarefaction phenomena caused by sound waves in air. The shear waves (S-waves), on the other hand, vibrate the atoms at right angles to the direction of the ultrasonic wave propagation. Since the velocity of L-waves is

generally much higher than that of the S-waves, the L-waves allow shorter access time and, consequently, make the deflectors faster than the S-wave mode of operation. The lower velocity of S-waves, however, yields larger deflection angle than in the case of L-waves.

The diffraction efficiency and the deflection scan angle are governed by the elasto-optic or photoelastic effect which states that mechanical stresses modify the refractive index. This effect arises when acoustic waves propagate through a medium since an acoustic wave is a traveling strain or pressure disturbance in the material. Acoustic waves, therefore, can be considered as time-varying deformations of atomic planes in the acousto-optic medium with displaced particles from their equilibrium positions. This mechanical effect of acoustic waves modifies the refractive index of the medium in a periodic pattern and produces dynamic volume phase grating for the laser light passing through the medium. The displacement of the particles can be determined by solving the Christoffel Equation that involves the tensor constitutive relation of the material properties [18]. Kazuyuki and Naoyuki [19] simplified this equation to express the diffraction of acoustic waves as a modified Rayleigh-Sommerfeld integral (mRSI) for the particle displacement vector field, and evaluated the integral numerically to analyze ultrasonic beam steering by phased array transducers. The applications of the phased array technology for beam steering include non-destructive testing of material defects, radar, underwater acoustics, medical diagnostics, and therapeutic treatment. Tiansi et al. [20] evaluated the modified Rayleigh-Sommerfeld integral analytically for transducers of small widths to obtain the displacement vector field that compares well with the numerical solution of the integral [19]. The analytic expression of the integral is used in this study to determine the strain induced in the acousto-optic medium by phased array piezoelectric transducers, and then the two-dimensional variation of the refractive index is calculated using the strain tensor.

4.2. Analytic Model for Numerical Simulation

4.2.1. Strain tensor in the AOD medium due to a row of phased array transducers

In this study, a row of transducers is attached to the AOD medium at the surface z = 0 as shown in Fig. 4-1. The width and length of each transducer are 2a and infinite along the x and y axes, respectively. For each transducer, if P_0 is the pressure exerted on the AOD, cl is the speed of L-waves in the AOD, and κ and α are the wave number and attenuation coefficients of the waves, respectively, the displacement vector of the atoms in the AOD medium can be written as [20] follows for unit length of the medium along the y axis:

for $x \neq x_{cm}$

$$\vec{U}(x,z) = -\frac{P_0}{2\pi\rho c_l^2}\frac{1}{i(\kappa+i\alpha)}\sum_{m=1}^{M} A_m \frac{exp[i(\kappa+i\alpha)b_u]-exp[i(\kappa+i\alpha)b_l]}{x-x_{cm}} \quad (1)$$

and for $x = x_{cm}$

$$\vec{U}(x,z) = \frac{P_0 a}{\pi\rho c_l^2}\frac{1}{\sqrt{z^2+a^2}}\sum_{m=1}^{M} A_m exp\left(i(\kappa+i\alpha)\sqrt{z^2+a^2}\right) \quad (2)$$

where the two integration limits are defined as $b_l = \sqrt{z^2+[x-(x_{cm}-a)]^2}$, $b_u = \sqrt{z^2+[x-(x_{cm}+a)]^2}$ and x_{cm} is the coordinate of the center of m-th transducer on the x axis, i.e., x_{cm} is negative when the transducer is on the –x axis. The expression for Am is given by $A_m = D(\theta(x_{cm}))\vec{d}_p(x_{cm})exp(i\Delta\phi_m)$ with the following definitions of the variables.

Directivity function due to m-th transducer:

$$D(\theta(x_m)) = \frac{c^2\left(\frac{1}{2}c^2-sin^2\theta(x_m)\right)cos\theta(x_m)}{2(sin^2\theta(x_m)-c^2/2)^2+\frac{1}{2}sin^2(2\theta(x_m))\sqrt{c^2-sin^2\theta(x_m)}} \quad (3)$$

Polarization vector due to m-th transducer:

$$\vec{d}_p(x_m) = \frac{x-x_m}{\sqrt{(x-x_m)^2+z^2}}\hat{x} + \frac{z}{\sqrt{(x-x_m)^2+z^2}}\hat{z} \quad (4)$$

Phase shift due to the time delay, $\Delta\tau_m$, for ultrasonic waves arriving at point Q(x′,z′) from points C(x_{cm},0) and O(0,0), i.e., $\Delta\tau_m = (F' - R'_m)/c_l$, where Q is the point of focus at a distance F' from the point O, and R'_m is the distance CQ [19,21]:

$$\Delta\phi_m = 2\pi F\Delta\tau_m = \frac{2\pi}{\Lambda}F'\left[1 - \{F'^2 + x_{cm}^2 - 2F'x_{cm}sin\theta_s\}^{1/2}\right] \quad (5)$$

Here x_{cm} is the angular position of the point of interest P(x,z) in the AOD medium relative to the normal to the surface of m-th transducer at an arbitrary point B (xm,0), i.e., x_{cm} is the angle between this normal and the line BP, and c is the ratio of the speeds of ultrasonic L-waves to the S-waves. $\hat{x}$ and $\hat{z}$ are the unit vectors along the x and z axes respectively. F and Λ are the frequency and wavelength in the AOD medium for the ultrasonic waves generated by each transducer, and θ_s is the steering angle which is taken to be positive when measured from the z axis in the clockwise direction.

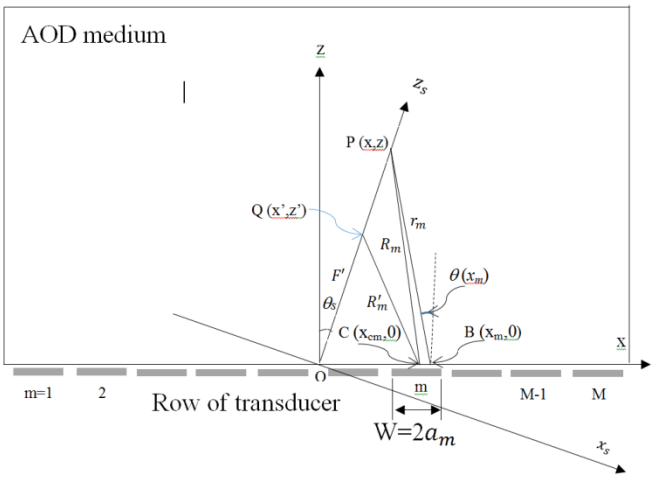

Figure 4-1 Schematic of coordinate system for a modeling of a contact phased array transducer located on solid AO medium.

Equations (1) and (2) yield the displacement vector $\vec{U}(x,z) = u_x(x,z)\hat{x} + u_z(x,z)\hat{y}$, where ux(x,z) and uz(x,z) are the displacement components in the x and z directions, respectively. Using these components, the deformation inside the AOD medium can be characterized by the displacement gradient $\frac{\partial u_i}{\partial u_j}$, where the indices i, j = 1, 2, 3 are the coordinates x, y, z, respectively. The mechanical strains due to this deformation are represented by a second rank strain tensor, $\boldsymbol{S} = [S_{ij}]$, and each strain component is given by the following expression[18,22]:

$$S_{ij} = \frac{1}{2}\left(\frac{\partial u_i}{\partial x_j} + \frac{\partial u_j}{\partial x_i}\right) \tag{6}$$

This strain changes the atomic density within the volume of acoustic wave propagation inside the AOD and, consequently, modifies the refractive index.

4.2.2. Two-dimensional Refractive Index due to Photoelastic Effect

Equation (7) is used to determine the refractive index based on the photoelastic effect. The refractive index is inversely related to the relative impermeability tensor and this tensor depends on the strain tensor by the following expression [23]:

$$\eta_{ij}(\boldsymbol{S}) = \eta_{iju} + \Delta\eta_{ij}(\boldsymbol{S}) = \eta_{iju} + \sum_{k,l} p_{ijkl} S_{kl} \tag{7}$$

where iju is the relative impermeability tensor of the unstrained medium, ij(S) is the change in the relative impermeability tensor due to strain, and p_{ijkl} represents the dimensionless photoelastic coefficient as a fourth-rank tensor. Since the photoelastic tensor is symmetric in i and j, and in k and l, the indices can be contracted to simplify the double indices ij and kl to single indices g and h, respectively, as follows:

$$p_{ijkl} = p_{jikl} = p_{ijlk} = p_{jilk} = p_{gh} \tag{8}$$

where each of $i, j, k, l = 1,2,3$ and each of $g, h = 1,2,3,4,5,6$. Therefore, Eq. (7) can be expressed as

$$\begin{bmatrix}\eta_1\\ \eta_2\\ \eta_3\\ \eta_4\\ \eta_5\\ \eta_6\end{bmatrix} = \begin{bmatrix}\eta_{1u}\\ \eta_{2u}\\ \eta_{3u}\\ \eta_{4u}\\ \eta_{5u}\\ \eta_{6u}\end{bmatrix} + \begin{bmatrix}p_{11} & p_{12} & p_{13} & p_{14} & p_{15} & p_{16}\\ p_{21} & p_{22} & p_{23} & p_{24} & p_{25} & p_{26}\\ p_{31} & p_{32} & p_{33} & p_{34} & p_{35} & p_{36}\\ p_{41} & p_{42} & p_{43} & p_{44} & p_{45} & p_{46}\\ p_{51} & p_{52} & p_{53} & p_{54} & p_{55} & p_{56}\\ p_{61} & p_{62} & p_{63} & p_{64} & p_{65} & p_{66}\end{bmatrix}\begin{bmatrix}S_1\\ S_2\\ S_3\\ S_4\\ S_5\\ S_6\end{bmatrix} \tag{9}$$

where the strain elements S_h are defined by the following rule:

$$\begin{bmatrix}S_1\\ S_2\\ S_3\\ S_4\\ S_5\\ S_6\end{bmatrix} = \begin{bmatrix}S_{xx}\\ S_{yy}\\ S_{zz}\\ 2S_{yz}\\ 2S_{xz}\\ 2S_{xy}\end{bmatrix} \tag{10}$$

The variation of refractive index at different points in the presence of a strain field is given by an index ellipsoid:

$$X^2\left(\frac{1}{{n_u}^2} + \Delta\eta_1\right) + Y^2\left(\frac{1}{{n_u}^2} + \Delta\eta_2\right) + Z^2\left(\frac{1}{{n_u}^2} + \Delta\eta_3\right) + 2YZ\Delta\eta_4 + 2XZ\Delta\eta_5 + 2XY\Delta\eta_6 = 1 \tag{11}$$

where X, Y and Z are not the usual Cartesian coordinates but dimensionless electric displacement components in the x, y and z directions, respectively. $X = \frac{D_x}{\sqrt{2\varepsilon_0\widetilde{U}}}$, $Y = \frac{D_y}{\sqrt{2\varepsilon_0\widetilde{U}}}$ and $Z = \frac{D_z}{\sqrt{2\varepsilon_0\widetilde{U}}}$ with Dx, Dy and Dz as the x, y and z components, respectively, of the electric displacement field D corresponding to the electric field (E) of the laser beam, ε_0 is the permittivity of vacuum and the energy density $\widetilde{U} = \frac{1}{2}\boldsymbol{E}\cdot\boldsymbol{D}$. To determine the variation of the refractive index in the principal directions, Eq. (11) can be written in its normal form by rotating the axes X, Y and Z to the corresponding principal axes X′, Y′ and Z′ at an angle that eliminates the cross terms. Applying the rotation

$$\begin{bmatrix} X \\ Y \\ Z \end{bmatrix} = \begin{bmatrix} cos\theta & 0 & sin\theta \\ 0 & 1 & 0 \\ -sin\theta & 0 & cos\theta \end{bmatrix} \begin{bmatrix} X' \\ Y' \\ Z' \end{bmatrix} \tag{12}$$

to Eq. (11), the following result is obtained,

$$\begin{aligned} &\eta_1(cos^2\theta + \eta_3 sin^2\theta - \eta_5 sin2\theta)X'^2 + \eta_2 Y'^2 \\ &+(\eta_1 sin^2\theta + \eta_3 cos^2\theta + 2\eta_5 cos2\theta)Z'^2 \\ &+(\eta_1 sin2\theta - \eta_3 sin2\theta + 2\eta_5 cos2\theta)X'Z' = 1 \end{aligned} \tag{13}$$

and Eq. (13) is transformed to the normal ellipsoid form by choosing θ so that the coefficient of the cross term X′Z′ is zero, i.e.,

$$\theta = \frac{1}{2} arctan\left(\frac{-2\eta_5}{\eta_1 - \eta_3}\right) \tag{14}$$

The resulting normal form of Eq. (13) yields the following expressions for the refractive indices in the principal directions X′, Y′ and Z′.

$$n_{X'} = 1/\sqrt{\eta_1 cos^2\theta + \eta_3 sin^2\theta - \eta_5 sin2\theta}$$

$$n_{Y'} = \frac{1}{\eta_2}$$

$$n_{Z'} = 1/\sqrt{\eta_1 sin^2\theta + \eta_3 cos^2\theta - \eta_5 sin2\theta} \tag{15}$$

Single-crystal paratellurite (TeO_2) is generally used as an acousto-optic material because of its good photoelastic properties and transparency over a broad wavelength ranging from 0.35-5 μm [18,24]. However, TeO_2 is an anisotropic acousto-optic material both optically and acoustically. For the wavelength 632.8 nm in vacuum and TeO_2 at room temperature, the ordinary and extraordinary refractive indices [24] are n_o = 2.26 and n_e = 2.41, respectively. The photoelastic coefficients for this material are reported as [25]

$$[p_{ij}] = \begin{bmatrix} p_{11} & p_{12} & p_{13} & 0 & 0 & 0 \\ p_{12} & p_{11} & p_{13} & 0 & 0 & 0 \\ p_{31} & p_{31} & p_{33} & 0 & 0 & 0 \\ 0 & 0 & 0 & p_{44} & 0 & 0 \\ 0 & 0 & 0 & 0 & p_{44} & 0 \\ 0 & 0 & 0 & 0 & 0 & p_{66} \end{bmatrix} \quad (16)$$

with p_{11} = 0.0074, p_{12} = 0.187, p_{13} = +0.340, p_{31} = +0.0905, p_{33} = +0.240, p_{44} = -0.170 and p66 = -0.0463. In this study, the refractive index of the material at unstrained condition is taken as $n_u = \sqrt{n_o n_e}$ in Eq. (11). Applying the photoelastic constants to Eq. (9), the impermeabilities I, I = 1, 2, …, 6, are calculated and then the refractive indices in the x and z directions are determined using Eq. (15). Since the transducers are infinitely long in the y direction, the ultrasonic waves induce two-dimensional strains in the x-z plane. Consequently, two principal values of the refractive index, $n_{X'}$ and $n_{Z'}$ in the principal directions X' and Z', respectively, are different from the unstrained refractive index nu and the third principal value, nY´, is the same as nu. A mean value of the refractive index can be calculated as $n_s = \sqrt{n_{X'} n_{Z'}}$ for the strained AOD under the quasi-isotropic approximation which generally holds good for weakly anisotropic media [26]. The two-dimensional change in the refractive index compared to the unstrained AOD is determined as $\Delta n(x,z) = n_s(x,z) - n_u(x,z)$.

4.3. Results and Discussions

Results are obtained for TeO_2 as the AOD medium using the refractive index data at the He-Ne laser wavelength 632.8 nm in vacuum. The speeds of ultrasonic L-waves and S-waves in this material are 4202 ± 10 m/s and 616 ± 10 m/s, respectively, for piezoelectric transducer operating at 75 MHz [17], which yields the acoustic wavelength Λ = 56 μm and the acoustic wave number κ = 1.12×105 m^{-1} inside the AOD medium. In this study, the attenuation coefficient of the

ultrasonic wave is taken as = 0, and the distance for the point of focus is taken as F′ = 106 mm to determine the phase shift or time delay using Eq. (5) for different values of the steering angle θ_s. The half-width, a, and pitch of the transducers are 10.4 μm and 28 μm, respectively. The amplitude of the ultrasonic waves emitted by each transducer is taken to be P_0 = 1 N/mm^2 for the following results unless stated otherwise.

The phased array transducer in this study is a row of 22 planar transducers with the central operating frequency 75 MHz. The pitch of the array is $S = \Lambda/2$ and the width of each element is $W = 0.742S$. The formation of grating lobes is avoided by choosing the difference of the time delay between two adjacent transducers as an integral multiple of half-wavelength, i.e. the pitch $S = \Lambda/2$.

Figures 4-2 and 4-3 show the strain-induced two-dimensional index change in a rectangular region of 2 × 2 mm2 for the beam steering angles $\theta_s = 0^o$ and 30^o, respectively. These two angles correspond to the time delays Δτ = 0 and 3.33 s, respectively. In Fig. 4-2, the ultrasonic waves, which are emitted by each transducer, propagate vertically upward while spreading laterally due to diffraction. Consequently, the overlapping waves interfere to produce a composite wave field in the form of a diffraction pattern. This pattern, therefore, defines the strain field within which the refractive index is modified. The refractive index varies in the z and x directions due to longitudinal and lateral strains in the vertical and horizontal directions, respectively. For Fig. 4-3, on the other hand, the time dalay was so selected that the composite wave field is steered at a certain angle and, therefore, the refractive index pattern is also tilted. These results indicate that the index pattern can be oriented in different directions by varying $\Delta\tau$ to produce dynamic phase grating in the AOD medium for deflecting laser beams at large angles.

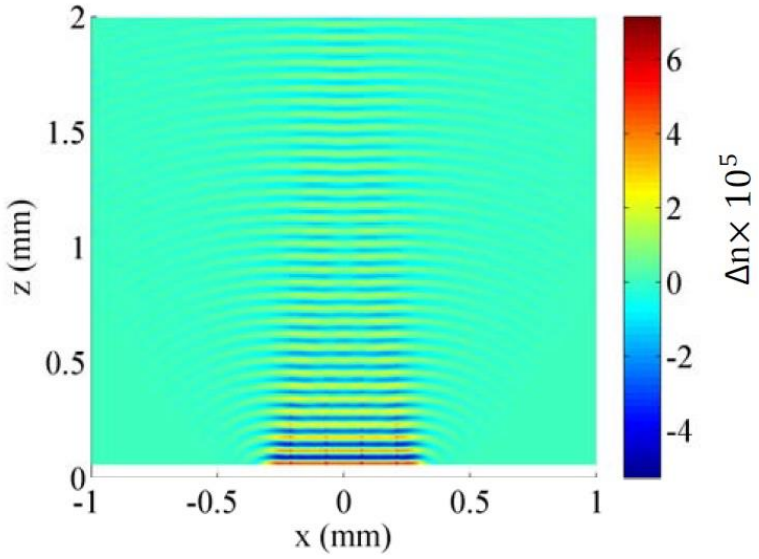

Figure 4-2 Two-dimensional strain-induced index change of Δn with the beam steering angle of $\theta_s = 0^o$.

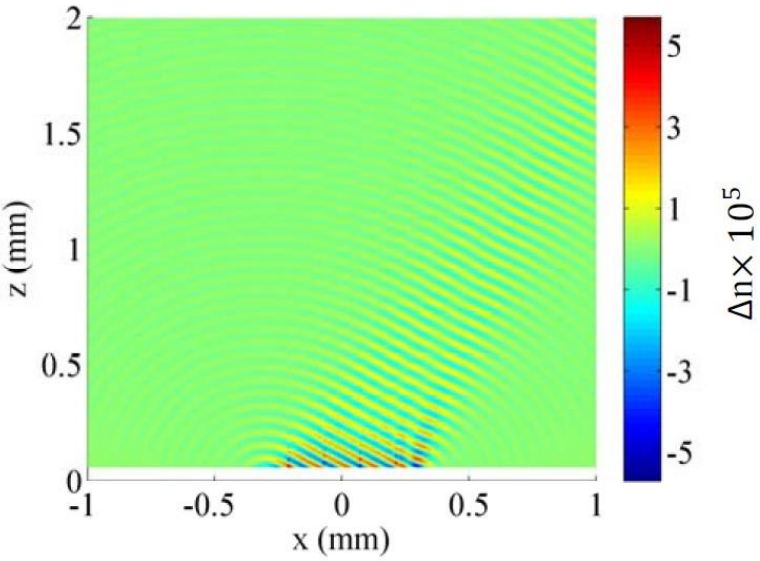

Figure 4-3 Two-dimensional strain-induced index change of Δn with the beam steering angle of $\theta_s = 30^o$.

The two-dimensional features of the index change, Δn(x,z), are examined in Figs. 4-4 and 4-5 that represent the front and rear views of the index profile, respectively, when the acoustic beam steering angle $\theta_s = 0°$ and each transducer emits the acoustic waves as a rectangle function. Near

the transducer plane, the composite acoustic wavefront assumes a rectangular diffraction pattern of peak intensity at the two edges of the rectangle and oscillating intensity of very small amplitude between the edges. This type of pattern is formed due to Gibbs' phenomenon in the Fourier series representation of rectangle functions. Due to this acoustic diffraction pattern, the refractive index has a rectangular profile near the transducer plane as shown in Fig. 4-4. However, the diffraction pattern assumes the Fresnel and Fraunhofer patterns slightly away and far away from the transducer plane, respectively, since the waves spread in the longitudinal and transverse directions. Consequently, the index profile also changes as indicated by the rear view of the index surface in Fig. 4-5.

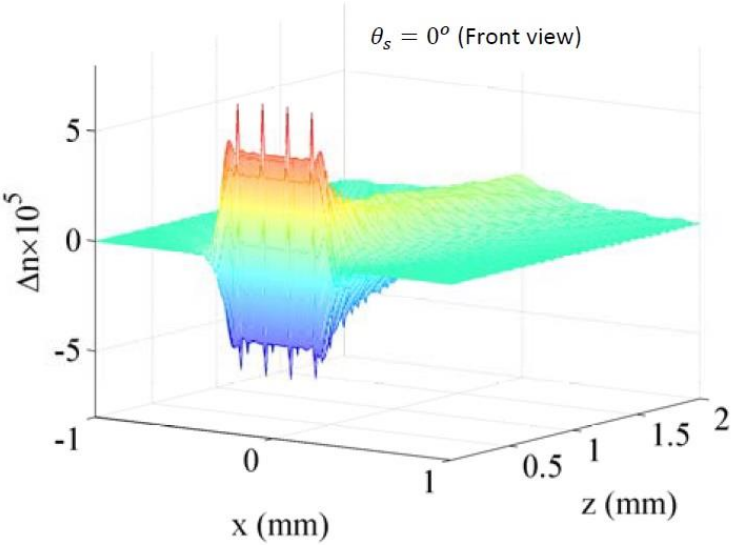

Figure 4-4 Three-dimensional strain-induced index change with the beam steering angle of $\theta_s = 0^o$ (front view).

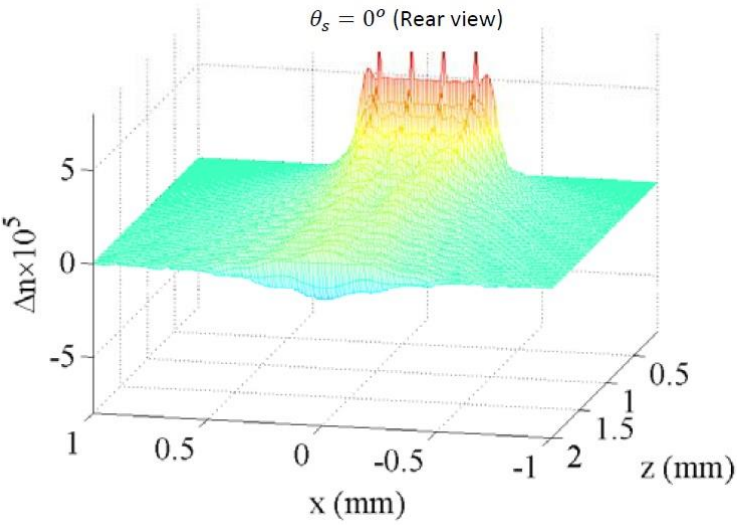

Figure 4-5 Three-dimensional strain-induced index change with the beam steering angle of $\theta_s = 0^o$ (rear view).

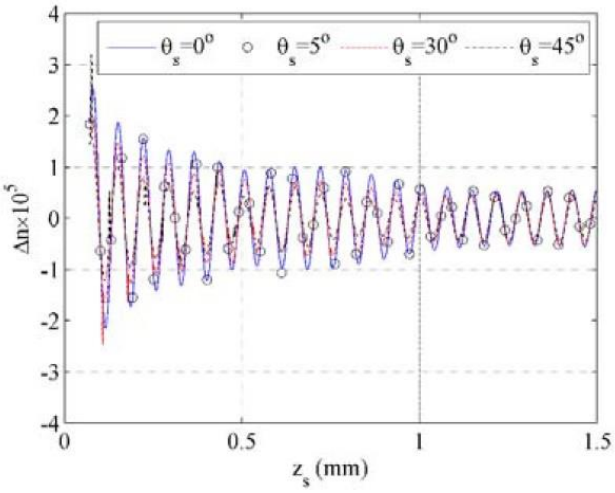

Figure 4-6 One-dimensional strain-induced index change along beam steering axis at center RF frequency of F_c = 59 MHz with varying steering angle of θ_s = 0°, 5°, 30° and 45°.

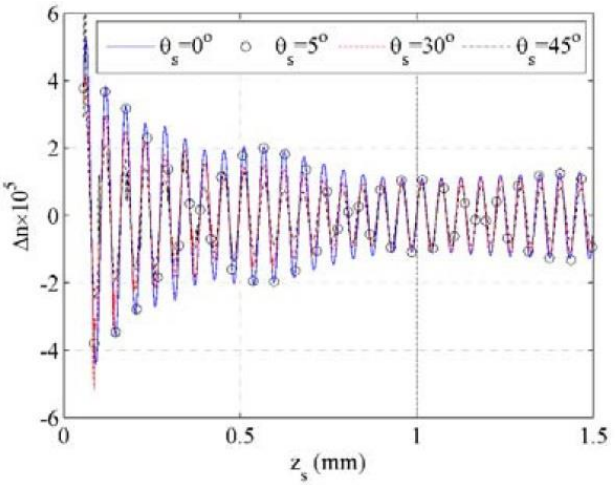

Figure 4-7 One-dimensional strain-induced index change along beam steering axis at center RF frequency of F_c = 75 MHz with varying steering angle of θ_s = 0°, 5°, 30° and 45°.

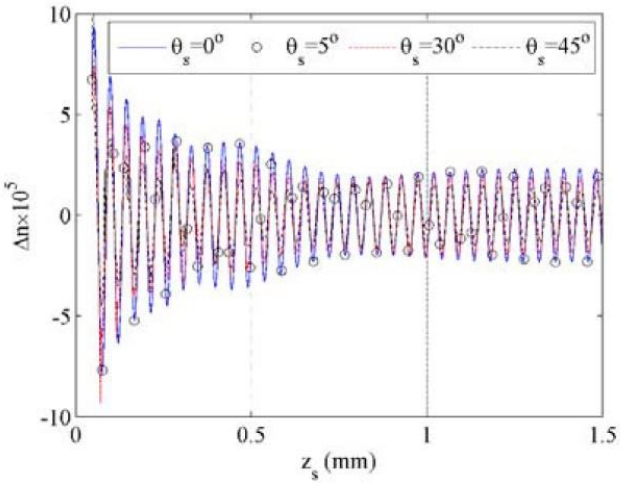

Figure 4-8 One-dimensional strain-induced index change along beam steering axis at center RF frequency of F_c = 91 MHz with varying steering angle of θ_s = 0°, 5°, 30° and 45°.

The effects of transducers having different central RF frequencies, 59, 75 and 91 MHz are presented in Figs. 4-6, 4-7 and 4-8, respectively, for different steering angles. These results show the periodic variation, i.e., the amplitude and wavelength, of Δn along the beam steering axis zs. The steering angles do not affect the wavelength since it is determined by the central RF frequency. It can be observed in the results that the wavelength decreases as the RF frequency increases because the wavelength is inversely proportional to the frequency. At a fixed RF frequency, the steering angle does not affect the periodicity of the index modulation, but the amplitude decreases as the angle increases. The reductions in the amplitude due to the beam steering angle of 45° compared to the zero steering angle are 41% and 38% in the near and far fields respectively. Figures 4-6, 4-7 and 4-8 show that the refractive index modulation (Δn) increases as the RF frequency increases, which is because the wave number, κ,increases as the frequency increases. The mechanical displacement vector of the atoms, on the other hand, are affected by the wave number as indicated by Eqs. (1) and (2), and consequently the strain depends on the frequency. It

is also known that Δn depends on the strain as indicated by Eq. (7). Therefore Δn varies with frequency through the strain term.

The effects of different pressures exerted on the AOD medium by the acoustic waves are studied in Figs. 4-9 and 4-10. For the results in both figures, the pressure exerted by each of the left-half 11 transducers, which lie on the –x axis, is P0 = 1 N/mm2. The pressures exerted by each of the right-half 11 transducers, which lie on the +x axis, are P0 = 0.1 N/mm2 and 10 N/mm2 for Figs. 4-9 and 4-10, respectively. Higher pressure would increase the amplitude of the acoustic waves, resulting in more strain in the AOD medium and, consequently, large modulation in the refractive index. This phenomenon can be observed in Figs. 4-9 and 4-10, which show that Δn is much higher in Fig. 4-10 due to higher right-half pressure than that in Fig. 4-9.

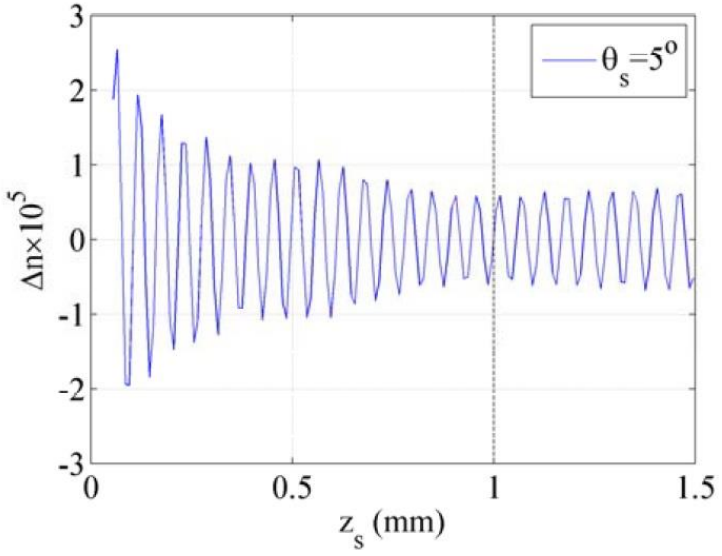

Figure 4-9 One-dimensional strain-induced index change along beam steering axis at center RF frequency of F_c = 75MHz with varying steering angle of $\theta_s = 5^o$ with left-half pressure of P_0 =1N/mm^2 and right-half pressure of P_0 = 0.1 N/mm^2.

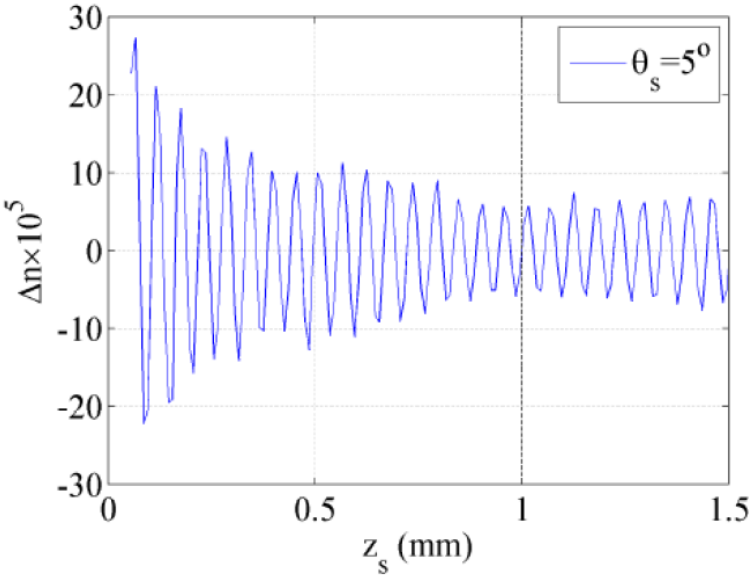

Figure 4-10 One-dimensional strain-induced index change along beam steering axis at center RF frequency of F_c = 75MHz with varying steering angle of $\theta_s = 5^o$ with left-half pressure of P_0 =1N/mm^2 and right-half pressure of P_0 = 10 N/mm^2.

4.4. Conclusions

A mathematical model is presented for generating dynamic phase gratings in AOD media based on strain-induced modulation of two-dimensional refractive index. Phased array transducers enable acoustic beam steering at any arbitrary angle, and this steering effect is utilized to tilt the modulated index profile that can be implemented in AOD devices for deflecting laser beams at large angles. The shape of the index profile and the magnitude of the change in the index are significantly different near the transducer plane compared to far away regions. While the periodicity of the index modulation is determined by the central RF frequency of the transducers, theamplitude of the index modulation is found to decrease as the steering angle increases. The acoustic pressure affects the amplitude of the index profile significantly, yielding higher amplitudes at higher pressures.

4.5. References

[1] M. Gottlieb, C.L.M. Ireland and J.M. Ley, Electro-optic and Acousto-optic Scanning and Deflection (Marcel Dekker, 1983), pp. 158-174.

[2] A. Goutzoulis and D. Pape, Design and Fabrication of Acousto-Optic Devices (Marcel Dekker, 1994), pp. 1-69.

[3] N.J. Berg and J.M. Pellegrino, Acousto-Optic Signal Processing (Marcel Dekker, 1995), pp. 47-80.

[4] G. Aubin, J. Sapriel, V.Ya. Molchanov, R. Gabet, P. Grosso and S. Gosselin, Y. Jaouen, "Multichannel acousto-optic cells for fast optical crossconnect," Electron. Lett. 40, 448–449 (2004).

[5] S.N. Antonov and Yu.G. Rezvov, "Efficient multi-beam Bragg acoustooptic diffraction with phase optimization of a multifrequency acoustic wave," Tech. Phys. 52, 1053–1060 (2007).

[6] L. Zhao, Q. Zhao, J. Zhou, Sh. Tian and H. Zhang, "Two-dimensional multi-channel acousto-optic diffraction," Ultrasonics 50, 512–516 (2010).

[7] K.C. Vermeulen, J. van Mameren, G.J.M. Stienen, E.J.G. Peterman, G.J.L. Wuite and C.F. Schmidt, "Calibrating bead displacements in optical tweezers using acousto-optic deflectors," Rev. Sci. Instrum. 77, 013704-1:6 (2006).

[8] A.E. Wallin, H. Ojala, E. Hæggström and R. Tuma, "Stiffer optical tweezers through real-time feedback control," Appl. Phys. Lett. 92, 224104-1:3 (2008).

[9] A.H. Mack, M.K. Trías and S.G.J. Mochrie, "Precision optical trapping via a programmable direct-digital-synthesis-based controller for acousto-optic deflectors," Rev. Sci. Instrum. 80, 016101-1:3 (2009).

[10] V. Iyer, T.M. Hoogland and P. Saggau, “Fast functional imaging of single neurons using random-access multiphoton (RAMP) microscopy,” J. Neurophysiol. 95, 535–545 (2006).

[11] Y. Kremer, J.-F. Léger, R. Lapole, N. Honnorat, Y. Candela, S. Dieudonné and L. Bourdieu, “A spatio-temporally compensated acousto-optic scanner for twophoton microscopy providing large field of view,” Opt. Exp. 16, 10066–10076 (2008).

[12] P.A. Kirkby, K.M.N. Srinivas Nadella and R.A. Silver, “A compact acousto-optic lens for 2D and 3D femtosecond based 2-photon microscopy,” Opt. Exp. 18, 13720–13744 (2010).

[13] S. Dupont and J.-C. Kastelik, “Wide-band acousto-optic deflectors with high efficiency for visible range fringe pattern projector,” Rev. Sci. Instrum. 78, 105102-1:4 (2007).

[14] S. Dupont and J.-C. Kastelik, “Demonstration of a tunable two-frequency projected fringe pattern with acousto-optic deflectors,” Rev. Sci. Instrum. 79, 056101-1:3 (2008).

[15] S. Dupont, J.-C. Kastelik and M. Pommeray, “Structured light fringe projection setup using optimized acousto-optic deflectors,” IEEE/AMSE Trans. Mechatron. 15, 557–560 (2010).

[16] M.G. Gazalet, M. Ravez, F. Haine, C. Bruneel and E. Bridoux, “Acousto-optic lowfrequency shifter,” Appl. Opt. 33, 1293–1298 (1994).

[17] C. Grebing, S. Koke and G. Steinmeyer, “Self-referencing of optical frequency combs, In: Conference on Lasers and Electro-Optics/International Quantum Electronics Conference.” OSA Technical Digest, Optical Society of America, CTuK5 (2009).

[18] J. Xu and R. Stroud, Acousto-optic Devices: Principles, Design, and Applications (Wiley, 1992), pp. 32-42.

[19] Kazuyuki Nakahata and Naoyuki Kono, 3-D Modelings of an Ultrasonic Phased Array Transducer and Its Radiation Properities in Solid (Ehime University, Hitachi, Ltd, 2012), pp. 60-80.

[20] T. Wang, C. Zhang, A. Aleksov, I. Salama and A. Kar, “Two-dimensional analytic modeling of acoustic diffraction for ultrasonic beam steering by phased array transducers,” Ultrasonics (2016), doi: http:// dx.doi.org/10.1016/j.ultras.2016.12.005

[21] M.G. Silk, Ultrasonic Transducers for Nondestructive Testing (Adam Hilger Ltd, Bristol, 1984), 90-93.

[22] J.M. Liu, Photonic devices (Cambridge University Press, 2005), 357-363.

[23] A. Yariv and P. Yeh, Optical Waves in Crystals (Wiley, 1984), pp. 318-365.

[24] J. C. Kastelik, M. G. Gazalet, C. Bruneel and E. Bridoux, "Acoustic shear wave propagation in Paratellurite with reduced spreading," J. Appl. Phys. 74, 2813-2817 (1993).

[25] N. Uchida and N. Niizeki, Acoustooptic deflection materials and techniques, Proc. IEEE 61, 1073-1092 (1973).

[26] N. Uchida and Y. Ohmachi, "Elastic and Photoelastic Properties of TeO2 Single Crystal," Journal of Applied Physics 40, 4692-4695 (1969).

[27] A.A. Fuki, Yu.A. Kravtsov and O.N. Naida, Geometrical optics of weakly anisotropic media (Gordon and Breach Science Publisher, The Netherlands, 1998), p. 26.

CHAPTER 5: PLANE WAVE DIFFRACTION BY TWO-DIMENSIONAL REFRACTIVE INDEX MODULATION FOR HIGH DIFFRACTION EFFICIENCY AND LARGE DEFLECTIVE ANGLE

5.1. Introduciton

The light diffraction by bulk acoustic waves is a subject of considerable interest due to the wide variety of important applications. Bulkwave acousto-optics enable spatial, temporal and spectral modulations of light in various devices such as acousto-optic deflectors (AODs), acousto-optic modulators and acousto-optic tunable filters. Specifically, in medical applications, AODs enable inertia-free scanning for fast two-dimensional and three-dimensional imaging in multiphoton microscopy on physiologically relevant time scales, overcoming the limitations of galvanometer scanners [1]. Therefore, the diffraction characteristics of acousto-optic gratings have been analyzed extensively. These studies can be broadly distinguished depending on the sizes of the incident light and acousto-optic medium. The light can be plane waves of infinite dimension laterally or a beam of finite size, and similarly, the medium can be the half-space or a crystal of finite length. Additionally, the medium can be isotropic or anisotropic. Kastelik et al. [2] analyzed the performance of anisotropic acousto-optic crystals by introducing a phase mismatch vector in the method of wave vector diagram.

Klein and Cook [3] studied the diffraction of light due to ultrasonic waves by solving a set of coupled first order difference-differential equations that were obtained from the optical wave equation by applying the method of partial wave, which involves resolving the diffracted light into a series of plane waves, and neglecting the second order derivatives of the amplitude of the electric

field. Chu and Tamir [4] presented a rigorous modal approach as well as a coupled mode representation for the diffraction of light in periodically modulated isotropic media. Although the modal theory is accurate, it is tedious and time-consuming for determining the solution. Kogelnik [5] developed a coupled wave approach, which yields analytic results that are accurate around the Bragg angle of incidence for the Klein-Cook parameter greater than 10. Kaspar [6] applied Burckhardt's [7] Floquet method to thick gratings and compared the results to the coupled wave model. Burckhardt's work was only for phase gratings, which was extended to phase-plus-absorption gratings by Kaspar. Gaylord and Moharam [8] analyzed the coupled wave theory and showed the similarity between the coupled wave and modal approaches. These studies were for the diffraction of plane waves rather than the practical case of light beams of finite size. However, Chu and Tamir [9,10], and Chu, Kong and Tamir [11] applied the coupled mode theory to Gaussian beams by considering the beam as a superposition of plane waves. Moharam, Gaylord and Magnusson [12] studied the diffraction of Gaussian beams in acousto-optic media using a modified version of the coupled wave theory, yielding two coupled first order partial differential equations.

Chu and Tamir [3,9,10] simplified the coupled mode equations under the assumption of slowly-varying electric field, $E(x)$, such that $\left|d^2E(x)/dx^2\right| \ll \left|k_{0x}dE(x)/dx\right|$ where k_x is the angular wavevector in the direction, x, of the light propagation. This approximation, which is generally applicable to weakly-modulated media, yielded two coupled first order ordinary differential equations. They solved the equations analytically by neglecting the reflection of energy at the exit boundary and, therefore, the solution is applicable to the propagation of light in very wide media and the half-space. Uchida and Niizeki [13] studied a first order coupled mode theory that yielded analytic solutions for 0 and -1 order modes at the Bragg angle of incidence. However, the application of their model is restricted to weakly modulated media [11] since it neglects the effect

of the exit boundary. Later Kong [14] presented a simplified second order coupled mode approach for both weakly and strongly modulated media and provided analytic solutions for the reflection and transmission coefficients, accounting for the effects at both boundaries of an AOD.

The above-mentioned studies are, however, based on one-dimensional modulation of the refractive index. Only recently, attention has been paid to the effect of two-dimensional refractive index modulation on light diffraction as analyzed by Andre, Guen and Jonnard [15]. In the present paper, the diffraction of plane wave lights is studied in two-dimensionally modulated media of finite size. The bulk acousto-optic grating is formed by the interaction of light and acoustic waves. The acoustic wave is steerable [16,17,18] using a phased array of transducers with suitable time delayed radio-frequency (RF) signals. This mechanism enables meeting the Bragg condition at every RF frequency for incident lights from a fixed source. Consequently, the dynamic acousto-optic volume grating can improve the performance of AODs, such as high diffraction efficiency, large deflection angle and large scan angle.

This project begins by presenting in Section 2 a qualitative argument that supports the coupled-mode theory of light diffraction based on two-dimensional refractive index modulation. An analytic approach is then presented for second-order coupled mode propagation of light in AODs with multiple phased-array transducers. The results are presented in Section 3 for TeO_2 AODs based on the phase, frequency and amplitude modulations of the transducers. Additionally, the diffraction efficiency of this two-dimensional refractive index model is compared to the results of others' one-dimensional refractive index models.

5.2. Theoretical background

5.2.1. Modulation of refractive index in two dimensions

Conventional AODs are operated with a single transducer or an array of transducers assembled in the planar or stepped configuration [19]. In the single transducer configuration, the performance of AODs is limited by the applied RF power, narrow bandwidth, small deflection angle, narrow scan angle and low diffraction efficiency.

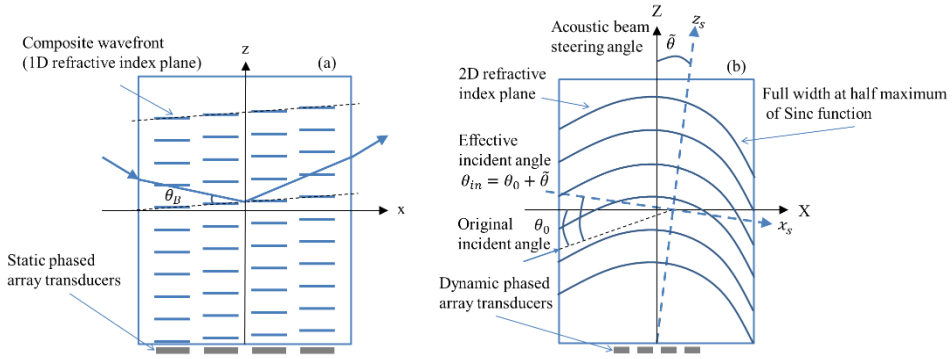

Figure 5-1 Difference in the refractive index profiles due to Fig. 1(a) static phased array transducers in conventional AOD and Fig. 1(b) dynamic phased array transducers in this study.

The array configuration of transducers was introduced to improve the performance of AODs using phase-shifted acoustic waves that create tilted modulation in the refractive index as shown in Fig. 1(a). Each transducer is operated at a relative time delay to generate phase-shifted acoustic waves. These waves propagate through the AOD with a tilted composite wavefront and consequently, the compressed and rarefied atomic layers are also tilted resulting in the slanted refractive index modulation. This type of transducer array improves the deflection scan angle and the diffraction efficiency. However, the time delays are fixed, which produce a static phase grating, and the transducers are relatively large in conventional AODs and therefore, the composite wavefronts

cannot be steered at any arbitrary angles. Dynamic phase gratings can be produced by operating the transducers at different phase shifts and utilizing the interference and diffraction of the acoustic waves. These phenomena produce a tilted grating lobe with the principal direction, z_s, as shown in Fig. 1(b) and the lobe can be steered at any angle of interest by varying the phase shift and amplitude of the acoustic waves.

The steering angle is indicated by θ in Fig. 1(b). Noting that θ_0 is the original incident angle of the light onto the unperturbed medium, the new incident angle becomes $\theta_{in} = \theta_0 + \tilde{\theta}$ for the tilted lobe. Thus the tilted lobe provides a mechanism of automatically changing the incident angle of light without moving the original light source. Also the frequency of the acoustic waves emitted by the transducers can be adjusted to achieve the Bragg angle of incidence, i.e., $\theta_{in} = \theta_B$ for each lobe, which ensures large deflection angle given by θ_{in} and large diffraction efficiency given by the Bragg diffraction condition.

Another aspect of the tilted lobe is two-dimensional modulation of refractive index in the lobe, which results in dynamic two-dimensional gratings in contrast to one-dimensional gratings in conventional AODs. The interference and diffraction of the acoustic waves that form the lobe, also produce a resultant acoustic intensity distribution as a diffraction pattern, typically, in the form of a sinc function. This intensity pattern modifies the refractive index in the transverse direction x_s, and the index variation is taken as a sinc function in this study. On the other hand, the refractive index varies periodically with the period Λ in the longitudinal direction z_s due to the propagation of the acoustic waves in the AOD. These two mechanisms produce a refractive index profile in two dimensions by perturbing the nominal refractive index in the titled lobe as shown in Fig. 2, resulting in a two-dimensional phase grating. Wooh and Shi [20,21,22] showed that multiple

piezoelectric transducers can produce steerable acoustic lobes in a medium, and the longitudinal direction, z_s, coincides with the composite acoustic wavevector $\vec{K}$. A typical two-dimensional index profile in region II, $n_{II}(x,z)$, can be written as:

$$n_{II}(x,z) = n_2(\lambda_0) + \Delta n \cos\left(\frac{2\pi}{\Lambda} z\right)\left(\frac{\sin(bx)}{bx}\right) \tag{1}$$

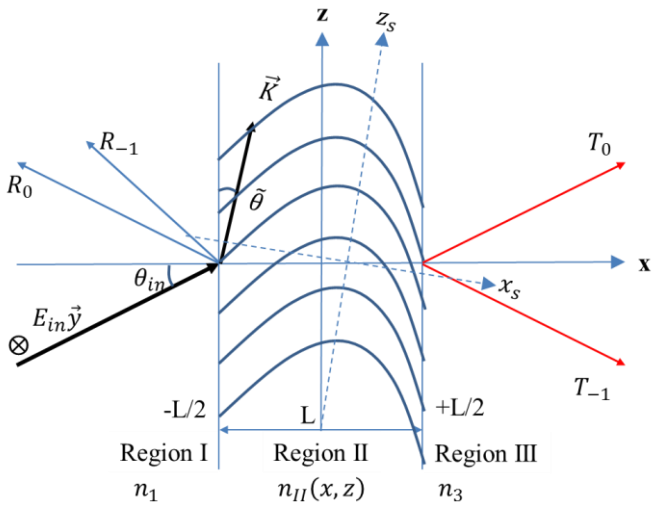

Figure 5-2 Two-dimensional refractive index profile generated by a tilted lobe in an acousto-optic medium.

where $n_2(\lambda_0)$ is the refractive index of the unperturbed acousto-optic medium at the wavelength of the incident light in vacuum, λ_0, and Δn and Λ are the maximum change in the refractive index and the acoustic wavelength in the modulated medium, respectively. The parameter b is a constant that defines the length of the lobe spanned by the central peak of the sinc function with significant contribution to Δn. Considering that x = 0 is at the center of the lobe, x = ±L/2 represent two points on either side of the center, and L is the full width at half maximum of the sinc function, b can be related to L by the following expression:

$$\frac{\sin(bL/2)}{bL/2} = 1/2 \tag{2}$$

The perturbation of the refractive index, δn, from its nominal value, $n_2(\lambda_0)$, is given by [21]:

$$\delta n = -\frac{1}{2} n_2^3(\lambda_0)\, pe \tag{3}$$

where p is the photo-elastic constant and e is the strain tensor due to the mechanical stresses induced by the acoustic wave. The strain amplitude is in the range of 10^{-8} to 10^{-5}, and the photoelastic coefficient is 0.23 for TeO_2 [19]. So the value of δn and consequently, the maximum modulation, Δn, are relatively small for typical AODs.

5.2.2. Second order coupled-mode equations for periodically modulated media

For an incident light of TE polarization in the y direction, the electric field, $E_{II}(x,z)$, satisfies the following scalar wave equation in the modulated region II bounded by $-L/2 \le x \le L/2$,

$$\left[\frac{\partial^2}{\partial x^2} + \frac{\partial^2}{\partial z^2} + k_0^2 n_{II}^2(x,z)\right] E_{II,y}(x,z) = 0 \tag{4}$$

where k_0 is the angular wavenumber of the light at its wavelength in vacuum. Since the light propagates in a periodic medium of periodicity Λ, and the wavevector of the acoustic field, $\vec{K}$, is inclined to the z axis at an angle θ (Fig. 2), the electric field can be expanded in a set of Floquet waves [14],

$$E_{II,y}(x,z) = \sum_{m=-\infty}^{\infty} E_m(x) e^{im\pi/2} e^{i\kappa_{mz} z} \tag{5}$$

where

$$\kappa_{mz} = k_{0z} + mK\cos\theta \tag{6}$$

E_m is the m-th mode electric field, k_{0z} is the z component of the wavevector of the light inside Region II at the incident boundary, and K is the angular wavenumber of the acoustic wave in this

region, i.e., $K = 2\pi / \Lambda$. Applying Eq. (4) to Eq. (3) and equating the coefficient of the m-th Floquet wave to zero, the following second order coupled mode equation is obtained.

$$\frac{d^2 E_m(x)}{dx^2} + \left(k_2^2 - \kappa_{mz}^2\right) E_m(x) + i\frac{\Delta n}{n_2}\left(\frac{\sin(bx)}{bx}\right) k_2^2 \left(E_{m+1} - E_{m-1}\right) = 0 \tag{7}$$

At the Bragg angle of incidence and in its vicinity, only two Floquet modes, i.e., $E_0(x)$ and $E_{-1}(x)$ modes, couple strongly to each other. So Eq. (7) can be reduced to the following two coupled equations by neglecting the higher order modes and taking θ as zero.

$$\frac{d^2 E_0}{dx^2} + \frac{\phi_1^2}{L^2} E_0 = i\frac{\phi\phi_1}{L^2}\left(\frac{\sin(bx)}{bx}\right) E_{-1} \tag{8}$$

$$\frac{d^2 E_{-1}}{dx^2} + \frac{\phi_1^2 \beta^2}{L^2} E_{-1} = -i\frac{\phi\phi_1}{L^2}\left(\frac{\sin(bx)}{bx}\right) E_0 \tag{9}$$

Three dimensionless parameters, ϕ_1, ϕ and β, appear in Eqs. (8) and (9), which are given by:

$$\phi_1 = k_0 n_2 L \cos\theta_2 \tag{10}$$

$$\phi = \frac{k_0 \Delta n L}{\cos\theta_2} \tag{11}$$

$$\beta = \sqrt{1 - \frac{Q}{\phi_1}(1-\alpha)} \tag{12}$$

where Q and α are Klein-Cook parameter and angle ratio, respectively, which are defined below. The relations $k_{0z} = k_2 \sin\theta_2$ and $k_2 = n_2 k_0$ are used to obtain ϕ_1 while deriving equations (8) and (9), where θ_2 is the angle of refraction at the incident boundary of the AOD medium. ϕ_1 is a phase parameter for the light in the unperturbed medium.

ϕ, which is obtained using the relation $k_2 = n_2 k_0$ while deriving Eqs. (8) and (9), represents the phase difference due to the change in the optical path length ΔnL. This parameter can be varied

by operating the piezoelectric transducer in the amplitude modulation mode since Δn depends on the amplitude of the acoustic wave. The third parameter β includes the light-sound interactions through the Klein-Cook parameter Q and the angle ratio α. The relations $k_{0z} = k_2 \sin\theta_2$ and $k_2 = n_2 k_0$ are used to obtain β while deriving equations (8) and (9).

Q is given by [23]:

$$Q = \frac{K^2 L}{n_2 k_0 \cos\theta_2} \tag{13}$$

It classifies the light diffraction process into three regimes: (i) Raman-Nath diffraction in thin gratings corresponding to $Q \ll 1$, (ii) Bragg diffraction in thick gratings corresponding to $Q \gg 1$, and (iii) the transition region for $Q \approx 1$. The angle ratio, α, is defined as:

$$\alpha = \frac{2k_0 \sin\theta_{in}}{K} \tag{14}$$

It represents the ratio of the sine functions of the incident and Bragg angles since $\sin\theta_B = K/(2k_0)$, where θ_B is the Bragg angle measured outside the acousto-optic medium. The sine of an angle is approximately equal to the angle itself for small angles, and under this condition, α is a measure of the incident angle normalized by the Bragg angle. α = 1 indicates $\theta_{in} = \theta_B$ and $\alpha > 1$ corresponds to $\theta_{in} > \theta_B$. The angle ratio parameter can be varied by operating the piezoelectric transducers in the frequency modulation mode since K depends on the frequency of the acoustic wave.

5.2.3. Solutions of the reduced coupled mode equations

Equations (8) and (9) are solved for 0 and -1 order Floquet modes $E_0(x)$ and $E_{-1}(x)$, respectively, by the method of variation of parameters. The resulting expressions, which involve the sine integral, $Si(z)$, and cosine integral, $Ci(z)$, [24], are given below:

$$
\begin{aligned}
&E_0(x) = A_1 e^{i\frac{\phi_1}{L}x} + A_2 e^{-i\frac{\phi_1}{L}x} \\
&+\frac{i\phi}{4bL} B_1 \sum_{j=1}^{4}\left[1-2\delta_{j1}-2\delta_{j2}\right] e^{i(-1)^{j-1}\frac{\phi_1}{L}x}\left[Si\left(b_{1j}x\right)-iCi\left(b_{1j}x\right)\right] \\
&+\frac{i\phi}{4bL} B_2 \sum_{j=1}^{4}\left[1-2\delta_{j1}-2\delta_{j2}\right] e^{i(-1)^{j-1}\frac{\phi_1}{L}x}\left[Si\left(b_{2j}x\right)-iCi\left(b_{2j}x\right)\right] \\
&+\frac{\phi^2}{4\beta L^2} \sum_{j=1}^{2}(-1)^j e^{i(-1)^{j-1}\frac{\phi_1}{L}x} \int_0^x e^{i(-1)^{2-j}\frac{\phi_1}{L}x''} \frac{\sin\left(bx''\right)}{bx''} \\
&\times\left[\sum_{p=1}^{2}(-1)^p e^{i(-1)^{p-1}\frac{\phi_1\beta}{L}x''} \int_0^{x''} e^{i(-1)^{2-p}\frac{\phi_1\beta}{L}x'} \frac{\sin\left(bx'\right)}{bx'} E_0\left(x'\right)dx'\right]dx''
\end{aligned}
\tag{15}
$$

$$
\begin{aligned}
&E_{-1}(x) = B_1 e^{i\frac{\phi_1\beta}{L}x} + B_2 e^{-i\frac{\phi_1\beta}{L}x} \\
&+\frac{i\phi}{4bL\beta} A_1 \sum_{j=1}^{4}\left[1-2\delta_{j1}-2\delta_{j2}\right] e^{i(-1)^{j-1}\frac{\phi_1\beta}{L}x}\left[Si\left(a_{1j}x\right)-iCi\left(a_{1j}x\right)\right] \\
&+\frac{i\phi}{4bL\beta} A_2 \sum_{j=1}^{4}\left[1-2\delta_{j1}-2\delta_{j2}\right] e^{i(-1)^{j-1}\frac{\phi_1\beta}{L}x}\left[Si\left(a_{2j}x\right)-iCi\left(a_{2j}x\right)\right] \\
&+\frac{\phi^2}{4\beta L^2} \sum_{j=1}^{2}(-1)^j e^{i(-1)^{j-1}\frac{\phi_1\beta}{L}x} \int_0^x e^{i(-1)^{2-j}\frac{\phi_1\beta}{L}x''} \frac{\sin\left(bx''\right)}{bx''} \\
&\times\left[\sum_{p=1}^{2}(-1)^p e^{i(-1)^{p-1}\frac{\phi_1}{L}x''} \int_0^{x''} e^{i(-1)^{2-p}\frac{\phi_1}{L}x'} \frac{\sin\left(bx'\right)}{bx'} E_{-1}\left(x'\right)dx'\right]dx''
\end{aligned}
\tag{16}
$$

where δ_{j1} and δ_{j2} are Kronecker's delta functions and the other auxiliary parameters are defined as:

$$
\begin{aligned}
&b_{11} = a_{24} = b - \frac{\phi_1}{L}(1-\beta), b_{21} = a_{21} = b - \frac{\phi_1}{L}(1+\beta) \\
&b_{12} = a_{12} = -b + \frac{\phi_1}{L}(1+\beta), b_{22} = a_{13} = -b + \frac{\phi_1}{L}(1-\beta) \\
&b_{13} = a_{22} = -b - \frac{\phi_1}{L}(1-\beta), b_{23} = a_{23} = -b - \frac{\phi_1}{L}(1+\beta) \\
&b_{14} = a_{14} = b + \frac{\phi_1}{L}(1+\beta), b_{24} = a_{11} = b + \frac{\phi_1}{L}(1-\beta)
\end{aligned}
\tag{17}
$$

A_1, A_2, and B_1 and B_2 are the constants pertaining to the homogeneous solutions for 0 and -1 order Floquet modes, $E_0(x)$ and $E_{-1}(x)$, respectively. On the right hand side in Eqs. (16) and (17), the first two terms are these two modes in the unperturbed acousto-optic medium and the third and fourth terms represent the interaction between these two modes in the perturbed medium for transferring energy between them. The last term in each equation represents higher order effects for the interaction between the modes involving $(\Delta n)^2$ through the ϕ^2 term. This last term also shows the self-effect of each mode because the electric field of a mode at a given point x, e.g., $E_0(x)$, is affected by the distribution of the field over the entire distance ranging from 0 to x. Eqs. (16) and (17) are essentially Volterra integral equations which can be solved by the method of successive approximations [25]. As a first approximation, however, only the first four terms have been considered in this study to calculate $E_0(x)$ and $E_{-1}(x)$.

5.2.4. Reflection and transmission due to the modulated medium

In region I, the overall electric field, which consists of the incident and reflected fields, can be expressed as:

$$
E_{I,y}(x,z) = G_m e^{ik_{in,mx}x} e^{ik_{in,mz}z} + r_0 e^{-i\kappa_{1,0x}x} e^{i\kappa_{0z}z} + r_{-1} e^{-i\kappa_{1,-1x}x} e^{i\kappa_{-1z}z} \tag{18}
$$

where G_m is the amplitude of m-th plane wave component of the input light, $k_{in,mx}$ is the x component of the wavevector of the incident m-th plane wave component, r_0 and r_{-1} are the field reflection coefficients for 0 and -1 Floquet modes, respectively, and $\kappa_{1,0x}$ and $\kappa_{1,-1x}$ are the x components of the wavevectors for 0 and -1 Floquet modes, respectively, in region I, as given later in this section. κ_{0z} and κ_{-1z} are the z components of the wavevectors for 0 and -1 Floquet modes, respectively.

In region II, the electric field takes the form:

$$E_{II,y}(x,z) = E_0(x)e^{i\kappa_{0z}z} - iE_{-1}(x)e^{i\kappa_{-1z}z} \tag{19}$$

where $E_0(x)$ and $E_{-1}(x)$ are the solutions to the two Floquet modes given by Eqs. (15) and (16), respectively.

In region III, the electric field consists of the transmitted components of 0 and -1 order modes, and there is no reflection from this region back to region II. So the transmitted electric field in region III can be written as:

$$E_{III,y}(x,z) = t_0 e^{i\kappa_{3,0x}x}e^{i\kappa_{0z}z} + t_{-1}e^{i\kappa_{3,-1x}x}e^{i\kappa_{-1z}z} \tag{20}$$

where t_0 and t_{-1} are the field transmission coefficients for 0 and -1 Floquet modes, respectively, and $\kappa_{3,0x}$ and $\kappa_{3,-1x}$ are the x components of the wave vectors for 0 and -1 Floquet modes, respectively, as given below.

The $\hat{x}$ components of the wave vectors pertaining to the Floquet modes are given by:

$$\kappa_{r,mx} = \sqrt{k_r^2 - \kappa_{mz}^2} \tag{21}$$

where $\kappa_{r,mx}$ is the x component of the wavevector in region r, r = 1 or 3, respectively, for m-th Floquet mode. Eqs. (18-20) contain eight unknowns: r_0, r_{-1}, A_1, A_2, B_1, B_2, t_0 and t_{-1}, which are

determined by applying the boundary conditions that the tangential electric and magnetic fields are continuous at the incident (x = -L/2) and exit (x = L/2) boundaries of the acousto-optic medium. The boundary conditions involving the normal components, which require that the normal component of the electric displacement vector and the normal component of the magnetic flux density vector be continuous at the boundaries, are not considered because these two conditions are not independent of the two tangential conditions [26]. Since the tangential magnetic field H_z is given by Maxwell's equation as $H_z = \frac{1}{i\omega\mu}\frac{\partial E_y}{\partial x}$, where μ is the permeability of a given medium, the boundary conditions can be written as follows for nonmagnetic media, i.e., $\mu = 1$.

$$\text{At } x = -L/2,\ E_{I,y}(x,z) = \mathrm{E}_{II,y}(x,z) \text{ and } \frac{\partial E_{I,y}}{\partial x} = \frac{\partial E_{II,y}}{\partial x} \tag{22}$$

$$\text{At } x = L/2,\ E_{II,y}(x,z) = E_{III,y}(x,z) \text{ and } \frac{\partial E_{II,y}}{\partial x} = \frac{\partial E_{III,y}}{\partial x} \tag{23}$$

These four boundary conditions must be satisfied for each mode at all values of z. So eight linear simultaneous equations can be obtained by equating the coefficients of the waveform of each mode, i.e., $e^{i\kappa_{0z}z}$ or $e^{i\kappa_{-1z}z}$, to zero for determining the eight unknowns. The Crammer rule is applied in this study to calculate these unknown coefficients.

The solution is verified by checking that the Conservation of Energy (CoE) is satisfied. The transmitted and diffracted electric fields, E_0 and E_{-1}, respectively, are related to the electric field of the incident light, E_{in}, by the CoE as stated below:

$$\left(\frac{\kappa_{1,0x}}{k_{1x}}\right)|r_0|^2 + \left(\frac{\kappa_{1,-1x}}{k_{1x}}\right)|r_{-1}|^2 + \left(\frac{\kappa_{3,0x}}{k_{1x}}\right)|t_0|^2 + \left(\frac{\kappa_{3,-1x}}{k_{1x}}\right)|t_{-1}|^2 = 1 \tag{24}$$

for the case of $G_m = 1.0$.

5.3. Results and discussion

In this study, the acousto-optic medium is a TeO_2 crystal, which is transparent in the wavelength range of 0.35 to 5 μm [27,13], and the incident light is a plane wave of wavelength λ_0 = 632.8 nm in vacuum. So the angular wavenumber of the light in vacuum is $k_0 = 9.93\times10^6$ m^{-1}. The nominal refractive index of the crystal is n_2 = 2.26 at this wavelength, which is the refractive index for the ordinary light [28]. Although TeO_2 is a uniaxial positive crystal, it can be treated as an isotropic medium for longitudinal acoustic waves and transverse electric polarized light. The velocity of sound in the crystal is V = 4260 m/s in the crystallographic direction [001] for the longitudinal mode [28] that results in Λ = 56 μm and $K = 1.12\times10^5$ m^{-1}. So the Bragg angle of incidence is θ_B = 0.324° at 75 MHz. The length of the modulated region is L = 2.24 cm, which yields Q = 4π and therefore, the AOD is operated in the Bragg regime since Q >> 1.

Results are obtained for different cases by varying the frequency of the acoustic waves as well as their amplitudes and phases. The effect of amplitude modulation manifests as the index modulation Δn, and the phase-shifting corresponds to grating lobes at different steering angles, θ, resulting in a new incident angle $\theta_0+\theta$ [Fig. 1(b)]. This angle would be the Bragg angle of incidence if the acoustic frequency for the lobe is chosen properly using the Bragg diffraction condition, i.e., $\sin\left(\theta_0+\theta\right)=\lambda_0 F/\left(2V\right)$. Thus the effect of phase-shifting manifests as operating the AOD under the Bragg diffraction condition for each lobe to achieve large deflection angle, $\theta_0+\theta$, and high diffraction efficiency at any frequency. Four parameters, the index modulation strength Δn, the acoustic frequency F, the angle of incidence θ_{in} and the grating length L, are found to affect the optimal performance of the AOD.

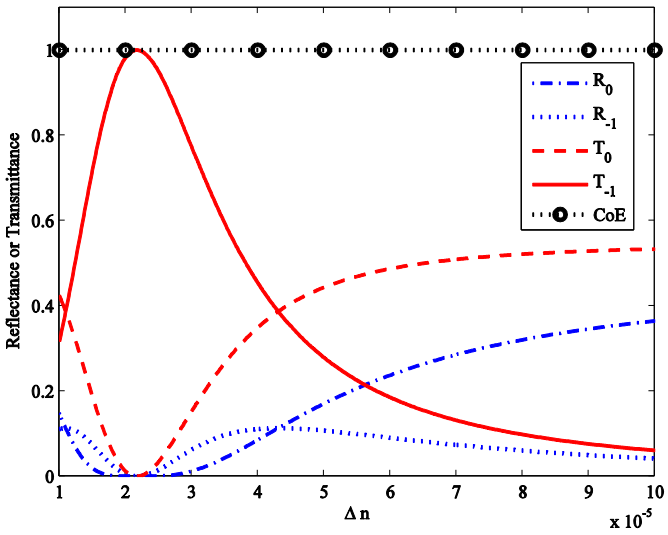

Figure 5-3 Reflectance and Transmittance as a function of the index modulation strength Δn with L = 2.24 cm, Q = 4π and F = 75 MHz at Bragg incidence angle of 0.324o.

The solutions of the above-mentioned eight linear algebraic equations yield the reflection and transmission coefficients, r_0, r_{-1}, t_0 and t_{-1}, for 0 and -1 order modes. The corresponding reflectance and transmittance are given by $R_0 = |r_0|^2, R_{-1} = |r_{-1}|^2$ and $T_0 = |t_0|^2, T_{-1} = |t_{-1}|^2$, which are plotted in Fig. 3 as a function of the index modulation strength Δn for $n_1 = n_3 = 1.0$. At the index modulation strength $\Delta n = 2.2 \times 10^{-5}$, the transmittance, T_{-1}, of -1 order mode is maximum with the value unity and correspondingly the transmittance, T_0, of 0 order mode is minimum with the value zero. The reflectances are also zero at this critical point. The index modulation strengths of 1.1×10^{-5} and 4.3×10^{-5} are a pair of turning points because the trend in the variation of the transmittances reverses, i.e., $T_{-1} < T_0$ after these two points. The fifth graph, which is designated by CoE, is determined using the conservation of energy as given by the left hand side of Eq. (24).

Its value of unity for different values of Δn validates the results of the coupled mode theory for two-dimensional refractive index modulation.

The diffraction efficiency is plotted as a function of the incident angle θ_{in} in Fig. 4 for a fixed acoustic frequency of 75 MHz and different index modulation strengths. It has the maximum value of unity at the Bragg angle of $\theta_{in} = 0.324^{o}$ at this frequency for the optimal index change of 2.2×10^{-5}. The curves are symmetric about this angle, indicating that the diffraction efficiency reduces by the same amount if the incident light is misaligned to either side of the Bragg angle of incidence. As the index modulation strength deviates more from the optimal Δn, the diffraction efficiency decreases further and varies with θ_{in} more nonuniformly. Good uniformity in the curve shows that the AOD can be operated at nearly 100% diffraction efficiency over a relatively large range of the incident angle and therefore, the AOD would be highly tolerant of misalignment while setting it up and tuning to achieve the Bragg angle of incidence in practice.

Figure 5 examines the diffraction efficiency as a function of the incident angle θ_{in} for different acoustic frequencies and $\Delta n = 2.2\times10^{-5}$. This value of Δn is the optimal index modulation strength at the frequency F = 75 MHz. The Bragg diffraction condition is satisfied only at $\theta_{in} = 0.324^{o}$ for the frequency of 75 MHz. The diffraction efficiency is nearly 100% and varies symmetrically in the proximity of this angle, but the curve becomes asymmetric away from this angle because Eqs. (8) and (9) hold good around the Bragg angle of incidence. For the other two RF frequencies of 65 MHz and 85 MHz, the Bragg angles are 0.281° and 0.367°, respectively. Although the Bragg condition is satisfied at these two angles, the diffraction efficiency is not unity at the corresponding frequencies because the efficiency of an AOD depends on both the index modulation strength and the degree to which the momentum is conserved in the photon-phonon

interaction [29,30]. While the frequency of the acoustic wave affects the conservation of momentum for a given incident light, the acoustic amplitude influences Δn. Therefore, both the frequency F, and the amplitude or equivalently Δn, need to be adjusted to optimize the diffraction efficiency.

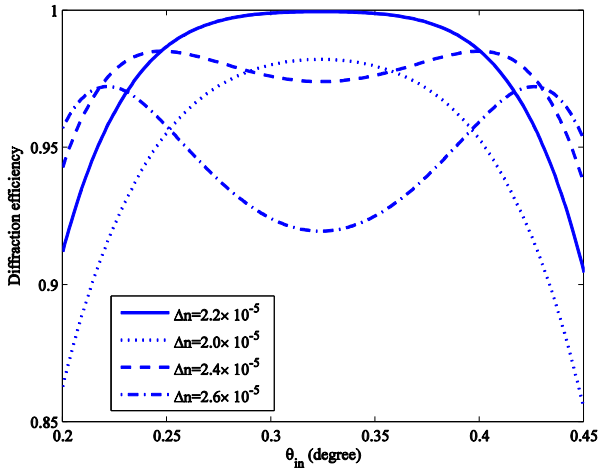

Figure 5-4 Reflectance and Transmittance as a function of the index modulation strength Δn with L = 2.24 cm, Q = 4π and F = 75 MHz at Bragg incidence angle of 0.324o.

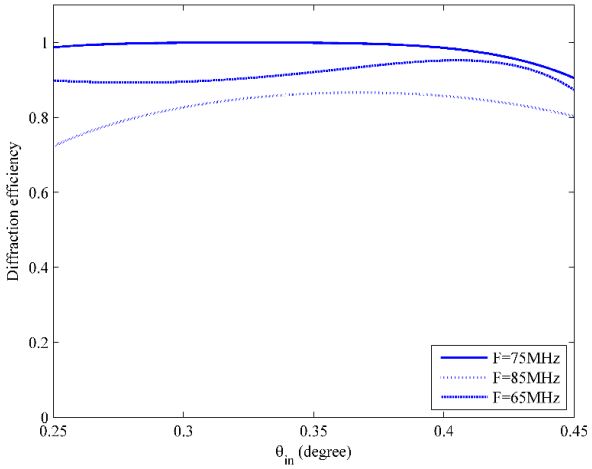

Figure 5-5 Diffraction efficiency as a function of the incident angle θin with Δn = 2.2×10-5, Q = 4π for different RF frequencies.

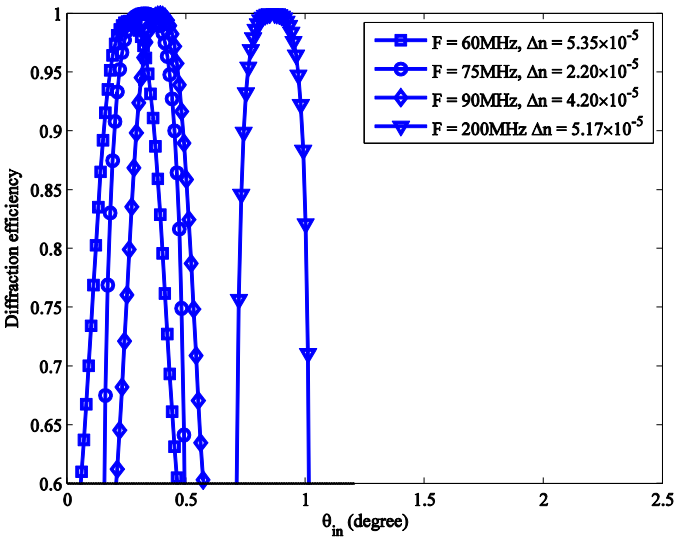

Figure 5-6 Diffraction efficiency as a function of the incident angle θin for Q = 4π.

The effect of the optimal pair of F and Δn is studied in Fig. 6, which shows the performance of dynamic phase gratings, i.e., acoustic lobes at different steering angles. The diffraction efficiency is plotted as a function of the incident angle θ_{in} for different pairs F and Δn, so that each pair has its own Bragg angle of incidence. This is the reason for achieving 100% diffraction efficiency at different frequencies. As discussed earlier in this section, operating the piezoelectric transducers at different phase-shifts forms acoustic lobes in the AOD at various steering angles, resulting in new incident angles $\theta_0 + \tilde{\theta}$. For each new angle of incidence, an acoustic frequency can be selected to ensure that the Bragg diffraction condition is satisfied. Also the transducers can be operated in the amplitude modulation mode so that the acoustic pressure inside the AOD is sufficient to induce an optimal Δn. Thus the phase, frequency and amplitude modulations of the transducers enable achieving 100% diffraction efficiency with relatively large deflection angles at different frequencies.

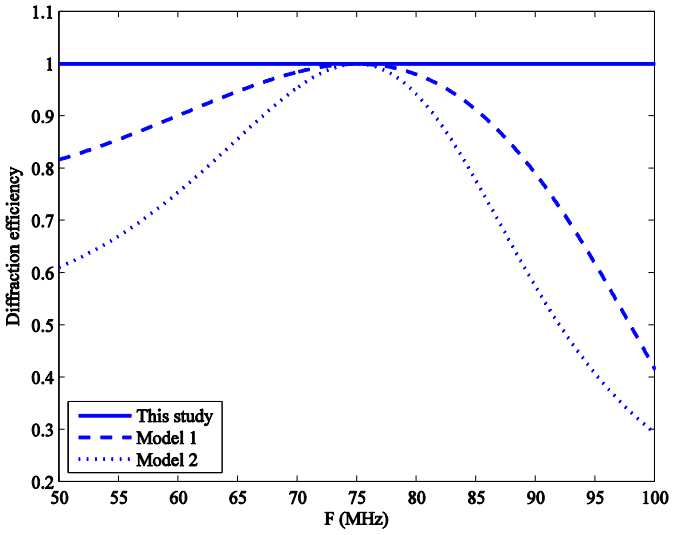

Figure 5-7 Comparison of the diffraction efficiency obtained from different models.

Figure 7 compares the results of this study with two other models to examine the effect of two-dimensional and one-dimensional refractive index modulations on the diffraction efficiency. This study is based on steerable acoustic lobes, whereas models 1 and 2, which were developed by Kong [14], and Uchida and Niizeki [13], respectively, considered conventional AODs composed of a single or multiple transducers. Models 1 and 2 in Fig. 7 show that conventional AODs have the maximum diffraction efficiency only at the Bragg angle corresponding to the central operating frequency of the AOD, which is 75 MHz in this study, and have limited bandwidth as imposed by the Bragg interaction. Only certain momentum components of the acoustic beam, which can be phase-matched to the momentum components of the incident and diffracted lights, are useful for generating the -1 order mode from the 0 order mode. In the acoustic lobe steering model of this study, however, the diffraction efficiency is 100% for all operating frequencies of the AOD because the Bragg diffraction condition can be achieved at all frequencies as discussed previously.

It should be noted that an ideal, i.e., a loss-less acousto-optic device, is considered in this study. In practice, however, the acousto-optic crystals can absorb the light causing a significant amount of power loss, which will reduce the diffraction efficiency. Additionally, the piezoelectric transducers are not ideal, i.e., they do not generate acoustic waves at a single frequency, which can also affect the diffraction of the light. The diffraction efficiency is 100% in loss-less media as predicted by models 1 and 2, and the model of this study. Klein and Cook's [3] model also yielded 100% diffraction efficiency for isotropic media under certain operating conditions. For anisotropic media, Kastelik et al. [2] determined 100% diffraction efficiency theoretically, which compares well with their experimental data, over a fairly wide range of acoustic frequency under the no power loss condition. These results highlight that all of the light can be diffracted into the first-order mode for ideal AODs.

5.4. Conclusion

A two-dimensional refractive index model has been presented to modulate the refractive index in two dimensions for improved performance of AODs. The refractive index varies as periodic and sinc functions in the longitudinal and transverse directions, respectively. This type of modulation can be achieved by operating the piezoelectric transducers of AODs in the phase, frequency and amplitude modulation modes simultaneously. The resulting second order coupled mode equations have been solved analytically for the reflection and transmission coefficients of the AOD. The phased array of transducers allows generating tilted acoustic wavefront dynamically, resulting in acoustic lobe steering that produces dynamic two-dimensional phase grating inside the AOD. Due to this effect, the AOD can be operated under the Bragg diffraction condition at any frequency

with corresponding optimal index modulation strength and consequently, the diffraction efficiency is found to be unity at different frequencies with relatively large deflection angles. Therefore, the performance of AODs under the two-dimensional index modulation is not limited by the frequency bandwidth as observed in conventional AODs.

5.5. References

[1] G. D. Reddy, R. J. Cotton, A. S. Tolias, and P. Saggau, “Random-access multiphoton microscopy for fast three-dimensional imaging,” in *Membrane Potential Imaging in the Nervous System and Heart*, M. Canepari, D. Zecevic, and O. Bernus, ed. (Springer, 2015), Chap. 18.

[2] J.-C. Kastelik, S. Dupont, K. B. Yushkov, and J. Gazalet, "Frequency and angular bandwidth of acousto-optic deflectors with ultrasonic walk-off," Ultrasonics **53**, 219-224 (2013).

[3] W. R. Klein and B. D. Cook, "Unified approach to ultrasonic light diffraction," *IEEE Trans. Sonics and Ultrasonics* **14**, 123-134 (1967).

[4] R. S. Chu and T. Tamir, "Guided-wave theory of light diffraction by acoustic microwaves," IEEE Trans. Microw. Theory Tech. **18**, 486-504 (1970).

[5] H. Kogelnik, "Coupled wave theory for thick hologram gratings," Bell System Technical Journal **48**, 2909-2947 (1969).

[6] F. G. Kaspar, "Diffraction by thick, periodically stratified gratings with complex dielectric constant," J. Opt. Soc. Am. A **63**, 37-45 (1973).

[7] C. B. Burckhardt, "Diffraction of a Plane Wave at a Sinusoidally Stratified Dielectric Grating," J. Opt. Soc. Am. **56**, 1502-1508 (1966).

[8] T. K. Gaylord and M. G. Moharam, "Planar dielectric grating diffraction theories," Appl. Phys. B **28**, 1-14 (1982).

[9] R. S. Chu and T. Tamir, "Bragg diffraction of Gaussian beams by periodically modulated media," J. Opt. Soc. Am. **66**, 220-226 (1976).

[10] R. S. Chu and T. Tamir, "Diffraction of Gaussian beams by periodically modulated media for incidence close to a Bragg angle," J. Opt. Soc. Am. **66**, 1438-1440 (1976).

[11] R. S. Chu, J. A. Kong, and T. Tamir, "Diffraction of Gaussian beams by a periodically modulated layer," J. Opt. Soc. Am. **67**, 1555-1561 (1977).

[12] M. G. Moharam, T. K. Gaylord, and R. Magnusson, "Bragg diffraction of finite beams by thick gratings," J. Opt. Soc. Am. **70**, 300-304 (1980).

[13] N. Uchida and N. Niizeki, "Acoustooptic deflection materials and techniques," Proc. IEEE **61**, 1073-1092 (1973).

[14] J. A. Kong, "Second-order coupled-mode equations for spatially periodic media," J. Opt. Soc. Am. **67**, 825-829 (1977).

[15] J.-M. Andre, K. L. Guen, and P. Jonnard, "Rigorous coupled-wave theory for lossy volume grating in Laue geometry X-ray spectroscopy," submitted to J. Opt. Soc. Am. B (2014) <hal-01082017>, https://hal.archives-ouvertes.fr/hal-01082017.

[16] L. Azar, Y. Shi, and S.-C. Wooh, "Beam focusing behavior of linear phased arrays," NDT & E International **33**, 189-198 (2000).

[17] X. Zhao and T. Gang, "Nonparaxial multi-Gaussian beam models and measurement models for phased array transducers," Ultrasonics **49**, 126-130 (2009).

[18] K. Nakahata and N. Kono, "3-D modelings of an ultrasonic phased array transducer and its radiation properties in solid," in *Ultrasonic Waves*, A. A. dos Santos, Jr., ed. (InTech, Croatia, 2012, ISBN: 978-953-51-0201-4), p. 59-80.

[19] M. Gottlieb, L. M. Ireland, and J. M. Ley, *Electro-Optic and Acousto-Optic Scanning and Deflection* (Marcel Dekker, 1983), pp. 151, 152, 102, 126.

[20] S.-C. Wooh and Y. Shi, "Influence of phased array element size on beam steering behavior," Ultrasonics **36**, 737-749 (1998).

[21] S.-C. Wooh and Y. Shi, "Optimum beam steering of linear phased arrays," Wave Motion **29**, 245-265 (1999).

[22] S.-C. Wooh and Y. Shi, "A simulation Study of the beam steering characteristics for linear phased arrays," JNE **18**, 39-57 (1999).

[23] A. Korpel, *Acousto-Optics* (CRC Press, 1997), p. 49.

[24] B. M. Watrasiewicz, "Some useful integrals of Si(x), Ci(x) and related integrals," Optica Acta **14**, 317-322 (1967).

[25] F. G. Tricomi, *Integral Equations* (Dover, 1985), p. 42.

[26] J. A. Kong, *Electromagnetic Wave Theory, Second Edition,* (Wiley, 1990), p. 119.

[27] J. P. Xu and R. Stroud, *Acousto-Optic Devices: Principles, Design, and Applications* (Wiley, 1982), p. 23.

[28] N. Uchida and Y. Ohmachi, "Elastic and photoelastic properties of TeO_2 single crystal," J. Appl. Phys. **40**, 4692-4695 (1969).

[29] A. P. Goutzoulis and V. V. Kludzin,"Principles of acousto-optics" in *Design and Fabrication of Acousto-Optic Devices*, A. P. Goutzoulis and D. R. Pape, ed. (Marcel Dekker, 1994), p. 13.

[30] D. R. Pape, O. B. Gusev, S. V. Kulakov, and V. V. Momotok, "Design of acousto-optic deflectors" in *Design and Fabrication of Acousto-Optic Devices*, A. P. Goutzoulis and D. R. Pape, ed. (Marcel Dekker, 1994), pp. 73,74-77.

CHAPTER 6: GAUSSIAN BEAM DIFFRACTION BY TWO-DIMENSIONAL REFRACTIVE INDEX MODULATION FOR HIGH DIFFRACTION EFFICIENCY AND LARGE DEFLECTIVE ANGLE

6.1. Introduction

Acousto-Optic Deflectors (AODs) are inertialess optical solid state devices to deflect and scan laser beams in numerous applications including microvia drilling in microelectronic industries for advanced high density packaging. Conventional mirror-based mechanical deflectors are prone to wear and tear, mechanical noise and drift due to moving parts such as rotating mirrors [1,2,3]. AODs are free of these drawbacks since they do not have any moving parts. Additionally, AODs allow higher deflection velocities, better accuracy in the scan angle and lower response time than the mechanical deflectors due to massless photons [1]. Various applications of AODs include optical communication [4-6], optical tweezers for molecule trapping [7], optical image scanners [8.9], and optical frequency shifters [10].

Chu and Tamir [11] modeled the diffraction of Gaussian beams in dielectric media of periodically modulated permittivity by treating the incident beam as linear superposition of plane waves, and showed that both the refracted and Bragg-scattered beams split into two beams and this distortion lowers the diffraction efficiency compared to when a single plane wave is incident on the medium. Later they [12] applied the model to incident angles close to the Bragg angle and analyzed the effect of beam splitting by examining the major and minor lobe profiles for both the refracted and Bragg-scattered beams. Chu, Kong and Tamir [13] and Kong [15] presented a highly accurate second order coupled-mode model for the diffraction of Gaussian beams due to

periodic modulation of permittivity, and showed that the conventional first order coupled-mode theory is accurate for small perturbation in the permittivity and that the second order approach must be used for strongly modulated media. Moharam, Gaylord and Magnusson [14] modeled the diffraction of Gaussian beams in transparent volume gratings by two coupled first order partial differential equations based on a modified version of the two-dimensional coupled wave theory. One-dimensional modulation of the refractive index, n(z), has been considered in the above-mentioned studies. Also conventional AODs operate at small deflection angles, and high diffraction efficiency only over a narrow bandwidth of the acoustic frequency. However, advanced applications, such as high precision and high speed microvia drilling and image scanning, require large deflection angles for large-area processing and high diffraction efficiency over a wide acoustic bandwidth. Phased-array transducers have been incorporated to AODs for improving the deflection angle and bandwidth [18,19,20] by assuming one-dimensional index modulation that holds good for small tilting of the phase grating planes. Two-dimensional index modulation, n(x,z), provides a mechanism to improve the performance of AODs further. Recently, Andre, Guen and Jonnard [16] applied a rigorous coupled-wave theory to lossy volume gratings with two-dimensional permittivity for X-ray spectroscopy and concluded that the rigorous approach without two-wave and first derivative approximations is necessary to accurately calculate the diffraction efficiency. Wang et al. [22] studied the effect of two-dimensional refractive index modulation on the diffraction of plane waves and showed that the deflection angle can be increased using phased array transducers and the diffraction efficiency is nearly unity over a wide acoustic bandwidth. The phase-shifted acoustic waves, which are emitted by the transducers, interfere inside the AOD to form a phase grating within which the refractive index varies in two dimensions. The grating lobe can be tilted to different angles by operating the transducers with appropriate time-delayed

radio-frequency (RF) signals. This tilt in the grating automatically modifies the incident angle of the laser beam on the grating plane even though the laser is stationary [17]. So the frequency of the RF signal is changed to achieve the Bragg condition under this new angle of incidence, and thus the dynamic acousto-optic volume grating can improve the performance of AODs.

In this project, the diffraction of Gaussian beams is studied for AODs of finite size with two-dimensional index modulation. Section 2 provides a summary of the AOD geometry and the index modulation used in this study. The Gaussian beam is represented by the superposition of plane waves and then the electric field is determined at the exit surface of the AOD using the plane wave solution from Ref. [22]. The results and discussion are presented in Section 3 for TeO2 and Ge AODs based on the phase, frequency and amplitude modulations of the transducers for Ne-Ne and CO2 lasers respectively.

6.2. Theoretical background

6.2.1. Two-dimensional refractive index modulation

AODs can be generally classified into two groups depending on whether a single transducer or phased-array transducers are used to operate the AODs. The drawbacks of single-transducer AODs are narrow acoustic bandwidth, small deflection angle and small scan angle. Phased-array transducers are utilized to overcome these shortcomings [6,22]. Phase-shifted acoustic waves, which are emitted by the transducers when they are operated with some time delays with respect to each other, propagate through the AOD medium as a tilted composite wavefront (Fig. 5-1) due to the diffraction and interference of the waves. Due to this acoustic effect, the atomic planes of the AOD medium are tilted as alternating compressed and rarefied layers with index modulation

along the titled planes. The composite wavefront can be steered in different directions by dynamically varying the time delays and, consequently, the index modulation planes can be titled at various angles.

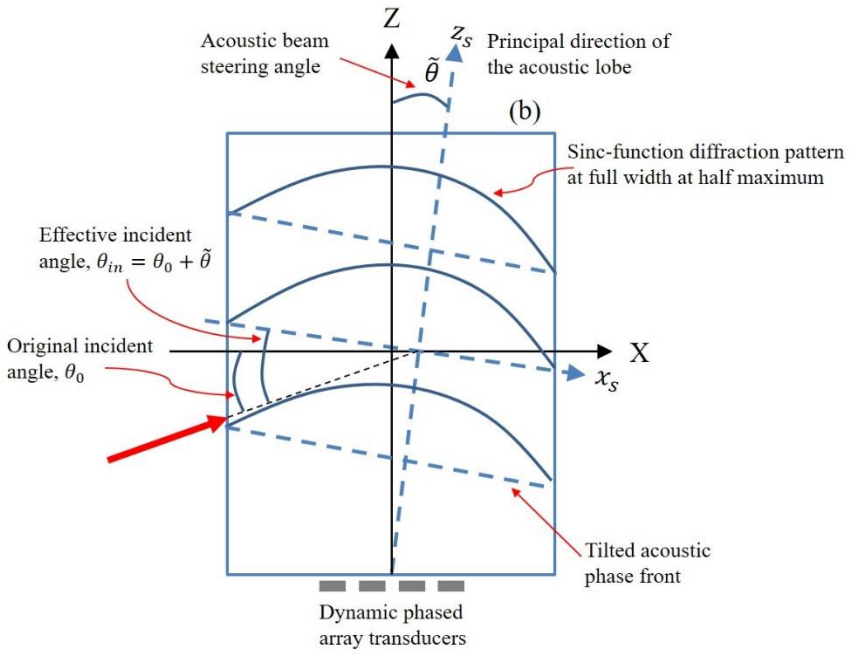

Figure 6-1 The refractive index profiles due to dynamic phased array transducers in this study.

A typical steering angle, $\tilde{\theta}$ corresponding to the principal direction, z_s, of the acoustic diffraction lobe is presented in Fig. 5-1, showing that the new incident angle would be $\theta_{in} = \theta_0 + \tilde{\theta}$ for the tilted index modulation if the laser beam is originally incident on the unperturbed AOD at the angle θ_0. Using this acoustic beam steering mechanism, the angle of laser incidence on the tilted phase grating can be varied automatically without moving the original laser beam. For each steering angle, the frequency of the acoustic waves needs to be adjusted to ensure that θ_{in} in corresponds to the Bragg angle of incidence for achieving large deflection angle given by θ_{in} and large diffraction efficiency given by the Bragg diffraction condition.

The above-mentioned acoustic effect also produces a two-dimensional phase grating in contrast to one-dimensional gratings in conventional AODs. The diffraction pattern of waves emitted by a regular array of emitters generally has the sinc-function shape in Cartesian coordinates. Since the variation of refractive index depends on the intensity distribution of the composite acoustic wavefront, the refractive index is considered to vary as a sinc-function in the transverse direction xs in this study (Fig. 5-2). On the other hand, the refractive index varies periodically with the period Λ. In the longitudinal direction z_s, however, the index varies periodically with the period Λ, where Λ is the wavelength of the acoustic waves in the AOD medium. So the two-dimensional index profile in region II, $n_{II}(x,z)$, can be written as:

$$n_{II} = n_2(\lambda_0) + \Delta n cos\left(\frac{2\pi}{\Lambda} z\right)\left(\frac{sinbx}{bx}\right) \tag{1}$$

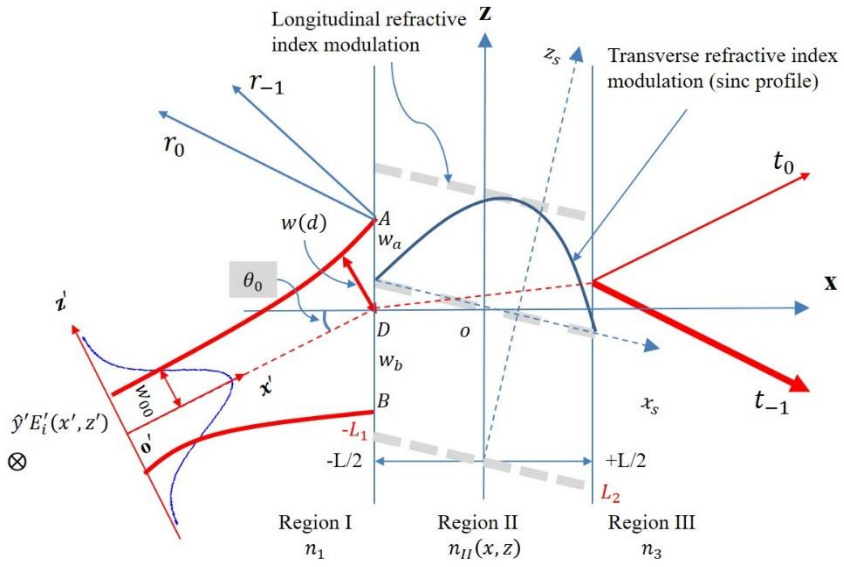

Figure 6-2 Transverse refractive index (sinc profile) generated by a tilted lobe in an acousto-optic medium.

where $n_2(\lambda_0)$ is the refractive index of the unperturbed acousto-optic medium at the wavelength of the incident light in vacuum, λ_0, and Δn is the maximum change in the refractive index. The parameter b is a constant that defines the width of the central lobe of the sinc function. Since this function varies from a maximum value at the center of the lobe to zero at the edge of the lobe, the parameter b is so chosen that the index modulation is significant in the AOD medium. The central peak of the sinc function occurs at $x_s = 0$ and the lobe spans from $x_s = -L_1$ to $x_s = L_2$ (Fig. 5-2) to yield a significant index modulation. If L_m represents the larger of the two values L_1 and L_2, b can be determined by considering that L_m is the full width at half maximum of the sinc function, i.e.,

$$\frac{sin(bL_m/2)}{bL_m/2} = \frac{1}{2} \tag{2}$$

Wang et al. [22] analyzed the performance of AODs using the coupled mode theory for incident lights of plane wavefront and the above-mentioned two-dimensional index modulation. Their model is implemented in this study for analyzing the diffraction of Gaussian beams by decomposing the beam into numerous plane waves.

6.2.2. Decomposition of Gaussian laser beam profiles into plane wave spectral components

The electric field of Gaussian laser beams can be written as follows [38]

$$E_i(x', z') = A_0 \frac{w_{00}}{\omega(x\prime)} e^{-\left(\frac{z\prime}{\omega(x\prime)}\right)^2} e^{ik_0 x\prime} e^{-i\phi(x\prime)} e^{ik_0 \frac{z\prime^2}{2R(x\prime)}} \tag{3}$$

in the Cartesian coordinate system (x', z') with the origin being at the center of the beam waist as shown in Fig. 5-2. Here A_0 is the peak electric field and w_{00} is the radius of the Gaussian beam waist which is located at the plane x' = 0. The radius of the Gaussian beam at any other plane is given by $\omega(x') = w_{00}\sqrt{1 + (x'/x'_R)^2}$, $\phi(x')$ is the Gouy phase, $\phi(x') = arctan(x'/x'_R)$, x'_R is the radius of curvature of the Gaussian laser wavefront, $x'_R = \pi w_{00}^2/\lambda_0$.

The laser beam is incident on the x = -L/2 surface of the AOD with the interception points A, D and B as shown in Fig. 5-2. The widths of the interception DA and DB are given by wa and wb respectively. These two widths are determined by applying the Gaussian beam radius w(x') to the points A and B, which yield wb and wa that can be expressed as:

$$w_a = \frac{-2d_1 sin\theta_0 - \sqrt{(2d_1 sin\theta_0)^2 - 4\left(sin\theta_0{}^2 - \frac{cos\theta_0{}^2}{w_{00}{}^2}x_R{}^2\right)(x_R{}^2 - d_1{}^2)}}{2\left(sin\theta_0{}^2 - \frac{cos\theta_0{}^2}{w_{00}{}^2}x_R{}^2\right)} \tag{4}$$

$$w_b = \frac{2d_1 sin\theta_0 - \sqrt{(2d_1 sin\theta_0)^2 - 4\left(sin\theta_0{}^2 - \frac{cos\theta_0{}^2}{w_{00}{}^2}x_R{}^2\right)(x_R{}^2 - d_1{}^2)}}{2\left(sin\theta_0{}^2 - \frac{cos\theta_0{}^2}{w_{00}{}^2}x_R{}^2\right)} \tag{5}$$

To analyze the laser beam propagation inside the AOD medium in the (x,z) coordinate system, where the consecutive three transformations are involved with: twice translation shifts are characterized by d_1 and $L/2$; once rotation matrix is characterized by the incidence angle of θ_0. The final resultant coordinate transformation Eq. (6) is applied to Eq. (3),

$$\begin{pmatrix} x' \\ z' \end{pmatrix} = \begin{pmatrix} (x + L/2).cos\theta_0 + z.sin\theta_0 + d_1 \\ -\left(x + \frac{L}{2}\right).sin\theta_0 + z.cos\theta_0 \end{pmatrix} \quad (6)$$

to obtain the Gaussian beam profile as

$$E_i(x,z) = A(d_1)e^{-\left[\frac{-(x+L/2)sin\theta_0 + zcos\theta_0}{\omega(d_1)}\right]^2} e^{ik_0\frac{[-(x+L/2)sin\theta_0 + zcos\theta_0]^2}{2R(d_1)}} e^{ik_0[(x+L/2)cos\theta_0 + zsin\theta_0]} \quad (7)$$

where $A(d_1) = A_0 \frac{\omega_0}{\omega(d_1)} e^{ik_0 d_1} e^{-i\phi(d_1)}$ and θ_0 is the incident angle of the Gaussian beam. Eq. (3) is expressed as a superposition of plane waves so that the solution of Ref. [21], which was obtained for the diffraction of plane waves due to two-dimensional index modulation, can be implemented in this study.

6.2.3. Gaussian beam diffraction in AOD media with two-dimensional refractive index modulation

Fourier representation of Ei(x,z) in terms of angular spectra provides a convenient way of expressing the electric field of an incident Gaussian beam as linear plane wave superposition, i.e.,

$$E_i(x,z) = \int_{-\infty}^{\infty} G(k_{0z}) exp[i(k_{1x}x + k_{0z}z)]\, dk_{0z} \quad (8)$$

where $G(k_{0z})$ is the spectral amplitude and exp(i$k_{1x}x$) and exp(i$k_{0z}z$) are spectral components of wavenumbers k_{1x} and k_{0z} for the plane waves propagating in the x and y directions,

respectively. $E_i(x,z)$ is incident on the incident surface of the AOD medium from region I (x<- L/2) with the wavenumber $k_1 = n_1 k_0$, where n_1 is the refractive index of medium I, $k_0 = 2\pi/\lambda_0$ and λ_0 is the wavelength of the incident laser in vacuum. So k_1, k_{1x} and k_{0z} can be related to each other by the expressions $k_{1x} = k_1\cos\theta$, $k_{0z} = k_1\sin\theta$ and $k_{1x} = \sqrt{k_1^2 - k_{0z}^2}$, where θ is the incident angle of an arbitrary plane wave of wavenumber k_1.

The unknown factor, i.e., the spectral amplitude G(k0z), in Eq. (7) can be obtained by applying the Fourier inverse transform to Eq. (7) on the incident surface x = - L/2, which yields

$$G(k_{0z}) = \frac{1}{2\pi}\int_{-\infty}^{\infty} E_i(-L/2\,, z)e^{ik_{1x}L/2}e^{-ik_{0z}z}dz \tag{9}$$

$$E_{inc}(-L/2, z) = A_0 e^{-\left(\frac{z}{\omega_0}\right)^2} e^{ik_0 sin\theta_0 z} \tag{10}$$

Substituting Eq. (10) into Eq. (9), $G(k_{0z})$ is obtained as

$$G(k_{0z}) = \frac{A_0}{\sqrt{\pi}}\left(\frac{\omega_s}{2}\right) e^{-(k_{0z}-k_0 sin\theta_0)^2\left(\frac{\omega_s}{2}\right)^2} e^{ik_{1x}L/2} \tag{11}$$

As pointed out by Chu, Kong and Tamir [23], the transmitted beams in region III can be viewed as the linear superposition of plane wave solutions. Therefore, the electric field of the zeroth order beam in region III is

$$E_0(x,z) = \int_{-\infty}^{\infty} G(k_{0z})t_0(k_{0z})exp\left(ik_{3,0x}x + ik_{0z}z\right)dk_{0z}, \quad for\ x \geq L/2 \tag{12}$$

and the Bragg-diffracted, i.e., -1 order, beam is

$$E_{-1}(x,z) = \int_{-\infty}^{\infty} G(k_{0z}) t_{-1}(k_{0z}) exp\left(ik_{3,-1x}x + ik_{-1z}z\right) dk_{0z}, \quad for\ x \geq L/2 \qquad (13)$$

where $t_0(k_{0z})$ and $t_{-1}(k_{0z})$ are the transmission coefficients for plane waves of wavenumber k_{0z} in the zeroth order and -1 order lights, respectively, at the exit surface x = L/2. Due to the propagation of acoustic waves of wavenumber K in the AOD medium, k_{0z} and k_{-1z} in Eqs. (12) and (13) are the z components of the zeroth and -1 order Floquet modes and are given by $k_{0z} = k_0 sin\theta$ and $k_{-1z} = k_{0z} - K$. Similarly, $k_{3,0x}$ and $k_{3,-1x}$ are the x components of the 0^{th}-order and -1^{st}-order Floquet modes and are given by $k_{3,0x} = \sqrt{k_3^2 - k_{0z}^2}$ and $k_{3,-1x} = \sqrt{k_3^2 - k_{-1z}^2}$. Here $K = 2\pi/\Lambda$ and $k_3 = n_3 k_0$ where the wavelength of the acoustic waves in region II and the refractive index in region III are Λ and n_3, respectively. The transmission coefficients $t_0(k_{0z})$ and $t_{-1}(k_{0z})$ are determined from the solutions of two second-order coupled mode equations for each plane wave spectral component k_{0z} [41].

The integrations in Eqs. (12) and (13) are evaluated numerically using the extended trapezoidal rule [23]. To transform the limits of integration from the infinite range to a finite range, the limits on k_{0z} are considered as follows:

$$k_1 sin\theta_0 - p\frac{2\pi}{w_a + w_b} \leq k_{0z} \leq k_1 sin\theta_0 + p\frac{2\pi}{w_a + w_b} \qquad (14)$$

where p is any positive number which is chosen to ensure that sufficient number of spectral components are selected for representing the Gaussian beam in terms of plane waves. Ngoc and Mayer [24] chose p = 1 for their studies on the intensity distribution of ultrasonic beams reflected

from a liquid-solid interface. In the present study, p is found to be 5 to accurately represent the incident Gaussian laser beam as linear superposition of plane waves. The finite range of integration is discretized into M points with the interval $\Delta k_{0z} = \frac{4p\pi}{(w_a+w_b)(M-1)}$ and the value of the spectral component at any point m as $k_{0z,m} = k_{0z,1} + (m-1)\Delta k_{0z}$ for m = 1, 2,3, …, M where $k_{0z,1} = k_1 sin\theta_0 - p\frac{2\pi}{w_a+w_b}$. Defining the integrands of Eqs. (12) and (13) at any point m as

$$E_{0,m} = \left[G(k_{0z})t_0(k_{0z})exp\left(ik_{3,0x}x + ik_{0z}z\right)\right]_{k_{0z}=k_{0z,m}} \tag{15}$$

$$E_{-1,m} = \left[G(k_{0z})t_{-1}(k_{0z})exp\left(ik_{3,-1x}x + ik_{-1z}z\right)\right]_{k_{0z}=k_{0z,m}} \tag{16}$$

the electric fields in the zeroth and -1st-order modes can be approximately determined by the following expressions:

$$E_0(x,z) \approx \Delta k_{0z} \sum_{m=1}^{M} E_{0,m} - \frac{\Delta k_{0z}}{2}\left(E_{0,1} + E_{0,M}\right) \tag{17}$$

$$E_{-1}(x,z) \approx \Delta k_{0z} \sum_{m=1}^{M} E_{-1,m} - \frac{\Delta k_{0z}}{2}\left(E_{-1,1} + E_{-1,M}\right) \tag{18}$$

Eqs. (17) and (18) are used to analyze the performance of AODs for He-Ne and CO_2 lasers of wavelengths 632.8 nm 10.6 μm, respectively, and the corresponding AOD media are considered to be crystalline TeO_2 and Ge.

6.3. Results and discussion

To examine the transmitted behavior of the Gaussian beam diffracted by periodically modulated AO medium, several numerical calculations were carried out in this study. The incident Gaussian beam is from HeNe laser source with λ_0 = 632.8 nm in the air and beam width ϕ = 0.6366 mm. The acousto-optic medium is called Tellurium dioxide, TeO2 crystal with the refractive index of n_2 = 2.26 at HeNe wavelength, which is transparent in the range of 0.35 to 5 μm [16,8]. We chose symmetric configuration in region I and II, $n_1 = n_3 = 1.0$.

Table 3 Simulation parameters for TeO2 crystal at HeNe-laser and Ge crystal at CO_2-laser.

Laser wavelength	10.6 μm at CO_2	632.8 nm at HeNe
AO material	Ge crystal	TeO_2 crystal
Refractive index, n	4.0042	2.26
Sound speed at P-wave	5500 m/s	4200 m/s
Sound speed at S-wave	3510 m/s	616 m/s
Density of AO medium, ρ	5.327 g/cm^3	5.99 g/cm^3
Central acoustic frequency	70 MHz	75 MHz
Central acoustic wavelength,	78.6 μm	56 μm
Acoustic bandwidth	40 MHz	32 MHz
Figure of merit, M_2	150×10^{-15} s^3/kg	793×10^{-15} s^3/kg
Attenuation constant, Γ	30 dB/cm-GHz^2	15 dB/cm-GHz^2

The accuracy of $E_0(x,z)$ and $E_{-1}(x,z)$ in Eqs. (23) and (24) depends on the choice of p and M. While p determines the range of spectral components chosen for plane wave decomposition of the Gaussian beam, M affects the convergence of the numerical integration by the extended trapezoidal rule. To verify the computational accuracy, the normalized intensity of the Gaussian beam is calculated by two approaches that are based on the exact expression of the input beam given by Eq. (6) and the spectral representation of the beam given by Eqs. (7) and (9). The results as obtained at the incident surface of the AOD medium with the beam waist on this surface, i.e., x = -L/2 and $d_1 = 0$, as shown in Fig. 5-3 for the case of TeO_2 AOD. The two results were found to match well when p = 5 and M = 100, and p = 5 and M = 100 for TeO_2 and Ge AODs respectively.

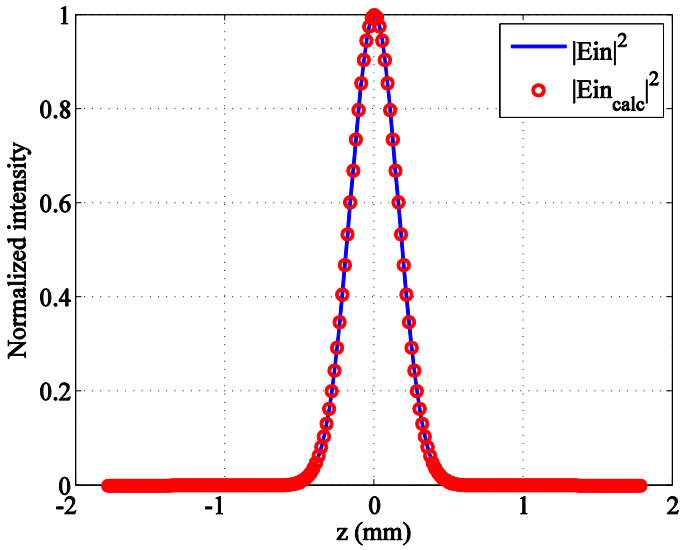

Figure 6-3 Exact Gaussian beam when you use Eq. (6), and Plane wave superposition.

The results of this study are also compared to the beam profiles determined by Chu, Kong and Tamir [13] for one-dimensional index modulation, and their model is referred to as 1D-CKT model hereafter. For this comparison, the sinc function is set to unity in Eq. (1) and the laser beam profiles obtained at the exit surface (x = L/2) using Eqs. (17) and (18) are presented in Fig. 5-4. Although the profiles of both studies exhibit similar trend, the results do not match exactly and this discrepancy may be attributed to the method of solution. The transmission coefficients t_0 and t_{-1} in 1D-CKT model were based on Kong's [15] exact calculation for these two coefficients by solving an 8×8 matrix equation exactly. In the present study, the transmission coefficients were calculated by considering Wang's et al. [22] first order approximation of the electric field for each plane wave component of the Gaussian beam. The results, however, exhibit two dominant peaks in the -1 order diffracted beam showing non-Gaussian profiles and splitting of the beam. The

zeroth order beam is also non-Gaussian with a fairly uniform irradiance profile showing distortion of the original Gaussian beam incident on the AOD.

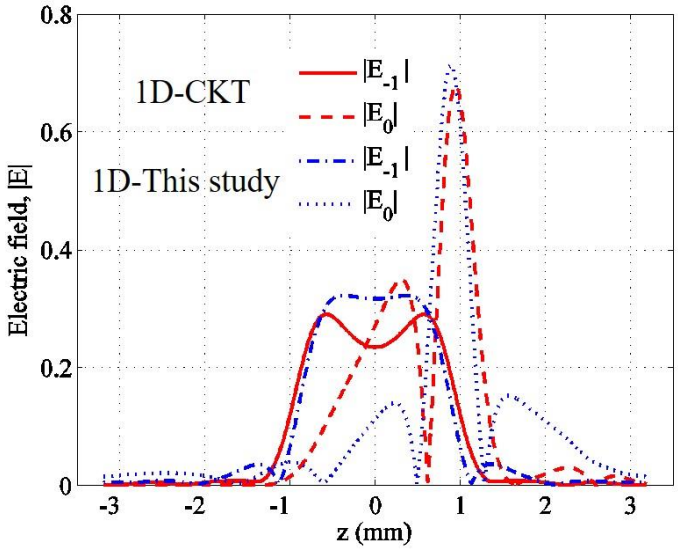

Figure 6-4 Comparison of the Gaussian beam profiles at the exit surface of a TeO_2 AOD for one-dimensional index modulation.

To examine the beam splitting and distortion, two-dimensional index modulation of this study, which is referred to as 2D model hereafter, is analyzed with optimized index modulation strength Δn as presented in Fig. 5-5.

Results are obtained from both the 2D and 1D-CKT models for the optimized values of $\Delta n = 2.2\times10^{-5}$ and 1.4×10^{-5}, respectively, to achieve the maximum diffraction efficiency in each model. Both models yield Gaussian profile with beam splitting in the -1 order diffracted beam. The zeroth order beam, however, exhibits non-Gaussian profile with two peaks indicating beam splitting at the exit surface x = L/2. The beam splitting is less dominant with much lower electric field in the 2D model than in the case of 1D-CKT model. Two-dimensional index modulation,

therefore, allows more energy transfer to the -1 order beam than the one-dimensional index modulation and, consequently, higher diffraction efficiency can be achieved in the former case.

Figure 5-6 examines the shape of the zeroth order split beam as it propagates in medium III away from the exit surface of the AOD medium. At x = 3L/2, the zeroth order beam begins to separate from the -1 order beam, but the zeroth order beam profile remains the same as at x = L/2 in Fig. 5-5.

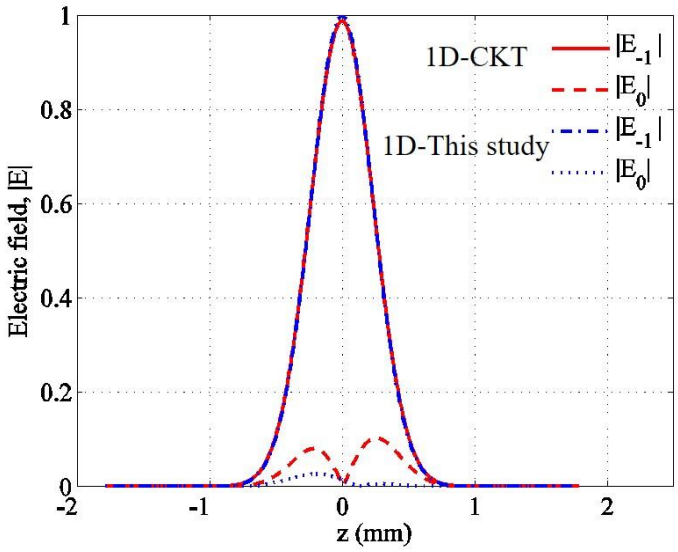

Figure 6-5 Near-field Electric field (|E|) at exit boundary x = L/2 calculated from GBD-model (blue solid line for -1st ; blue dashed line for 0th) and CKT-model (red dotted line for -1st ; red dash-dot line for 0th) with F = 75MHz, L = 2.24 cm, θ_{in} = 0.324°.

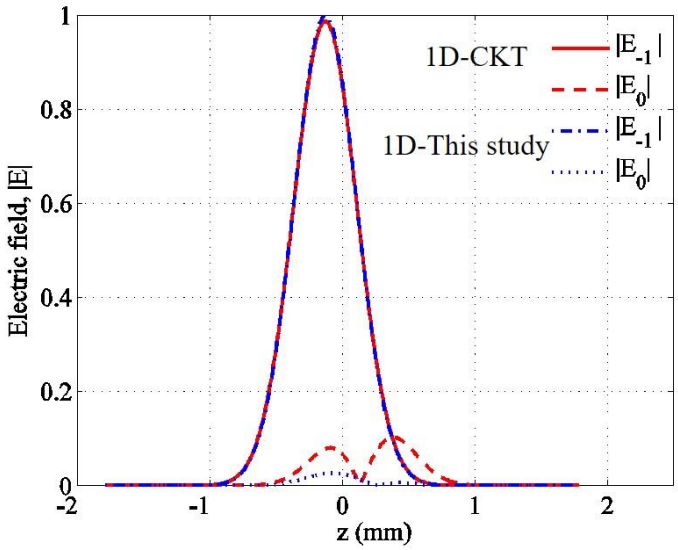

Figure 6-6 Near-field Electric field (|E|) at x = 3L/2 calculated from GBD-model (blue solid line for -1st ; blue dashed line for 0th) and CKT-model (red dotted line for -1st ; red dash-dot line for 0th) with F = 75MHz, L = 2.24 cm, θ_{in} = 0.324°.

Wang et al. [22] showed that nearly 100% diffraction efficiency can be achieved for a given acoustic beam steering angle, $\tilde{\theta}$ (Fig. 5-1), by optimizing the acoustic frequency F and the index modulation strength Δn. The steering of acoustic beam produces tilted phase grating inside the AOD device, and the tilt angle automatically modifies the laser incident angle on the grating compared to the original angle of incidence (θ_0) on the AOD device, resulting in a new incident angle $\theta_{in} = \theta_o + \tilde{\theta}$. So the acoustic frequency and amplitude are modulated to achieve the Bragg diffraction under the new angle of incidence and maximize the diffraction efficiency, respectively. The diffraction efficiency is plotted as a function of the incident angle θ_{in} for different pairs of F and Δn in Fig. 5-7 for He-Ne lasers, so that each pair has its own Bragg angle of incidence and thus nearly 100% diffraction efficiency is achieved at different values of F. A change in F changes the wavelength, Λ, of the acoustic waves inside the AOD medium and, therefore, the periodicity

of the phase grating changes as F is varied. Since the diffraction angle and efficiency depend on the ratio $n_2\lambda_0/\Lambda$, the effect of laser wavelength is examined in Fig. 5-8 for CO_2 lasers of wavelength 10.6 μm using Ge as the AOD medium. Both Figs. 5-7 and 5-8 show that the phased array AODs increase the efficiency and deflection angle. Also the acoustic bandwidth of the AODs increases since nearly 100% diffraction efficiency is achieved over a wide range of acoustic frequency.

In Figs. 5-7 and 5-8, the acoustic lobes were generated at different steering angles $\tilde{\theta}$ by considering the pitch, i.e., the center-to-center distance between two adjacent transducers, as $\Lambda/2$ for each F. Nakahata et al. [17] reported that optimum lobes are produced when the pitch is $\Lambda/2$. Since the acoustic lobes affect the shape of the phase grating and Λ depends on F, the pitch was varied for different frequencies to obtain the ideal values of the diffraction efficiency and deflection angle under the ideal pitch condition in these two figures. In practice, however, the pitch cannot be varied once the AOD is fabricated with a certain pitch for a given F and, therefore, the diffraction efficiency and deflection angle will deviate from their ideal values. This deviation is studied by determining the real values of the diffraction efficiency and deflection angle for the pitch $\Lambda_m/2$. Here Λ_m is the minimum acoustic wavelength corresponding to the maximum frequency considered in this study for the TeO_2 and Ge AODs. The values of Λ_m are 21 μm and 27.5 μm for the frequency of 200 MHz, based on TeO_2 and Ge respectively. Under this pitch condition, the real values of the diffraction efficiency and deflection angle are compared to their ideal values in Figs. 5-9 and 5-10 for the TeO_2 and Ge AODs. Although the real values differ from the ideal values, the maximum deviations of the diffraction efficiency are, respectively, within 32% of the ideal values for the TeO_2 AOD and 72% of the ideal values for the Ge AOD; while the deflectiona angle has no deivaiton for both cases.

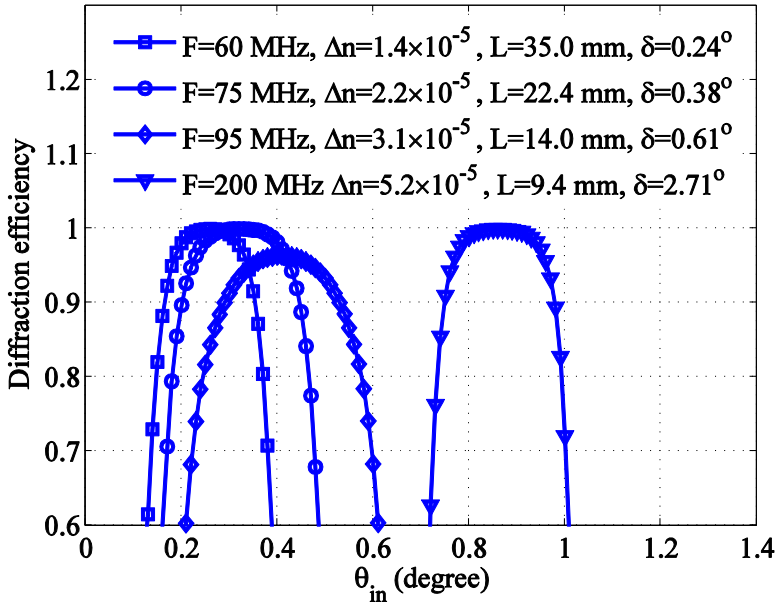

Figure 6-7 Diffraction efficiency as a function of the incident angle θ_{in} with different combination pairs of RF frequency F and index modulation Δn for $Q \geq 4\pi$ based on Ge crystal.

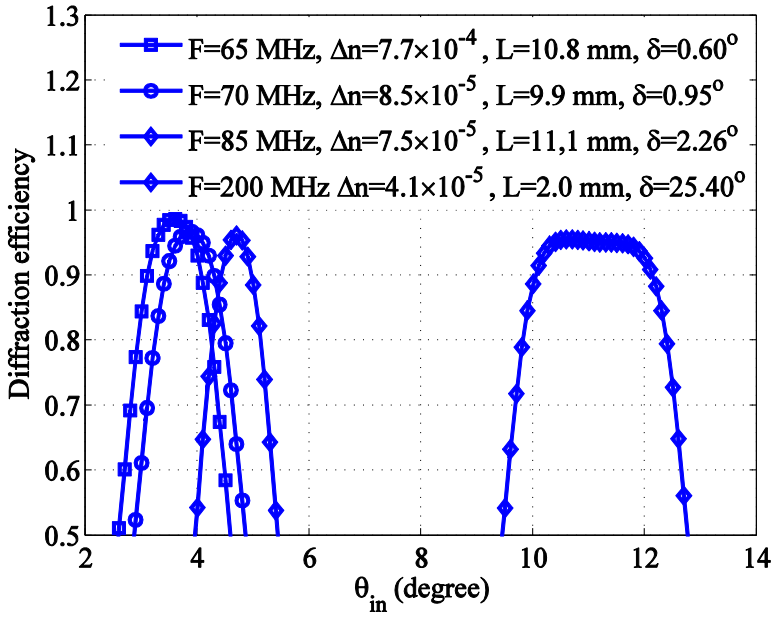

Figure 6-8 Diffraction efficiency as a function of the incident angle θin with different combination pairs of RF frequency F and index modulation Δn for $Q \geq 4\pi$ based on Ge crystal.

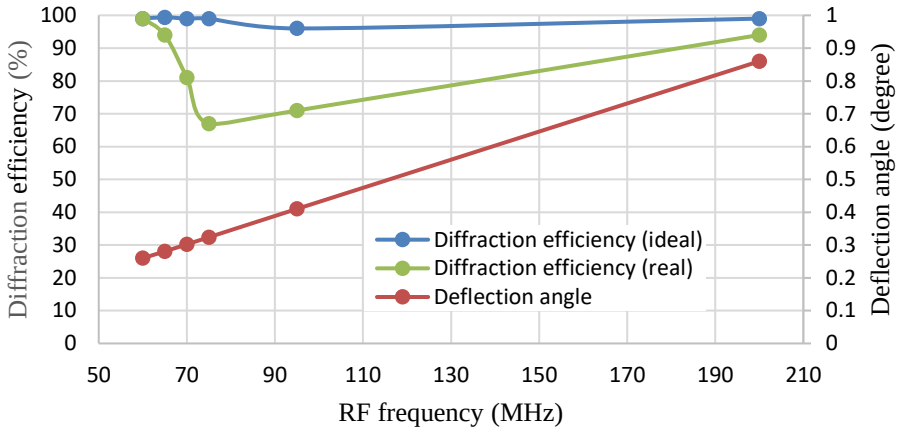

Figure 6-9 Comparison between ideal and real values of the diffraction efficiency and deflection angle for He-Ne lasers and a phased array TeO2 AOD with pitch S=10.5μm .

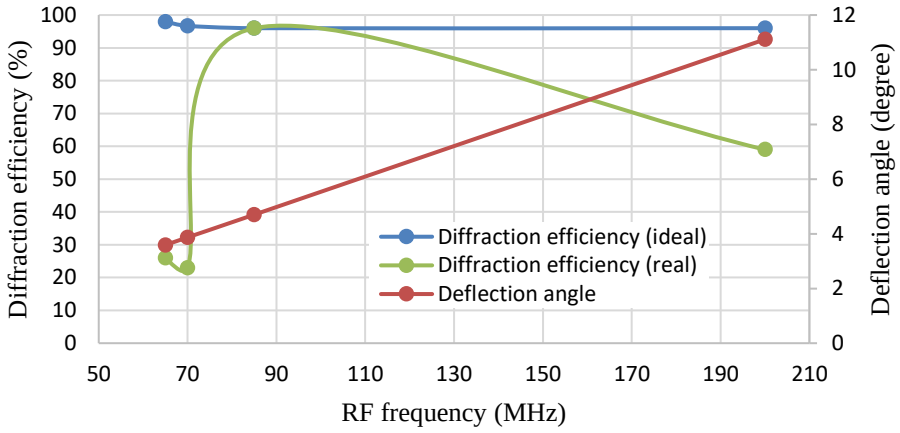

Figure 6-10 Comparison between ideal and real values of the diffraction efficiency and deflection angle for CO2 lasers and a phased array Ge AOD with pitch S=13.75μm .

Table 4 Ideal AO performance characterization and TeO2-AOD dimensions based on numerical simulation.

F (MHz)	60	65	70	75	95	200
η (%)	99	99	99	99	96	99
θ_D (in air)	0.26º	0.28º	0.30º	0.32º	0.41º	0.86º
Δ n ($\times 10^{-5}$)	1.4	1.9	2.0	2.2	3.1	5.2
Λ (μm)	70.0	60.0	64.6	56.0	46.7	21.0
L (mm)	35.0	25.7	29.8	22.4	14.0	9.4
# of elements at pitch=10.5μm	3334	2448	2838	2134	1334	896
$\tilde{\theta}$ at θ_0=0.00º	0.26º	0.28º	0.30º	0.32º	0.41º	0.86º
Time delay (ps)	11.3	12.2	13.1	14.1	17.9	37.7
Element dimension (μm)	Pitch: S = 10.5 μm Width: W = 7.79 μm Height: H = 2.74 mm					

Table 5 Real AO performance characterization and TeO2-AOD dimensions based on numerical simulation.

F (MHz)	60	65	70	75	95	200
η (%)	99	94	81	67	71	94
η-deviation (%)	0	5.1	18.2	32.3	26.0	5.1
θ_D (in air)	0.26º	0.28º	0.30º	0.32º	0.41º	0.86º
Δn ($\times 10^{-5}$)	1.4	1.4	1.4	1.4	1.4	1.4
Λ (μm)	70.0	60.0	64.6	56.0	46.7	21.0
L (mm)	35.0	35.0	35.0	35.0	35.0	35.0
# of elements at pitch=10.5μm	3334	3334	3334	3334	3334	3334
$\tilde{\theta}$ at θ_0=0.00º	0.26º	0.28º	0.30º	0.32º	0.41º	0.86º
Time delay (ps)	11.3	12.2	13.1	14.1	17.9	37.7
Element dimension	Pitch: S=10.5 μm Width: W=7.79 μm Height: H=2.74 mm					

Table 6 Ideal AO performance characterization and Ge-AOD dimensions based on numerical simulation.

F (MHz)	65	70	85	200
η (%)	98	97	96	96
θ_D (in air)	3.59º	3.87º	4.70º	11.11º
Δ n ($\times 10^{-4}$)	7.7	8.5	7.5	4.1
Λ (μm)	84.6	78.6	65.0	27.5
L (mm)	10.8	9.9	11.1	2.0
# of elements at pitch=13.75μm	786	720	808	146
$\tilde{\theta}$ at θ_0=3.00º	0.59º	0.87º	1.70º	8.11º
Time delay (ps)	26	38	74	353
Element dimension	Pitch: S=13.75 μm Width: W=10.2 μm Height: H=2.74 mm			

Table 7 Real AO performance characterization and Ge-AOD dimensions based on numerical simulation.

F (MHz)	65	70	85	200
η (%)	26	23	96	59
η-deviation (%)	73.5	76.3	0	38.5
θ_D (in air)	3.59º	3.87º	4.70º	11.11º
Δn ($\times 10^{-4}$)	3.4	3.3	7.5	7.8
Λ (μm)	84.6	78.6	65.0	27.5
L (mm)	11.1	11.1	11.1	11.1
# of elements at pitch=13.75μm	808	808	808	808
$\tilde{\theta}$ at θ_0=3.00º	0.59º	0.87º	1.70º	8.11º
Time delay (ps)	26	38	74	353
Element dimension	Pitch: S=13.75 μm Width: W=10.2 μm Height: H=2.74 mm			

6.4. Conclusions

The performance of two phased array AODs is analyzed for Gaussian laser beams of wavelengths 632.8 nm and 10.6 μm by considering two-dimensional refractive index modulation. Nearly 100% diffraction efficiency is achieved without any beam splitting or distortion in the -1 order beam for

both two-dimensional and one-dimensional index modulations. The zeroth order beam, however, exhibits less distortion and less electric field in the case of former modulation than the latter. Two-dimensional modulation, therefore, yields slightly higher diffraction efficiency than the one-dimensional modulation. The profile of the distorted beam appears to be non-Gaussian and this profile does not change as the beam propagates outside the AOD medium. The phased array AODs can be operated with nearly 100% diffraction efficiency over a broad range of acoustic frequency and thus the bandwidth of the device increases. Also the acoustic beam steering capability provides a mechanism to create titled phase gratings and this tilt angle is utilized to achieve large deflection angles for the diffracted laser beam. The performance of phased array AODs depends on the pitch of the piezoelectric transducers. Although the ideal pitch condition cannot be achieved in practice, AODs with non-ideal pitch condition are found to perform well with very little deviation from the ideal performance.

6.5. References

[1] G. R. B. E. Romer and P. Bechtold, “Electro-optic and acousto-optic laser beam scanners,” Physics Procedia 56 29 – 39 (2014).

[2] G. J. Evans, P.A. Kirkby, K. M. N. S. Nadella, B. Marin and R. A. Silver, “Development and application of a ray-based model of light propagation through a spherical acousto-optic lens,” Optics Express 23(18) 23493-23510 (2015).

[3] J. Heberle, P. Bechtold, J. Strauß and M. Schmidt, “Electro-optic and acousto-optic laser beam scanners,” Laser-based Micro- and Nanoprocessing X, edited by Udo Klotzbach, Kunihiko Washio, Craig B. Arnold, Proc. of SPIE 9736, 97360L-1:10 (2016).

[4] N.J. Berg and J.M. Pellegrino, Acousto-Optic Signal Processing (Marcel Dekker, 1995), pp. 47-80.

[5] G. Aubin, J. Sapriel, V.Ya. Molchanov, R. Gabet, P. Grosso and S. Gosselin, Y. Jaouen, “Multichannel acousto-optic cells for fast optical crossconnect,” Electron. Lett. 40, 448–449 (2004).

[6] S.N. Antonov and Yu.G. Rezvov, “Efficient multi-beam Bragg acoustooptic diffraction with phase optimization of a multifrequency acoustic wave,” Tech. Phys. 52, 1053–1060 (2007).

[7] A.H. Mack, M.K. Trías and S.G.J. Mochrie, “Precision optical trapping via a programmable direct-digital-synthesis-based controller for acousto-optic deflectors,” Rev. Sci. Instrum. 80, 016101-1:3 (2009).

[8] Y. Kremer, J.-F. Léger, R. Lapole, N. Honnorat, Y. Candela, S. Dieudonné and L. Bourdieu, “A spatio-temporally compensated acousto-optic scanner for twophoton microscopy providing large field of view,” Opt. Exp. 16, 10066–10076 (2008).

[9] P.A. Kirkby, K.M.N. Srinivas Nadella and R.A. Silver, “A compact acousto-optic lens for 2D and 3D femtosecond based 2-photon microscopy,” Opt. Exp. 18, 13720–13744 (2010).

[10] M.G. Gazalet, M. Ravez, F. Haine, C. Bruneel and E. Bridoux, “Acousto-optic lowfrequency shifter,” Appl. Opt. 33, 1293–1298 (1994).

[11] C. Grebing, S. Koke and G. Steinmeyer, “Self-referencing of optical frequency combs, In: Conference on Lasers and Electro-Optics/International Quantum Electronics Conference,” OSA Technical Digest, Optical Society of America, CTuK5 (2009).

[12] R. S. Chu and T. Tamir, “Diffraction of Gaussian beams by periodically modulated media for incidence close to a Bragg angle,” J. Opt. Soc. Am. 66(12), 1438–1440 (1976).

[13] R. S. Chu, J. A. Kong, and T. Tamir, “Diffraction of Gaussian beams by a periodically modulated layer,” J. Opt. Soc. Am. 67(11), 1555–1561 (1977).

[14] M. G. Moharam, T. K. Gaylord, and R. Magnusson, “Bragg diffraction of finite beams by thick gratings,” J. Opt. Soc. Am. 70(3), 300–304 (1980).

[15] J. A. Kong, "Second-order coupled-mode equations for spatially periodic media," J. Opt. Soc. Am. 67, 825-829 (1977).

[16] J.-M. Andre, K. L. Guen, and P. Jonnard, "Rigorous coupled-wave theory for lossy volume grating in Laue geometry X-ray spectroscopy," submitted to J. Opt. Soc. Am. B (2014) <hal-01082017>, https://hal.archives-ouvertes.fr/hal-01082017.

[17] K. Nakahata and N. Kono, “3-D modelings of an ultrasonic phased array transducer and its radiation properties in solid,” in Ultrasonic Waves, A. A. dos Santos, Jr., ed. (InTech, Croatia, 2012, ISBN: 978-953-51-0201-4), p. 59-80.

[18] S.-C. Wooh and Y. Shi, “Optimum beam steering of linear phased arrays," Wave Motion 29, 245-265 (1999).

[19] J. Aboujeib, A. Perennou, V. Quintard and J. L. Bihan, “Planar phased-array transducers associated with specific electronic command for acoustooptic deflectors,” J. Opt. A: Pure Appl. Opt. 9, 463-469 (2007).

[20] S. N. Antonov, A. V. Vainer, V. V. Proklov and Y. G. Rezvov, “Extension of the angular scanning range of the acousto-optic deflector with a two-element phased-array piezoelectric transducer,” Tech. Phys. 58, 1346-1351 (2013).

[21] E.J. Galvez, Gaussian Beams (Colgate University, 2009).

[22] T. Wang, C. Zhang, A. Aleksov, I.A. Salama and A. Kar, “Dynamic two-dimensional refractive index modulation for high performance acousto-optic deflector,” Optics Express 23, 33667-33680 (2015).

[23] M. Abramowitz and I. A. Stegun, Handbook of mathematical functions: with formulas, graphs, and mathematical tables (Courier Corporation, 1964), pp. 885-886.

[24] T. D. K. Ngoc and W. G. Mayer, “Numerical integration method for reflected beam profiles near Rayleigh angle,” J. Acoust. Soc. Am. 67, 1149-1152 (1980).

[25] Kazuyuki Nakahata and Naoyuki Kono, “3-D Modelings of an ultrasonic phased array transducer and its radiation properties in solid, ultrasonic waves,” Dr. Santos (Ed.), ISBN: 978-953-51-0201-4, InTech, (2012) 60-80.

[26] W. R. Klein and B. D. Cook, "Unified Approach to Ultrasonic Light Diffraction," IEEE Transactions on sonics and ultrasonics 14, 123-134 (1967).

CHAPTER 7: SUMMARY

As concept verification and demonstraiton of the dynamic grating implemented by the "acoustic beam steering" based on multiple linear phased-array transducer, the deailed design parameters, such as the pitch between neighboring elements (S), the time delay ($\Delta\tau$) for phase shift and the specific demensions for single element (element width W and element height H), have been listed in Tables 3 and 4 (for TeO_2-AOD) and 5 and 6 (for the Ge-AOD).

Given the AO material of TeO_2, the RF frequencies of 60MHz, 75MHz, 95MHz and 200MHz were chosed to charactierize the AO performances of TeO_2-AOD, such as the diffraction efficiency and the deflection angle. The deflection angle θ_D equals the effective input angle θ_{in} = $\theta_0 + \tilde{\theta}$, determined by Bragg condition and realized by acoustic beam steering technique. L is the thickness of AO material, characterized by Klein-Cook parameter to make sure Bragg diffraction operation. The index modulation Δn should be optimized for predefined F and L for maximum diffraction efficiency operation. Unfortunately, such optimum parameters combination of F, L and Δn are strongly interacted with each other. In the real situation, the pitch of S must make sure the generation of the acoustic beam steering, so that is why only the S_{min}=10.5μm was selected conrresponding to the F_{max}=200 MHz at the price of the degradation of the diffraction efficiency.

Similarly, the RF frequencies of 65MHz, 70MHz, 85MHz and 200MHz were simulated for Ge-AOD. In the real situation, the pitch of S must make sure the generation of the acoustic beam steering, so that is why only the S_{min}=13.75μm was selected conrresponding to the F_{max}=200 MHz at the price of the degradation of the diffraction efficiency.

APPENDIX A: DETAILED DERIVATION OF EQUATION (4) AND (5) IN CHAPTER 6

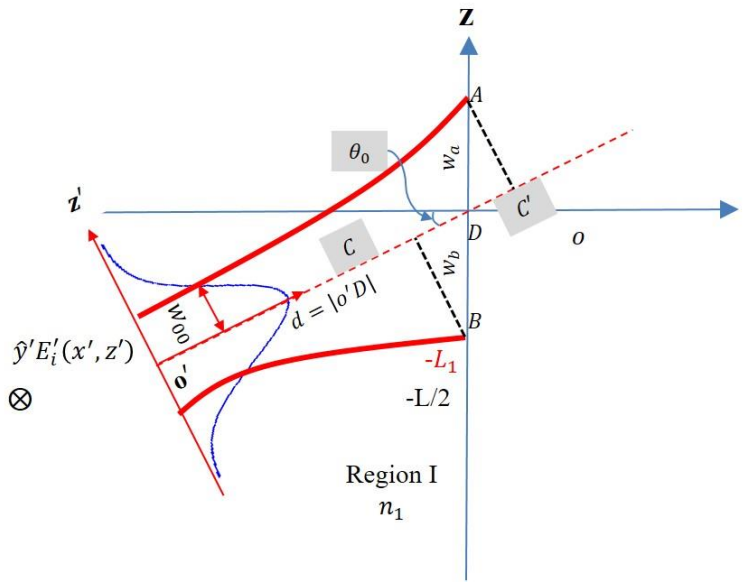

Figure 0-1 Schematic of Gaussian beam interception widths on input surface of AO medium.

when Gaussian beam comes at the input surface of AO medium, there are two interception points of A and B, the corresponding the interception widths are usually different, $|AD| \neq |BD|$, which are necessary for the next calculation of Gaussia beam propagation and diffraction inside AO medium. Corsely, we label $|AD|$ and $|BD|$ as w as follows.

$$AC = w_{00}\sqrt{1 + \left(\frac{d + wsin\theta_0}{\pi {w_{00}}^2/\lambda_0}\right)^2} = w_a cos\theta_0$$

$$1 + \left(\frac{d + wsin\theta_0}{\pi {w_{00}}^2/\lambda_0}\right)^2 = \left(\frac{w}{w_{00}} cos\theta_0\right)^2$$

let $\chi_R = \pi {w_{00}}^2/\lambda_0$

$$1 + \left(\frac{d + w_a sin\theta_0}{\chi_R}\right)^2 = \left(\frac{w_a}{w_{00}} cos\theta_0\right)^2$$

$$w^2\left[sin\theta_0{}^2-\left(\frac{\chi_R cos\theta_0}{w_{00}}\right)^2\right]+w(2dsin\theta_0)+(d^2+\chi_R{}^2)=0$$

Assume $A=\left[sin\theta_0{}^2-\left(\frac{\chi_R cos\theta_0}{w_{00}}\right)^2\right]$, $B=(2dsin\theta_0)$ and $C=(d^2+\chi_R{}^2)$, accordint to the quadratic formula for the roots of the general quadratic equation:

$$w=\frac{-B\pm\sqrt{B^2-4AC}}{2A}$$

Given $A>0$, and the interception widths of the input Gaussian beam $|AD|=w_a>|BD|=w_b$,

$$w_a=|AD|=\frac{-B-\sqrt{B^2-4AC}}{2A}$$

$$w_b=|BD|=\frac{-B+\sqrt{B^2-4AC}}{2A}$$

Now $B^2-4AC=(2d_1sin\theta_0)^2-4\left(sin\theta_0{}^2-\frac{cos\theta_0{}^2}{w_{00}{}^2}x_R{}^2\right)\left(x_R{}^2-d_1{}^2\right)$, subsition back to give

$$w_a=\frac{-2d_1sin\theta_0-\sqrt{(2d_1sin\theta_0)^2-4\left(sin\theta_0{}^2-\frac{cos\theta_0{}^2}{w_{00}{}^2}x_R{}^2\right)\left(x_R{}^2-d_1{}^2\right)}}{2\left(sin\theta_0{}^2-\frac{cos\theta_0{}^2}{w_{00}{}^2}x_R{}^2\right)}$$

$$w_b=\frac{2d_1sin\theta_0-\sqrt{(2d_1sin\theta_0)^2-4\left(sin\theta_0{}^2-\frac{cos\theta_0{}^2}{w_{00}{}^2}x_R{}^2\right)\left(x_R{}^2-d_1{}^2\right)}}{2\left(sin\theta_0{}^2-\frac{cos\theta_0{}^2}{w_{00}{}^2}x_R{}^2\right)}$$

APPENDIX B: LIST OF PUBLICATIONS

Journal Papers (published or submitted)

1. T-S. Wang, et al., “Effect of large deflection angle on the laser intensity profile produced by acousto-optic deflector scanners in high precision manufacturing,” The Journal of Laser Applications (2016)

2. T-S. Wang, et al., “Dynamic two-dimensional refractive index modulation for high performance acousto-optic deflector,” Optics Express (2015)

3. T-S. Wang, et al., (2017). "Two-dimensional analytic modeling of acoustic diffraction for ultrasonic beam steering by phased array transducers," Ultrasonics (2017).

4. T-S. Wang, et al., "Two-dimensional refractive index modulation by phased array transducers in acousto-optic deflectors," Applied Optics (2017).

5. T-S. Wang, et al., “Gaussian beam diffraction by two-dimensional refractive index modulation for high diffraction efficiency and large deflective angle,” Optics Express (submitted 2017).

Conference Proceedings

1. T.S. Wang, C. Zhang, A. Aleksov, I.A. Salama, A. Kar, “Effect of large deflection angle on the laser intensity profile produced by AOD scanners in high precision manufacturing,” ICALEO Conference Proceedings (2015).

2. T.S. Wang, C. Zhang, A. Aleksov, I.A. Salama, A. Kar, “Large angle of Bragg diffraction using interference of acoustic wave inside acousto-optic deflector,” ICALEO Conference Proceedings (2013). xx

Patents

1. T.S. Wang, et al., “ACOUSTO-OPTIC DEFLECTOR WITH MULTIPLE TRANSDUCERS FOR OPTICAL BEAM STEERING,” United States Patent Application 20150338718 Kind Code:A1